Copyright Warning & Restrictions

The copyright law of the United States (Title 17, United States Code) governs the making of photocopies or other reproductions of copyrighted material.

Under certain conditions specified in the law, libraries and archives are authorized to furnish a photocopy or other reproduction. One of these specified conditions is that the photocopy or reproduction is not to be "used for any purpose other than private study, scholarship, or research." If a, user makes a request for, or later uses, a photocopy or reproduction for purposes in excess of "fair use" that user may be liable for copyright infringement,

This institution reserves the right to refuse to accept a copying order if, in its judgment, fulfillment of the order would involve violation of copyright law.

Please Note: The author retains the copyright while the New Jersey Institute of Technology reserves the right to distribute this thesis or dissertation

Printing note: If you do not wish to print this page, then select "Pages from: first page # to: last page #" on the print dialog screen

NJIT New Jersey's Science & Technology University

The Van Houten library has removed some of the personal information and all signatures from the approval page and biographical sketches of theses and dissertations in order to protect the identity of NJIT graduates and faculty.

ABSTRACT

A NUMERICAL STUDY ON THE PROPAGATION AND INTERACTION OF STRONGLY NONLINEAR SOLITARY WAVES

by
Qiyi Zhou

We study numerically a strongly nonlinear long wave model for surface gravity waves propagating in both one and two horizontal dimensions. This model often referred to as the Su-Gardner or Green-Naghdi equations can be derived from the Euler equations under the assumption that the ratio between the characteristic wavelength and water depth is small, but no assumption on the wave amplitude is required. We first generalize the model to describe large amplitude one-dimensional solitary waves in the presence of background shear of constant vorticity. After computing the solitary wave solution of the strongly nonlinear model, the interaction between two solitary waves propagating in the same and opposite directions is investigated numerically and the numerical solutions are compared with weakly nonlinear asymptotic solutions. In particular, the effects of strong nonlinearity as well as background shear are examined. We also derive a model for strongly nonlinear long waves in uniform shear flow interacting with non-uniform bottom topography, and the generation of upstream-propagating solitary waves is investigated numerically. We then examine the stability characteristics of large amplitude solitary waves subject to transverse perturbations with assuming that the characteristic wavelength in the transverse direction is much greater than that in the wave propagation direction. Using an asymptotic approach, a sufficient condition for instability is obtained. To test this result, we solve numerically the strongly nonlinear, weakly two-dimensional model using a finite difference method. This numerical model is also used to study the interaction between two solitary waves propagating obliquely with a small angle. In particular, the Mach reflection due to the strong oblique interaction is investigated

numerically in detail and our numerical solution is compared with the analytical solution of the weakly nonlinear KP equation as well as available experimental data.

A NUMERICAL STUDY ON THE PROPAGATION AND INTERACTION OF STRONGLY NONLINEAR SOLITARY WAVES

by
Qiyi Zhou

A Dissertation
Submitted to the Faculty of
New Jersey Institute of Technology and
Rutgers, The State University of New Jersey – Newark
in Partial Fulfillment of the Requirements for the Degree of
Doctor of Philosophy in Mathematical Sciences

Department of Mathematical Sciences, NJIT
Department of Mathematics and Computer Science, Rutgers-Newark

August 2010

Copyright © 2010 by Qiyi Zhou
ALL RIGHTS RESERVED

APPROVAL PAGE

A NUMERICAL STUDY ON THE PROPAGATION AND INTERACTION OF STRONGLY NONLINEAR SOLITARY WAVES

Qiyi Zhou

Wooyoung Choi, Dissertation Advisor — Date
Professor of Mathematical Sciences, NJIT

Michael Booty, Committee Member — Date
Professor of Mathematical Sciences, NJIT

Lou Kondic, Committee Member — Date
Professor of Mathematical Sciences, NJIT

Yuan-nan Young, Committee Member — Date
Associate Professor of Mathematical Sciences, NJIT

Yi Li, Committee Member — Date
Associate Professor of Mathematical Sciences, Stevens Institute of Technology

BIOGRAPHICAL SKETCH

Author: Qiyi Zhou

Degree: Doctor of Philosophy

Date: August 2010

Undergraduate and Graduate Education:

- Doctor of Philosophy in Mathematical Sciences,
  New Jersey Institute of Technology, Newark, NJ, 2010
- Bachelor of Science in Information and Computational Sciences,
  Zhejiang University, Hangzhou, P. R. China, 2006

Major: Applied Math

This thesis is dedicated to my parents and my sisters who have supported me all the way since the beginning of my studies.

ACKNOWLEDGMENT

I would like to express my deepest and sincerest gratitude to my Ph.D. supervisor, Professor Wooyoung Choi. He has given me a lot of help during my academic career at NJIT. His wide knowledge and logical way of thinking have been of great value for me. His understanding, patience, encouraging, and personal guidance have provided a good basis for the present thesis.

There is no enough words to express my appreciation to Dr. Booty, Dr. Kondic, Dr. Moore, Dr. Young, and Dr. Li for serving as members of my dissertation committee. Their precious advices and suggestions make this work complete. Especially I gratefully acknowledge Dr. Li's help on numerical methods.

Finally I would like to thank the Department of Ocean Systems Engineering in the Korea Advanced Institute of Science and Technology, who provides me an excellent environment to carry out my research with my advisor for a half year during my Ph.D. study.

TABLE OF CONTENTS

Chapter **Page**

1 INTRODUCTION 1

2 STRONGLY NONLINEAR LONG WAVE MODELS 3

2.1 Strongly Nonlinear Fully 2D Long Wave Model 3

2.2 Strongly Nonlinear Weakly 2D Long Wave Model 4

2.3 One-dimensional Strongly Nonlinear Long Wave Model 5

3 STRONGLY NONLINEAR LONG GRAVITY WAVES IN UNIFORM SHEAR FLOWS 6

3.1 One-dimensional Model 6

3.2 Solitary Wave Solutions 7

3.3 A Numerical Method to Solve the One-dimensional Equations 10

3.4 Weakly Nonlinear Analysis for Wave Interactions in Uniform Shear Flows 25

3.5 Numerical Simulation of Solitary Wave Interaction 35

3.5.1 Head-on Collision of Two Solitary Waves 35

3.5.2 Overtaking Collision of Two Solitary Waves 38

3.5.3 Disintegration of an Initial Elevation into Solitary Waves . . . 44

3.6 Uniform Shear Flow Interacting with Bottom Topography 47

3.6.1 Derivation of the Governing Equations 48

3.6.2 Numerical Simulations 52

4 TRANSVERSE INSTABILITY OF SOLITARY WAVES 56

5 NUMERICAL STUDY OF THE STRONGLY NONLINEAR WEAKLY 2D LONG WAVE MODEL 69

5.1 Linear Dispersion Relationship 69

5.2 Numerical Method to Solve the Weakly 2D Long Wave Model 73

5.3 Numerical Simulations of Transverse Instability of Solitary Waves . . 81

5.4 Mach Reflection 85

TABLE OF CONTENTS
(Continued)

Chapter **Page**

5.4.1 Background 85

5.4.2 Oblique Interaction of Two Solitary Waves 87

5.4.3 Comparison with Tanaka's Numerical Solutions 91

5.4.4 Comparison with Experiment Data and the KP Solution 93

6 CONCLUSION 96

APPENDIX A TRANSVERSE INSTABILITY BY WEAKLY 2D MODEL . 98

APPENDIX B RESCALING $F = 1$ FOR ONE-DIMENSIONAL STRONGLY NONLINEAR LONG WAVE MODEL 110

REFERENCES 111

LIST OF TABLES

Table **Page**

5.1 Convergence in the x-direction with fixed $\triangle y = \frac{\pi}{3}$ and $\triangle x = 0.2,\ 0.1,$ and 0.05, respectively 79

5.2 Convergence in the y-direction with fixed $\triangle x = 0.01$ and $\triangle y = \frac{20\pi}{3},\ \frac{10\pi}{3},$ and $\frac{5\pi}{3}$, respectively 79

5.3 Amplification factor α of the stem waves for different wave amplitude A_0 $\left(k = \frac{\tan\psi_0}{\sqrt{2A_0}}\right)$ with $\psi_0 = 30^0$: $\alpha_{X=71.1}$(Exp) are the laboratory data at location $X = 71.1$ and $\alpha_{X=71.1}$(KP) are calculated from the corresponding KP exact solutions at the given location. $\alpha_{T=300}$(Num) are numerical results obtained by using strongly nonlinear weakly 2D long wave model at $T = 300$. When $A_0 = 0.086$ and $A_0 = 0.108$, the amplification factor α is calculated at $T = 400$. $\alpha_{T=\infty}$(Exp) are estimated from the exponential curve fitting to the laboratory data, and $\alpha_{T=\infty}$(KP) are values predicted by the solution of the KP equation as $T \to \infty$. In the last row of $A_0 = 0.413$, the values of α in the brackets are obtained at $X = 50.8$, because of the wave breaking immediately after this point; hence, the greater amplification cannot be realized in experiment. The large deviations in the estimation $\alpha_{T=\infty}$(Exp) in the boxes from the theoretical predictions for the cases near $k = 1$ 94

LIST OF FIGURES

Figure **Page**

2.1 A schematic of the problem. Here h is the water depth and ζ is the surface elevation. 4

3.1 Uniform shear flow with constant negative vorticity $\omega = -\Omega$. 7

3.2 In the left panel, the analytical solution of (3.11) (solid line) is compared with the numerical solution (+) using a Lobatto IIIA method. The right panel shows the relative error between the analytical solution and the numerical solution. 9

3.3 Solitary wave solutions for the presence of shear (F=0.5). Left panel: the upstream-propagating solitary wave ($c < 0$); Right panel: the downstream-propagating solitary wave ($c > 0$). The wave amplitude $a = 0.5$; the Froude number F=0.5; the number of grids N=8000, and the length of the computational domain L=80. 10

3.4 Comparison of dispersion relationships: ω_1: solid line; ω_2: dotted line; ω_3: dashed line. 12

3.5 In the left panel, the numerical solution (+) is compared with the analytical solution (solid line). In the right panel, the absolute error between the numerical solution and the analytical solution at time $T = 20$ is shown. In this computation, $\triangle t = 0.001$ and the computational domain is 10π. 13

3.6 Convergence in space with reducing $\triangle x$ for a fixed time step $\triangle t = 0.001$. 14

3.7 The periodic solutions of the equation (3.19) at time $T = 5$ (+), $T = 20$ ($\cdot$), and $T = 100$ ($*$) are compared with the numerical solutions at time $T = 5$ (solid line), $T = 20$ (dash line), and $T = 100$ (dot dash line), respectively. 16

3.8 From left to right, two panels represent the relative error between the numerical solutions and the periodic solutions with $F = 0$ at $T = 20$ and $T = 100$, respectively. 16

3.9 Convergence in space of the periodic solutions with reducing $\triangle x$ for fixing time step of $\triangle t = 0.001$, where $F = 0$, $T = 5$, $\triangle x = 0.2,\ 0.1,\ 0.05$, respectively. 17

3.10 The analytical solutions of the upstream-propagating solitary waves at time $T = 5$ (+), $T = 20$ ($\cdot$), and $T = 100$ ($*$) are compared with the numerical solutions at time $T = 5$ (solid line), $T = 20$ (dash line), and $T = 100$ (dot dash line), respectively. 18

LIST OF FIGURES
(Continued)

Figure **Page**

3.11 From left to right, these figures represent the relative error between the numerical solutions and the analytical solutions of upstream-propagating solitary waves with $F = 0.5$ at $T = 20$ and $T = 100$, respectively. . . . 19

3.12 Convergence in space of the upstream-propagating solitary waves with reducing $\triangle x$ for fixing time step of $\triangle t = 0.001$, where $F = 0.5$, $T = 5$, $\triangle x = 0.2,\ 0.1,\ 0.05$, respectively. 19

3.13 The analytical solutions of the downstream-propagating solitary waves at time $T = 5$ $(+)$, $T = 20$ $(\cdot)$, and $T = 100$ $(*)$ are compared with the numerical solutions at time $T = 5$ (solid line), $T = 20$ (dash line), and $T = 100$ (dot dash line), respectively. 20

3.14 From left to right, these figures represent the relative error between the numerical solutions and the analytical solutions of the downstream-propagating solitary waves with $F = 0.5$ at $T = 20$ and $T = 100$, respectively. 21

3.15 Convergence in space of the downstream-propagating solitary waves with reducing $\triangle x$ for fixing time step of $\triangle t = 0.001$, where $F = 0.5$, $T = 5$, $\triangle x = 0.2,\ 0.1,\ 0.05$, respectively. 21

3.16 Mass conserved quantity and momentum conserved quantity of the upstream propagating solitary waves are shown in the left panel and right panel at time $T = 20$ with relative error about 10^{-14} and 10^{-12}, respectively. Where $F = 0.5$, $a = 0.5$, $\triangle t = 0.001$, and $\triangle x = 0.01$. . . 23

3.17 Mass conserved quantity and momentum conserved quantity of the downstream propagating solitary waves are shown in the left panel and right panel at time $T = 20$ with relative error about 10^{-14} and 10^{-11}, respectively. Where $F = 0.5$, $a = 0.5$, $\triangle t = 0.001$, and $\triangle x = 0.01$. . . 24

3.18 Vorticity conserved quantity of the upstream-propagating and downstream propagating solitary waves at time $T = 20$ are shown in the left panel and right panel with relative error about 10^{-11} and 10^{-10}, respectively. Where $F = 0.5$, $a = 0.5$, $\triangle t = 0.001$, and $\triangle x = 0.01$. 24

3.19 Head-on collision of two solitary waves with $a_1 = a_2 = 0.5$ for $F = 0.5$. . 35

3.20 The surface wave profile during the head-on collision with $a_1 = a_2 = 0.5$ for $F = 0$ and $F = 0.5$ are shown in the left and right panels, respectively, and the maximum wave amplitude are measured at $T = 21$ and $T = 20.3$ numerically as well. The flat solid lines are the predicted maximum values from the weakly nonlinear analysis. 36

LIST OF FIGURES
(Continued)

Figure **Page**

3.21 Symmetric phase shift for the right-going and left-going waves for $F = 0$, $a_1 = 0.5$ and $a_2 = 0.5$. Where the solid line is the numerical result after head-on collision and the dash dot line is the solitary wave solution without head-on collision at time $T = 60$. 37

3.22 Asymmetric phase shift for the right-going and left-going waves for $F = 0.5$, $a_1 = 0.5$ and $a_2 = 0.5$. Where the solid line is the numerical result after head-on collision and the dash dot line is the solitary wave solution without head-on collision at time $T = 60$. 38

3.23 Overtaking collision of two solitary waves between $T_1 = 300$ and $T_2 = 600$ with $F = 0.5,\ a_1 = 0.4,$ and $a_2 = 0.2$. 39

3.24 Overtaking collision of two solitary waves between $T_1 = 150$ and $T_2 = 450$ with $F = 0.5,\ a_1 = 0.4,$ and $a_2 = 0.08$. 40

3.25 Two solitary waves merge into a single wave with flat peak during the overtaking collision at time $T = 369.5$. Where $F = 0$, $a_1 = 0.4$, and $a_2 = 0.1176$ with fixed ratio $\frac{a_1}{a_2} = 3.4$. 41

3.26 Two solitary waves remain separated during the overtaking collision, for $F = 0$, $a_1 = 0.8$, and $a_2 = 0.2353$ with fixed ratio $\frac{a_1}{a_2} = 3.4$. 41

3.27 Two upstream-propagating solitary waves merge into a single wave with flat peak during the overtaking collision at time $T = 349$. Where $F = 0.5$, $a_1 = 0.4$, and $a_2 = 0.125$ with fixed ratio $\frac{a_1}{a_2} = 3.2$. 42

3.28 Two upstream-propagating solitary waves remain separated during the overtaking collision. Where $F = 0.5$, $a_1 = 0.4$, and $a_2 = 0.125$ with fixed ratio $\frac{a_1}{a_2} = 3.2$. 42

3.29 Two downstream-propagating solitary waves merge into a single wave with flat peak during the overtaking collision at time $T = 347.3$. Where $F = 0.5$, $a_1 = 0.4$, and $a_2 = 0.1127$ with fixed ratio $\frac{a_1}{a_2} = 3.55$. 43

3.30 Disintegration of a upstream-propagating single elevation of amplitude $a = 0.5$ in the shear flow with $F = 0.5$ at $t = 10$ and $t = 40$. We use the relation between η and u for traveling solitary waves at $t = 0$. . . 44

3.31 Disintegration of a downstream-propagating single elevation of amplitude $a = 0.5$ in the shear flow with $F = 0.5$ at $t = 10$ and $t = 40$. We use the relation between η and u for traveling solitary waves at $t = 0$. . . 45

3.32 Disintegration of a single elevation of amplitude $a = 0.5$ in the shear flow with $F = 0.5$ at $t = 10$ and $t = 40$. At $t = 0$, we set $u = 0$. 46

LIST OF FIGURES
(Continued)

Figure **Page**

3.33 A schematic of uniform flow past topography. 47

3.34 A schematic of uniform shear flow past topography. 48

3.35 Uniform shear flow interacts with non-uniform convex topography between $T = 0$ and $T = 200$. Where $f_m = 0.2,\ w = 2.0,\ u(x,0) = 1.0$, and $F = 0.5$. 52

3.36 Uniform flow interacts with non-uniform convex topography between $T = 0$ and $T = 200$. Where $f_m = 0.2,\ w = 2.0,\ u(x,0) = 1.0$, and $F = 0$. . 53

3.37 Uniform shear flow interacts with non-uniform concave topography between $T = 0$ and $T = 350$. Where $f_m = -0.2,\ w = 2.0,\ u(x,0) = 1.0$, and $F = 0.5$. 54

3.38 Uniform flow interacts with non-uniform concave topography between $T = 0$ and $T = 350$. Where $f_m = -0.2,\ w = 2.0,\ u(x,0) = 1.0$, and $F = 0$. 54

5.1 First arrangement of the grid points. 70

5.2 Second arrangement of the grid points. 71

5.3 Third arrangement of the grid points. 71

5.4 Comparison of dispersion relationships: solid line, dash dot line, $\diamond$ line and dash line represents ω, ω_1, ω_2, and ω_3, respectively. In the left panel, $k_1 = 1$ is fixed, and $\triangle x = \triangle y = 0.1$. In the right panel, $k_2 = 1$ is fixed, and $\triangle x = \triangle y = 0.1$. 72

5.5 Numerical solution for a solitary wave propagating in the x-direction at $T = 100$. 76

5.6 Numerical solution compared with the solitary wave solution of the SG equation. The solid line is the solitary wave solution and the '+' line is the numerical solution at $T = 20$. The dashed dot line is the solitary wave solution and * is the numerical solution at $T = 100$. 76

5.7 The relative error between the numerical solution and solitary wave solution of the SG equation at $T = 100$ for varying x with $y = 0$. 76

5.8 Mass and horizontal momentum conserved with relative error less than 10^{-12} and close to 10^{-12} at time $T = 20$ are shown in the left and right panels, respectively. 77

5.9 Convergence of the numerical method in space with $\triangle t = 0.005$, time $T = 20$ and $\triangle x = 0.2,\ 0.1,\ 0.05$, respectively. 78

Figure **Page**

5.10 Mass η and horizontal momentum ηu conserved with relative error less than 10^{-11} at time $T = 20$ are shown in the left and right panels, respectively. 80

5.11 Horizontal momentum ηv is conserved with relative error less than 10^{-14} at time $T = 20$. 80

5.12 The solid line is the solitary wave solution and the '*' line is the numerical solution in the x-direction without transverse perturbation in the y-direction at time $T = 100$ with $y = 0$ and wave amplitude $a = 3.5$. . . 81

5.13 Numerical solution of the solitary wave in 3D form and the relative error between solitary wave solution and numerical solution are shown in the right and left panels, respectively. Where $a = 3.5,\ T = 100,\ \triangle t = 0.005,\ \triangle x = 0.05$, and $\triangle y = 6$. 82

5.14 Numerical solutions of solitary wave with small transverse perturbation in the y-direction at time $T = 0$ and $T = 52$ are shown in the left and right panels, respectively. Where $a = 3.5,\ \epsilon = 0.01,\ \gamma = 0.1,\ \triangle t = 0.005,\ \triangle x = 0.05$, and $\triangle y = \frac{\pi}{3}$. 83

5.15 The cross section of numerical solutions of solitary wave with $y = 0$ in the x-direction at time $T = 50$ and $T = 52$ are shown in the left and right panels, respectively. Where $a = 3.5,\ \epsilon = 0.01,\ \gamma = 0.1,\ \triangle t = 0.005,\ \triangle x = 0.05$, and $\triangle y = \frac{\pi}{3}$. 83

5.16 Numerical solutions of solitary wave with small transverse perturbation in the y-direction at time $T = 0$ and $T = 204$ are shown in the left and right panels, respectively. Where $a = 2,\ \epsilon = 0.01,\ \gamma = 0.1,\ \triangle t = 0.005,\ \triangle x = 0.05$, and $\triangle y = \frac{\pi}{3}$. 84

5.17 Numerical solution of the solitary wave in 3D form and the relative error between solitary wave solution and numerical solution are shown in the left and right panels, respectively. Where $a = 2,\ T = 400,\ \triangle t = 0.005,\ \triangle x = 0.05$, and $\triangle y = 6$. 84

5.18 Mach reflection pattern, showing the incident wave (– – –), reflected wave (– - –), and the stem wave (- -). The entire pattern is expanding uniformly from the leading edge O, such that the apex P is moving with speed V_*. 85

5.19 The Mach reflection. The left panel illustrates a semi-infinite line-soliton propagating parallel to the wall. The right panel is an equivalent system with two line-solitons propagating to the right when we ignore the viscous effect on the wall. 86

LIST OF FIGURES
(Continued)

Figure **Page**

5.20 Two solitary waves propagate in x'- and x''-directions, respectively. . . . 88

5.21 From left to right, these panels correspond to the numerical solutions at $T = 0$ and $T = 300$. 89

5.22 From left to right, these panels correspond to the contour plots of the solutions at $T = 0,\ 150,$ and 250. 89

5.23 From left to right, these panels correspond to the numerical solutions at $T = 0$ and $T = 300$. 90

5.24 From left to right, these panels correspond to the contour plots of the solutions at $T = 0,\ 200,$ and 270. 90

5.25 The evolution of amplification factor α as a function of time T with incident wave amplitude $a = 0.1$ and incident angle $\psi_0 = 23^o$. The solid line is the numerical result. The dash line is the predicted value given by Miles' model and the dash dot line is the value predicted by the KP equation. 92

5.26 The evolution of amplification factor α as a function of time T with incident wave amplitude $a = 0.3$ and incident angle $\psi_0 = 40^o$. The solid line is the numerical result. The dash line is the predicted value given by Miles' model and the dash dot line is the value predicted by the KP equation. 93

CHAPTER 1

INTRODUCTION

It has been of great interest for many years to model and understand the motion of nonlinear water waves due to a broad range of applications in ocean and coastal engineering and physical oceanography as well as theoretical curiosity of their complex dynamics. Under the assumption that the flow is incompressible and inviscid, the Euler equations are the governing equations for the fully nonlinear water waves problem, but they are too nonlinear to solve analytically. Although a great deal of effort has been made, solving the Euler equations with the free surface numerically is also a nontrivial task and is computationally expensive. Therefore, the description of nonlinear water waves often rely on reduced models.

Under various assumptions, a number of approximate models have been derived and are commonly used to gain physical insight into the dynamics of nonlinear waves. Particularly, in shallow water, the small amplitude and long wavelength assumptions have been adopted to obtain the well-known weakly nonlinear long wave models, such as the Korteweg-de Vries (KdV) equation [20] and the Boussinesq equations [3]. Despite the fact that the weakly nonlinear approximation to the Euler equations is often relevant for real applications, these weakly nonlinear models are still of limited success to describe the dynamics of large amplitude waves. To overcome this shortcoming, under the sole assumption that the wavelength is much greater than the local water depth, a strongly nonlinear long wave model was derived by Su and Gardner [28] without imposing any assumption on the wave amplitude. For one-dimensional waves, it has been shown [8] that the model of Su and Gardner approximates the Euler equations much better than the classical weakly nonlinear models, especially, in the strongly nonlinear regime. Here, motivated by this success,

this thesis is made (1) to generalize the strongly nonlinear model of Su and Gardner [28] to investigate the propagation and interaction of one-dimensional solitary waves in the presence of background shear, possibly, interacting with non-uniform bottom topography; (2) to examine instability of large amplitude solitary waves subject to long wave transverse perturbations; (3) to derive a weakly two-dimensional model to study the strong interaction between two solitary waves propagating obliquely with a small angle.

This thesis is organized as follows. In §2, we first introduce the strongly nonlinear long wave model of Su and Gardner [28] in two horizontal dimensions (also known as the Green-Naghdi equations) and, then, show the derivation of a weakly two-dimensional strongly nonlinear model with assuming that the characteristic wave length in the y-direction is much greater than the wavelength in the x-direction. In §3, we solve numerically the one-dimensional model of Su and Gardner generalized to include the effect of background shear using a 4th-order Adams-Bashforth method and validate our numerical method with the solitary wave solutions of the model. Using this numerical model, we study the interaction of large amplitude solitary waves in the presence of background shear and compare our numerical solutions with the weakly nonlinear analysis based on the weakly nonlinear bi-directional model proposed by Wu [37]. We also derive the strongly nonlinear long wave model with non-uniform topography, and study the interaction of the uniform shear flow with topography numerically. In §4, we study transverse instability of a single solitary wave using a asymptotic expansion technique and obtain a sufficient condition for instability. In §5, after introducing a numerical method to solve the weakly 2D long wave model, we examine the transverse instability numerically. Finally, we investigate numerically the Mach reflection due to the oblique interaction between two solitary waves and compare our numerical solutions with experimental data.

CHAPTER 2

STRONGLY NONLINEAR LONG WAVE MODELS

2.1 Strongly Nonlinear Fully 2D Long Wave Model

For an inviscid, irrotational, and incompressible fluid, the strongly nonlinear long wave models were derived by Su & Gardner [28] for one-dimensional (1D) waves and by Green & Naghdi [15] for two-dimensional (2D) waves from the Euler equations under the assumption that the ratio between wavelength (L) and fluid depth (h) is small. There is no limitation on the wave amplitude and, therefore, it might be able to describe higher-order nonlinear phenomena better than the well-known weakly nonlinear long wave models, such as the KdV equation [20] for 1D waves and the KP equation [19] for weakly 2D waves.

The strongly nonlinear fully 2D model is given [15], in vector form, by

$$\frac{\partial \eta}{\partial t} + \boldsymbol{\nabla} \boldsymbol{\cdot} (\eta \boldsymbol{u}) = 0 \ , \tag{2.1}$$

$$\frac{\partial \boldsymbol{u}}{\partial t} + \boldsymbol{u} \boldsymbol{\cdot} \boldsymbol{\nabla} \boldsymbol{u} + g \boldsymbol{\nabla} \zeta = \frac{1}{\eta} \boldsymbol{\nabla} \left(\frac{1}{3} \eta^3 G \right) \ , \tag{2.2}$$

where $\zeta(x, y, t)$ is the surface elevation; g is the gravity acceleration; h is the depth of the fluid; $\boldsymbol{u}(x, y, t) = (u, v)$ is the depth-averaged horizontal velocity vector; u is the depth-averaged horizontal velocity in the x-direction; v is the depth-averaged horizontal velocity in the y-direction; and

$$\eta = h + \zeta, \qquad \boldsymbol{\nabla} = \left(\frac{\partial}{\partial x}, \frac{\partial}{\partial y} \right),$$
$$G(x, y, t) = \boldsymbol{\nabla} \boldsymbol{\cdot} \boldsymbol{u_t} + \boldsymbol{u} \boldsymbol{\cdot} \boldsymbol{\nabla} (\boldsymbol{\nabla} \boldsymbol{\cdot} \boldsymbol{u}) - (\boldsymbol{\nabla} \boldsymbol{\cdot} \boldsymbol{u})^2 .$$

Since we assume no external pressure is applied to the free surface, no pressure term appears in equation (2.2). A schematic of the problem is shown in Figure 2.1.

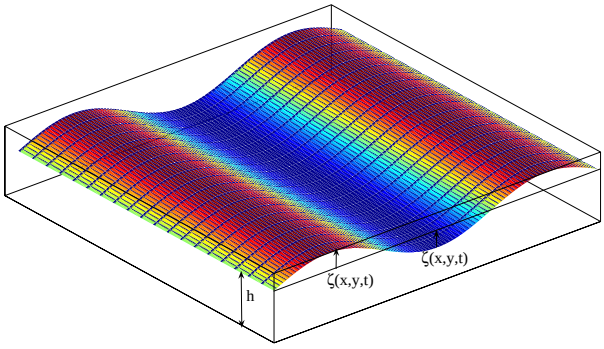

Figure 2.1 A schematic of the problem. Here h is the water depth and ζ is the surface elevation.

2.2 Strongly Nonlinear Weakly 2D Long Wave Model

When surface waves propagate in the ocean, they often travel in one direction (for example in the x-direction) and its dependence on the transverse direction (in the y-direction) is relatively weak. In other words, the wavelength in the y-direction is much greater than that in the x-direction. Under the assumption that the x-axis is aligned with the wave propagation direction, we can reduce the strongly nonlinear fully 2D long wave model given by equations (2.1)–(2.2) to the strongly nonlinear weakly 2D long wave model.

To derive the weakly 2D model, we first non-dimensionalize all physical variables in equations (2.1)–(2.2) as

$$x = lx^*,\ y = Ly^*,\ u = c_0u^*,\ v = \frac{l}{L}c_0v^*, \tag{2.3}$$

$$t = \frac{l}{c_0}t^*,\ \zeta = h\zeta^*,\ \eta = h\eta^*,\ c_0 = \sqrt{gh}, \tag{2.4}$$

where l is the wavelength in the x-direction and L is the wave length in the y-direction. For weakly 2D long waves, when we assume that

$$\epsilon = \frac{h}{l} << 1, \quad \beta = \frac{l}{L} << 1, \text{ and } \epsilon = \mathrm{O}\left(\beta\right), \tag{2.5}$$

we obtain the strongly nonlinear weakly 2D long wave model, after neglecting terms of $O(\epsilon^4)$ and $O(\epsilon^2\beta^2)$ and dropping the asterisks, as

$$\frac{\partial \eta}{\partial t} = -\left[\frac{\partial}{\partial x}(\eta u) + \frac{\partial}{\partial y}(\eta v)\right], \tag{2.6}$$

$$\frac{\partial}{\partial t}\left[\eta u - \frac{\partial}{\partial x}\left(\frac{\eta^3}{3}\frac{\partial u}{\partial x}\right)\right] = -\frac{\partial}{\partial x}\left(\eta u^2 + \frac{\eta^2}{2}\right) - \frac{\partial}{\partial y}(\eta u v) + \frac{\partial}{\partial x}\left[\frac{\partial}{\partial x}\left(\frac{\eta^3}{3}u\frac{\partial u}{\partial x}\right) + \frac{\eta^3}{3}\left(\frac{\partial u}{\partial x}\right)^2\right], \tag{2.7}$$

$$\frac{\partial}{\partial t}\left[\eta v - \frac{\partial}{\partial y}\left(\frac{\eta^3}{3}\frac{\partial u}{\partial x}\right)\right] = -\frac{\partial}{\partial x}(\eta u v) - \frac{\partial}{\partial y}\left(\eta v^2 + \frac{\eta^2}{2}\right) + \frac{\partial}{\partial y}\left[\frac{\partial}{\partial x}\left(\frac{\eta^3}{3}u\frac{\partial u}{\partial x}\right) + \frac{\eta^3}{3}\left(\frac{\partial u}{\partial x}\right)^2\right], \tag{2.8}$$

where $\eta = 1 + \zeta$ with ζ being the surface wave elevation. u and v are the depth-averaged horizontal velocities in the x- and y-directions, respectively. It should be pointed out that the weakly 2D model much more convenient to solve numerically when it is compared with the fully 2D model.

2.3 One-dimensional Strongly Nonlinear Long Wave Model

By setting $v = 0$, equations (2.1)–(2.2) can reduce to the one-dimensional model given by

$$\eta_t + (\eta u)_x = 0, \tag{2.9}$$

$$u_t + u u_x + g\zeta_x = \frac{1}{\eta}\left[\frac{\eta^3}{3}\left(u_{xt} + u u_{xx} - u_x^2\right)\right]_x, \tag{2.10}$$

where the subscripts x and t represent derivatives with respect to x and t. This is the system derived by Su and Gardner [28].

CHAPTER 3

STRONGLY NONLINEAR LONG GRAVITY WAVES IN UNIFORM SHEAR FLOWS

3.1 One-dimensional Model

In most studies on water waves, the assumption of irrotational flows has been adopted. In shear flows, it is no longer appropriate to assume that the fluid motion is irrotational, and the models shown in the previous chapter are no longer valid. Unfortunately, it is a non-trivial task to derive such a new model applicable to the wave motions in general shear flows and, therefore, we first consider a relative simple shear flow of uniform vorticity in this chapter.

Here, we study the strongly nonlinear long wave model generalized to a uniform shear flow by Choi [7]. Using an asymptotic method under the same assumption as before that the ratio between wavelength (L) and fluid depth (h) is small, the evolution equations can be obtained as

$$\eta_t + F\eta\eta_x + (\eta u)_x = 0, \tag{3.1}$$

$$u_t + uu_x + \zeta_x = \frac{1}{\eta}\left[\frac{\eta^3}{3}\left(u_{xt} + uu_{xx} - u_x^2 + F\eta u_{xx}\right)\right]_x, \tag{3.2}$$

where u is the depth-averaged horizontal velocity. ζ is the surface wave elevation. h is the depth of the fluid, and $\eta = h + \zeta(x,t)$. The Froude number F is defined as

$$F = \frac{\Omega h}{\sqrt{gh}}, \tag{3.3}$$

where Ω is a constant vorticity, as shown in Figure 3.1.

Notice that we can rescale the gravity acceleration $g = 1$ and the water depth $h = 1$.

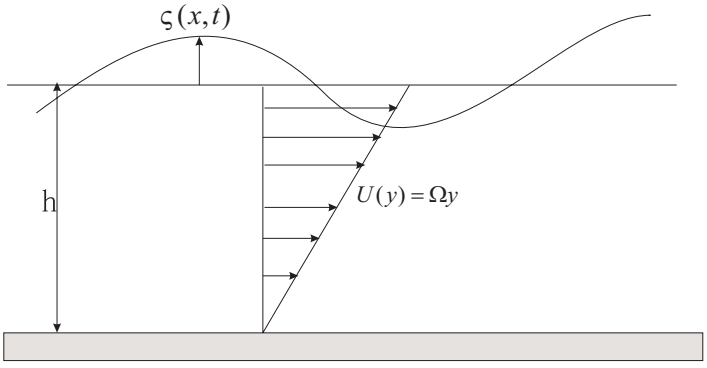

Figure 3.1 Uniform shear flow with constant negative vorticity $\omega = -\Omega$.

3.2 Solitary Wave Solutions

As shown in [7], solitary wave solutions of equations (3.1)–(3.2) can be found from the following equation

$$\left(\frac{d\zeta}{dx}\right)^2 = \frac{\zeta^2 N\left[\zeta\right]}{\left(D\left[\zeta\right]\right)^2}, \tag{3.4}$$

where N and D are given by

$$N\left[\zeta\right] = -\zeta^2 - \left(4 + \frac{12}{F^2}\right)\zeta + \frac{12}{F^2}\left(c^2 - Fc - 1\right), \tag{3.5}$$

$$D\left[\zeta\right] = \zeta^2 + 2\zeta + 2\left(1 - \frac{c}{F}\right). \tag{3.6}$$

Once ζ is computed, the horizontal velocity can be obtained as

$$u\left(x,t\right) = \frac{\zeta(x,t)\left\{c - \frac{F}{2}\left[2 + \zeta\left(x,t\right)\right]\right\}}{1 + \zeta\left(x,t\right)}. \tag{3.7}$$

By setting $\zeta_x = 0$ at the wave crest ($\zeta = a$), we can find the wave speed c, from $N[\zeta] = 0$, as

$$c_{\pm}(a) = \frac{F}{2} \pm \sqrt{1 + a + \frac{F^2}{12}\left(a^2 + 4a + 3\right)},$$

where a is the wave amplitude. Without losing generality, we assume that $F > 0$. Obviously, $0 < \zeta < a$ and $N\left[\zeta\right] > 0$ for all values of a and c. For upstream-propagating

solitary waves ($c = c_-$), it can be shown that the denominator $D[\zeta]$ never vanishes and solitary wave solutions exist for all wave amplitudes. On the other hand, for downstream-propagating solitary waves ($c = c_+$), if $F^2 < \frac{12}{3a^3+9a^2+8a}$, the denominator $D[\zeta] \neq 0$ for all values of ζ $(0 < \zeta < a)$; otherwise $D[\zeta] = 0$ for some value of ζ, for which a singularity appears at a point where the wave slope becomes infinite.

As a special case, when $F = 0$ (in the absence of background shear), the solitary wave solution can be found explicitly as

$$\zeta(x,t) = a\ \mathrm{sech}^2[k(x-ct)], \tag{3.8}$$

$$u(x,t) = \frac{c\zeta(x,t)}{1+\zeta(x,t)}, \tag{3.9}$$

where k and c can be expressed in terms of the wave amplitude a as

$$k^2 = \frac{3a}{4(1+a)}, \qquad c^2 = 1+a. \tag{3.10}$$

To find solitary wave solutions numerically for $F \neq 0$, we adopt a Lobatto IIIA method to solve the nonlinear ordinary differential equation (3.4). Notice that an explicit method such as a 4th-order Runge-Kutta method cannot be used because $x = 0$ is a fixed point. For the following ordinary differential equation

$$\frac{dy}{dt} = f(t,y), \quad \text{with initial condition} \quad y(0) = y_0,$$

the Lobatto IIIA method which is a 4th-order implicit method is given by

$$\begin{aligned}
y_{n+1} &= y_n + \frac{\Delta t}{6}\left(k_1 + 4k_2 + k_3\right), \\
k_1 &= f(t_n, y_n), \\
k_2 &= f(t_n + \frac{\Delta t}{2}, y_n + \frac{5}{24}k_1 + \frac{1}{3}k_2 - \frac{1}{24}k_3), \\
k_3 &= f(t_n + \Delta t, y_n + \frac{1}{6}k_1 + \frac{2}{3}k_2 + \frac{1}{6}k_3).
\end{aligned}$$

We first test the Lobatto IIIA method for the case of $F = 0$:

$$\frac{d\zeta}{dx} = -\frac{\sqrt{3}\zeta}{c}\sqrt{c^2 - 1 - \zeta}, \quad \text{with} \quad \zeta(0) = a, \tag{3.11}$$

for which its analytical solution is known as

$$\zeta(x,t) = a\ \mathrm{sech}^2[k(x - ct)].$$

As shown in Figure 3.2, the maximum relative error is found to be less than 10^{-11} and our numerical method is believed to be accurate to compute the solitary wave solutions.

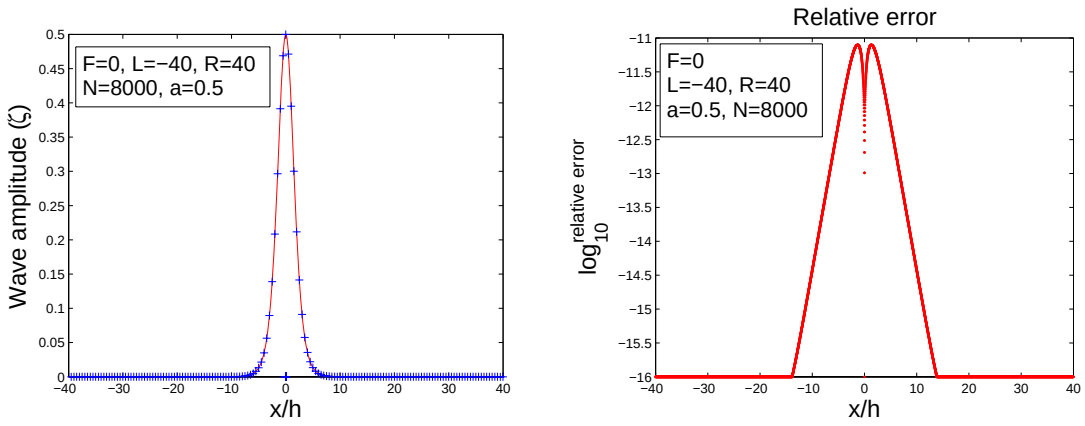

Figure 3.2 In the left panel, the analytical solution of (3.11) (solid line) is compared with the numerical solution (+) using a Lobatto IIIA method. The right panel shows the relative error between the analytical solution and the numerical solution.

The numerical solutions of (3.11) for solitary waves in the presence of background shear ($F \neq 0$) are shown in Figure 3.3 for $a = 0.5$. We can see that the downstream-propagating solitary wave is steeper than the upstream-propagating solitary wave with the same physical parameters. More detailed characteristics of solitary wave solutions in uniform shear flows can be found in [7]. Here we study their dynamics numerically, as described in the followings.

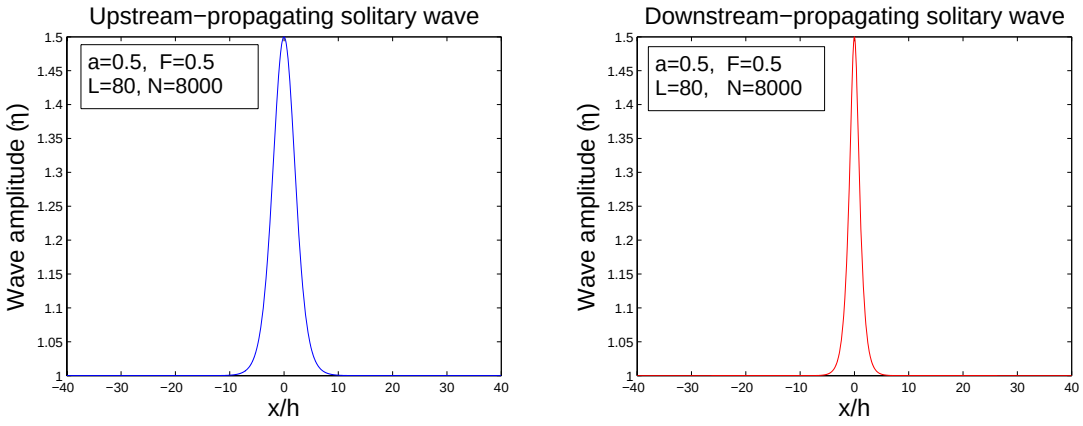

Figure 3.3 Solitary wave solutions for the presence of shear (F=0.5). Left panel: the upstream-propagating solitary wave ($c < 0$); Right panel: the downstream-propagating solitary wave ($c > 0$). The wave amplitude $a = 0.5$; the Froude number F=0.5; the number of grids N=8000, and the length of the computational domain L=80.

3.3 A Numerical Method to Solve the One-dimensional Equations

Before solving the nonlinear time evolution equations given by (3.1)–(3.2), we will first find an efficient and accurate numerical method for the linearized evolution equations.

After introducing small perturbations η' and u' to the steady solutions $\eta_0 = 1$ and $u_0 = 0$ of equations (3.1)–(3.2), we assume $\eta = 1+\eta'$ and $u = u'$. By substituting these expressions for η and u into equations (3.1)–(3.2) and neglecting the higher-order terms in η' and u', the linearized evolution equations can be obtained as

$$\eta_t + F\eta_x + u_x = 0, \tag{3.12}$$

$$\left(u - \frac{1}{3}u_{xx}\right)_t = -\eta_x + \frac{F}{3}u_{xxx}. \tag{3.13}$$

For simplicity, we choose $F = 0$ and equations (3.12)–(3.13) become

$$\eta_t = -u_x, \quad \left(u - \frac{u_{xx}}{3}\right)_t = -\eta_x. \tag{3.14}$$

When we use a finite difference method to solve the linearized equations given by (3.14), we have two different choices for the arrangement of equally spaced grid points: (1) evaluate η and u on the same grid points; (2) evaluate u on the grid points,

but η in the middle of two grid points. To make a better choice, we will compare the dispersion relationship of the continuous system with that of the discretized system based on these two different grid arrangements.

After substituting the expansions of η and u given by the following equations into the linearized equations (3.14)

$$\eta\left(x,t\right)=a_0e^{i(kx-\omega t)},\quad u\left(x,t\right)=b_0e^{i(kx-\omega t)},$$

we obtain the dispersion relationship for the continuous system:

$$\omega_1\left(k\right)=\sqrt{\frac{3k^2}{3+k^2}}.$$

On the other hand, by substituting with $x_j=j\Delta x$ with Δx being the grid size, the dispersion relation for the discrete system with grid (1) can be found as

$$\omega_2\left(k\right)=\frac{\sqrt{3}\sin\left(k\triangle x\right)}{\sqrt{3\triangle x^2-2\left(\cos k\triangle x-1\right)}},$$

while that with grid (2) is given by

$$\omega_3\left(k\right)=\frac{2\sqrt{3}\sin\frac{k\triangle x}{2}}{\sqrt{3\triangle x^2-2\left(\cos k\triangle x-1\right)}}.$$

When these dispersion relationships (ω_1, ω_2, and ω_3) are compared in Figure 3.4, we can see that ω_3 matches with ω_1 better than ω_2, which means that the staggered grid system for η and u should be chosen.

With the staggered grid, we use a 4th-order finite difference method with periodic boundary conditions to approximate the first-order and second-order spatial derivatives:

$$\frac{df}{dx}=\frac{f(x-2\triangle x)-8f(x-\triangle x)+8f(x+\triangle x)-f(x+2\triangle x)}{12\triangle x}+O(\triangle x^4),$$

$$\frac{d^2f}{dx^2}=\frac{-f(x-2\triangle x)+16f(x-\triangle x)-30f(x)+16f(x+\triangle x)-f(x+2\triangle x)}{12\triangle x}+O(\triangle x^4).$$

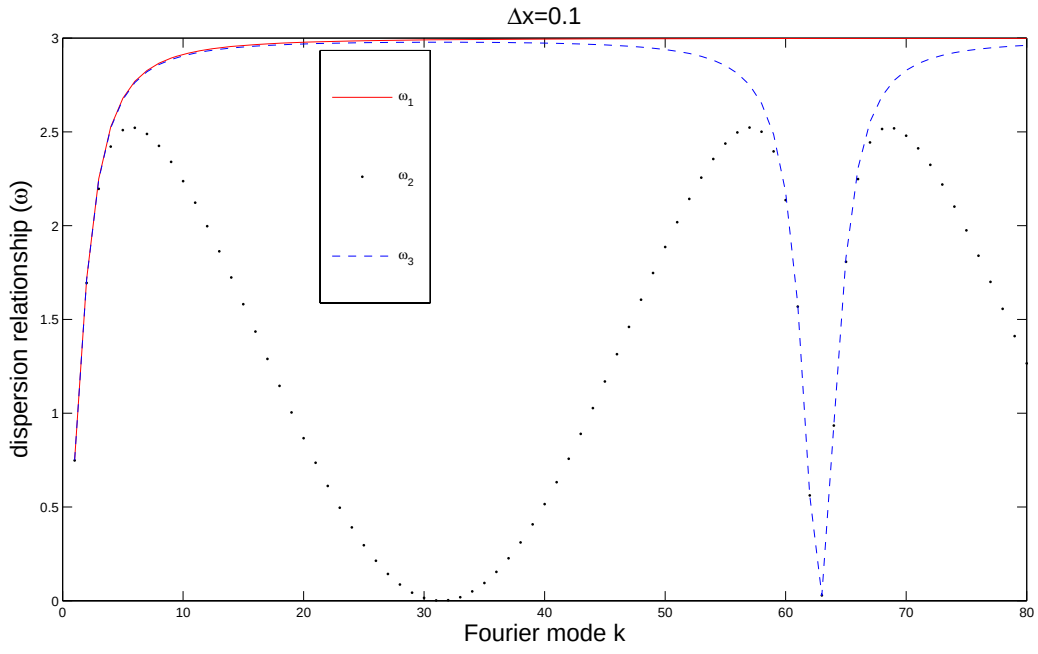

Figure 3.4 Comparison of dispersion relationships: ω_1: solid line; ω_2: dotted line; ω_3: dashed line.

To be consistent with our spatial discretization, we use a 4th-order predictor and corrector Admas-Bashforth method in time, which can be written as

$$\text{the predictor}: p_{n+1} = y_n + \frac{\triangle t}{24}\left(-9f_{n-3} + 37f_{n-2} - 59f_{n-1} + 55f_n\right),$$
$$\text{the corrector}: y_{n+1} = y_n + \frac{\triangle t}{24}\left[f_{n-2} - 5f_{n-1} + 19f_n + 9f\left(t_{n+1}, p_{n+1}\right)\right],\ n = 3, \cdots,$$

where

$$\frac{dy}{dt} = f\left(t, y\right), \quad \text{with initial condition} \quad y\left(0\right) = y_0.$$

Since this is a multi-step method, we use a 4th-order Runge-Kutta method to find the solutions at the first three time steps.

To validate our numerical model by solving the linearized equations (3.14), we consider the following initial conditions

$$\eta\left(x,0\right)=\cos x,\quad u\left(x,0\right)=\sqrt{\frac{3}{4}}\cos x, \tag{3.15}$$

for which the analytical solutions of the linearized equations are given by

$$\eta\left(x,t\right)=\cos\left(x-\sqrt{\frac{3}{4}}t\right),\quad u\left(x,t\right)=\sqrt{\frac{3}{4}}\cos\left(x-\sqrt{\frac{3}{4}}t\right). \tag{3.16}$$

As shown in Figure 3.5, our numerical solutions compare well with the analytical solutions and the maximum error is $O(10^{-8})$.

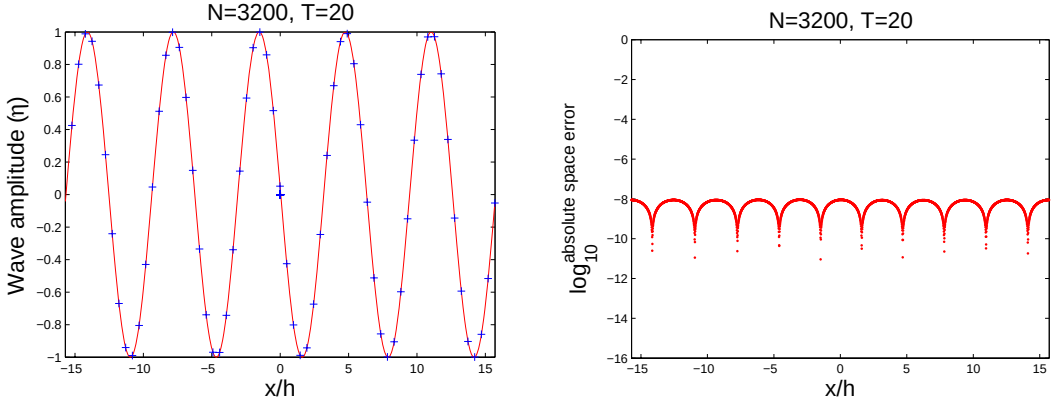

Figure 3.5 In the left panel, the numerical solution (+) is compared with the analytical solution (solid line). In the right panel, the absolute error between the numerical solution and the analytical solution at time $T = 20$ is shown. In this computation, $\triangle t = 0.001$ and the computational domain is 10π.

We also tested the convergence of our numerical method which has 4th-order accuracy in both space and time. Nevertheless the numerical error in space is greater than that in time since we have to choose $\triangle t$ much smaller than $\triangle x$ to satisfy the CFL condition i.e., $c\triangle t/\triangle x < 1$, where c is the wave speed. $\triangle t$ is the time step, and $\triangle x$ is the grid size in space. Therefore, after fixing the time step to be $\triangle t = 0.001$, we reduce $\triangle x$ and compare the numerical solutions at $T = 5$ with the analytical solutions given by (3.16). As shown in Figure 3.6, $\log_{10}^{\text{absolute error}}$ (where we use the

infinite norm to estimate the absolute error) varies linearly with $\log_{10}^{\triangle x}$ and the slope is close to 4, as expected.

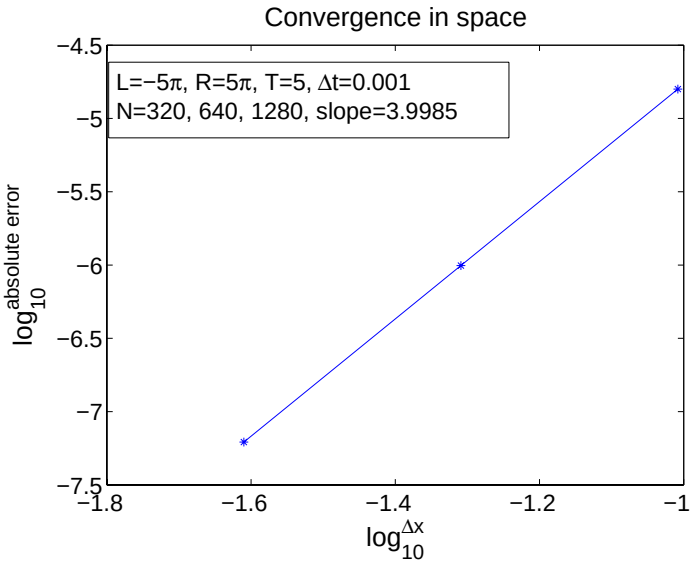

Figure 3.6 Convergence in space with reducing $\triangle x$ for a fixed time step $\triangle t = 0.001$.

Since our finite difference method is found satisfactory, it is used to solve the nonlinear evolution equations given by (3.1)–(3.2). For our numerical computations, it is convenient to rewrite (3.1)–(3.2) as

$$\eta_t = -\left(\frac{F}{2}\eta^2 + \eta u\right)_x, \tag{3.17}$$

$$\left(\eta u - \eta^2\eta_x u_x - \frac{\eta^3}{3}u_{xx}\right)_t = -\eta\left(uu_x + \eta_x\right) - u\left(\frac{F}{2}\eta^2 + \eta u\right)_x + H_x, \tag{3.18}$$

where (3.17) has been used to obtain (3.18) from (3.2), and

$$H = \left(\frac{F}{2}\eta^2 + \eta u\right)_x \eta^2 u_x + \frac{\eta^3}{3}\left(uu_{xx} - u_x^2 + F\eta u_{xx}\right).$$

As discussed previously, we evaluate u at grid i, but η at grid $\left(i + \frac{1}{2}\right)$ when the independent variables are discretized as $x_i = i\triangle x$ and $t_n = n\triangle t$, where $i = 1, 2, \cdots\cdots N$ is the grid number and $n = 1, 2 \cdots M$ is the number of time steps. Then we use a 4th-order finite difference scheme to approximate spatial derivatives with

respect to x, as described before. At time step n, we use a 4th-order explicit and implicit Adams-Bashforth method to integrate (3.17)–(3.18) in time t to find $\eta_{i+\frac{1}{2}}^{(n+1)}$ and $w_i^{(n+1)}$ where $w(\eta, u) = \eta u - \eta^2 \eta_x u_x - \frac{\eta^3}{3} u_{xx}$. Then, $u_i^{(n+1)}$ is found by inverting a pentacyclic matrix.

As discussed in Section 3.2, the traveling wave solutions of equations (3.1)–(3.2) are known and, therefore, we can validate our numerical method by comparing our numerical solutions of the time evolution equations given by (3.17)–(3.18) with the periodic traveling wave solutions, since we use periodic boundary conditions.

For $F = 0$, the periodic solutions of the governing equations (3.1)–(3.2) are given by

$$\zeta(x,t) = \alpha \ \mathrm{cn}^2 \left[\frac{\sqrt{3\beta}}{2c} (x - ct) \right], \tag{3.19}$$

$$u(x,t) = \frac{c\zeta(x,t)}{1 + \zeta(x,t)}, \tag{3.20}$$

with the wave period λ is given by

$$\lambda = \frac{4c}{\sqrt{3\beta}} \int_0^{\frac{\pi}{2}} \frac{d\theta}{\sqrt{1 - \frac{\alpha}{\beta} \sin^2 \theta}}, \tag{3.21}$$

where $\eta(x) = 1 + \zeta(x)$ and cn is the conoidal function. α is the wave amplitude, and β is the other parameter satisfying equation $\alpha < \beta < 1 + \beta$. The wave speed c satisfies the following equation $c^2 = (1 + \alpha)(1 + \alpha - \beta)$.

Numerical solutions compared with periodic solutions are shown in Figure 3.7. The maximum relative error between the numerical solutions and periodic solutions is less than 10^{-8} at $T = 100$, as shown in Figure 3.8. We also show the convergence in space in Figure 3.9. Notice that $\log_{10}^{\text{relative error}}$ varies linearly with $\log_{10}^{\triangle x}$ and the slope is 3.986, as we expected.

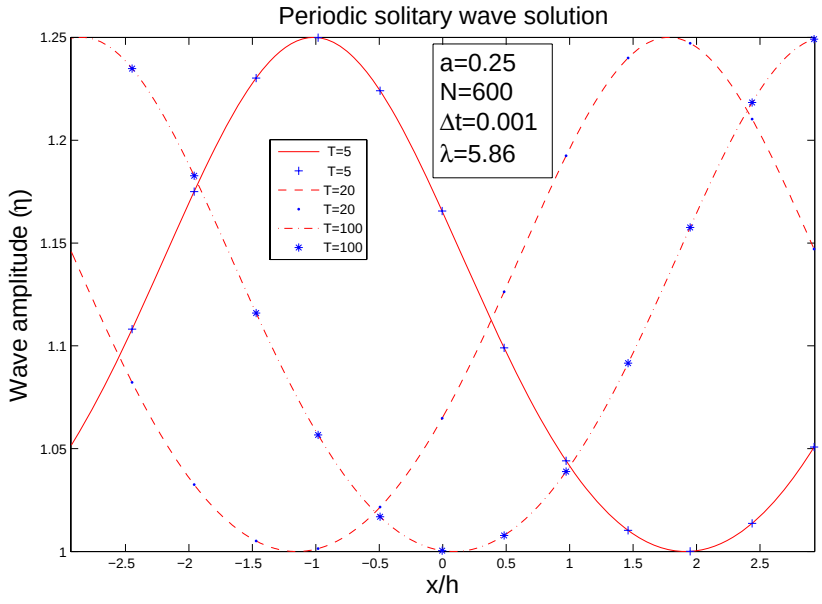

Figure 3.7 The periodic solutions of the equation (3.19) at time $T = 5$ $(+)$, $T = 20$ $(\cdot)$, and $T = 100$ $(*)$ are compared with the numerical solutions at time $T = 5$ (solid line), $T = 20$ (dash line), and $T = 100$ (dot dash line), respectively.

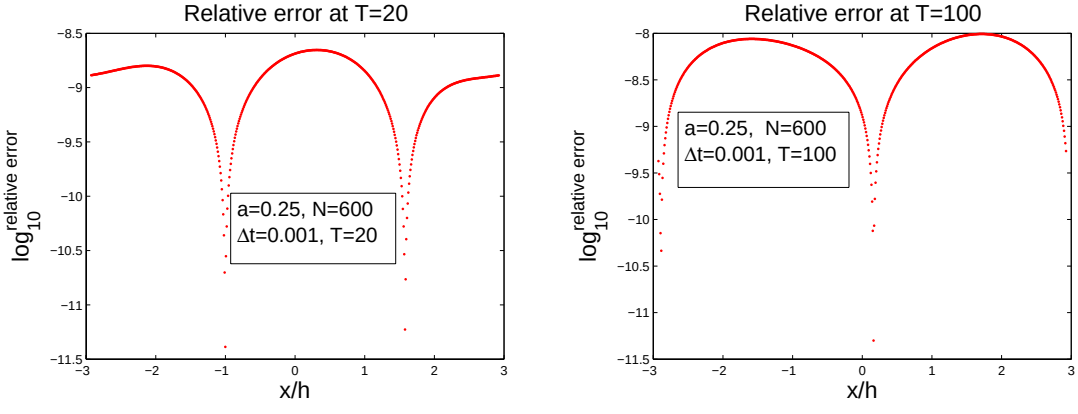

Figure 3.8 From left to right, two panels represent the relative error between the numerical solutions and the periodic solutions with $F = 0$ at $T = 20$ and $T = 100$, respectively.

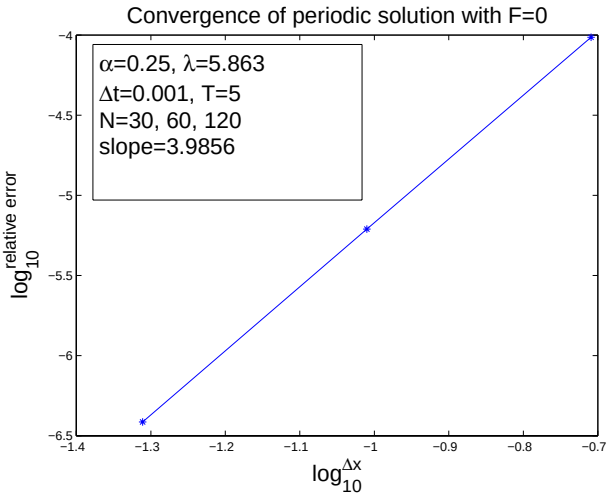

Figure 3.9 Convergence in space of the periodic solutions with reducing $\triangle x$ for fixing time step of $\triangle t = 0.001$, where $F = 0$, $T = 5$, $\triangle x = 0.2,\ 0.1,\ 0.05$, respectively.

For $F \neq 0$, the solitary wave solutions of the governing equations (3.1)–(3.2) can be found from

$$\left(\frac{d\zeta}{dx}\right)^2 = \frac{\zeta^2 N\left[\zeta\right]}{\left(D\left[\zeta\right]\right)^2},$$

with an initial condition

$$\zeta\left(0\right) = a,$$

where a is the wave amplitude. c is the wave speed, and

$$D\left[\zeta\right] = \zeta^2 + 2\zeta + 2\left(1 - \frac{c}{F}\right),\ N\left[\zeta\right] = -\zeta^2 - \left(4 + \frac{12}{F^2}\right)\zeta + \frac{12}{F^2}\left(c^2 - Fc - 1\right).$$

Because of background shear, the downstream-propagating solitary waves ($c > 0$) are steeper than the upstream-propagating solitary waves ($c < 0$), as shown in [7]. It is therefore more difficult to solve the evolution equations for the downstream-propagating solitary waves than the upstream-propagating solitary waves. As shown in Figure 3.11 and 3.14, the relative errors of our numerical solutions compared with the analytic solutions are greater for the downstream-propagating solitary waves. For

fixed wave amplitude a, we can see that if $F^2 < \frac{12}{3a^3+9a^2+8a}$, the denominator of $D[\zeta]$ vanishes for some value of ζ, the slope of downstream-propagating solitary waves become infinite, and we have a difficulty in solving it numerically. On the other hand, for upstream-propagating solitary waves, no such difficulty arises.

For upstream-propagating solitary waves, we choose

$$c = \frac{F}{2} - \sqrt{1 + a + \frac{F^2}{12}(a^2 + 4a + 3)}.$$

Comparison between numerical solutions and analytical solutions of the upstream-propagating solitary waves are shown in Figure 3.10. The maximum relative error between the numerical solutions and the analytical solutions is less than 10^{-9} as shown in Figure 3.11. We also show the convergence in space in Figure 3.12: $\log_{10}^{\text{relative error}}$ varies linearly with $\log_{10}^{\triangle x}$ and the slope is 3.996, as we expected.

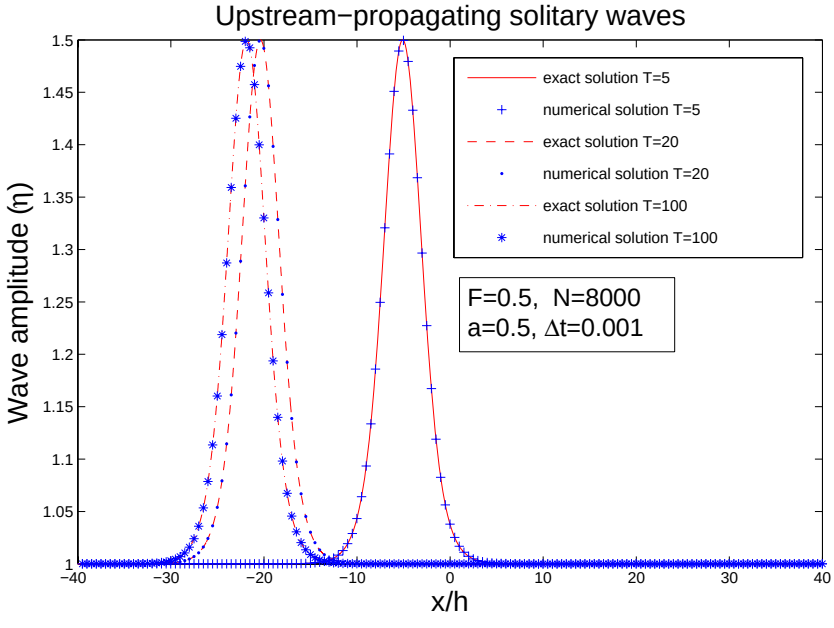

Figure 3.10 The analytical solutions of the upstream-propagating solitary waves at time $T = 5$ $(+)$, $T = 20$ $(\cdot)$, and $T = 100$ $(*)$ are compared with the numerical solutions at time $T = 5$ (solid line), $T = 20$ (dash line), and $T = 100$ (dot dash line), respectively.

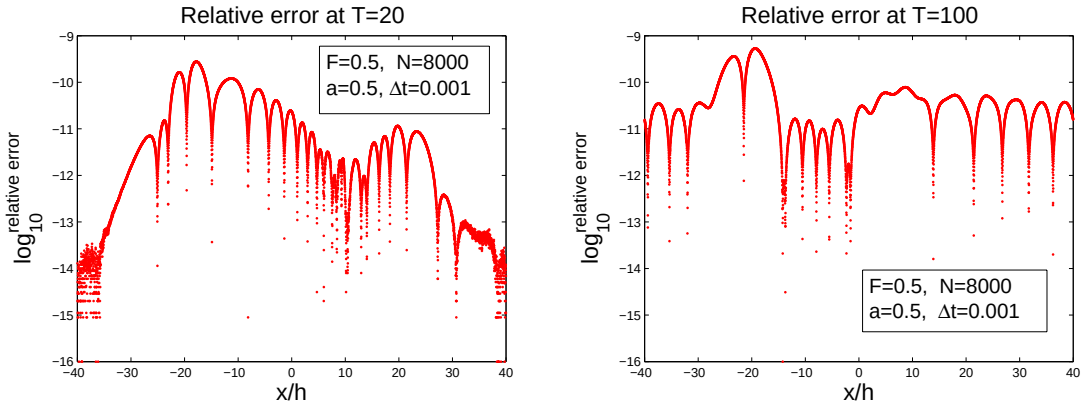

Figure 3.11 From left to right, these figures represent the relative error between the numerical solutions and the analytical solutions of upstream-propagating solitary waves with $F = 0.5$ at $T = 20$ and $T = 100$, respectively.

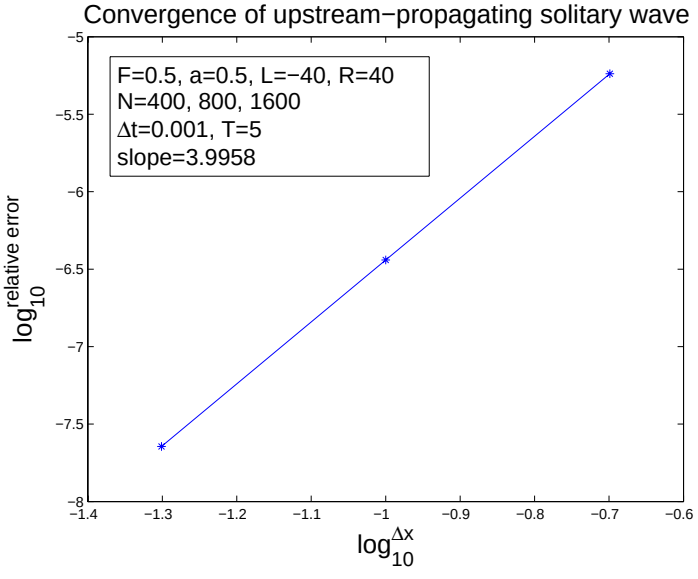

Figure 3.12 Convergence in space of the upstream-propagating solitary waves with reducing $\triangle x$ for fixing time step of $\triangle t = 0.001$, where $F = 0.5$, $T = 5$, $\triangle x = 0.2,\ 0.1,\ 0.05$, respectively.

For downstream-propagating solitary waves, we choose

$$c = \frac{F}{2} + \sqrt{1 + a + \frac{F^2}{12}(a^2 + 4a + 3)}.$$

Comparison between numerical solutions and analytical solutions are shown in Figure 3.13. The maximum relative error between the numerical solutions and the analytical solutions is less than 10^{-7} as shown in Figure 3.14. We also show the convergence in space in Figure 3.15: $\log_{10}^{\text{relative error}}$ varies linearly with $\log_{10}^{\triangle x}$ and the slope is 3.881, as we expected.

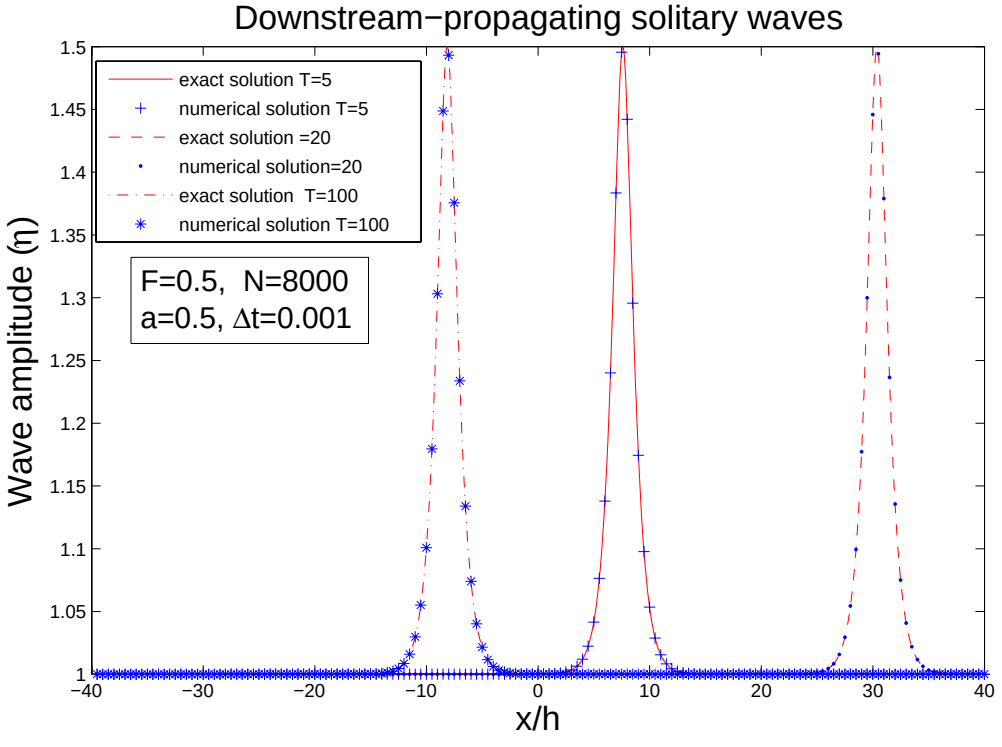

Figure 3.13 The analytical solutions of the downstream-propagating solitary waves at time $T = 5$ $(+)$, $T = 20$ $(\cdot)$, and $T = 100$ $(*)$ are compared with the numerical solutions at time $T = 5$ (solid line), $T = 20$ (dash line), and $T = 100$ (dot dash line), respectively.

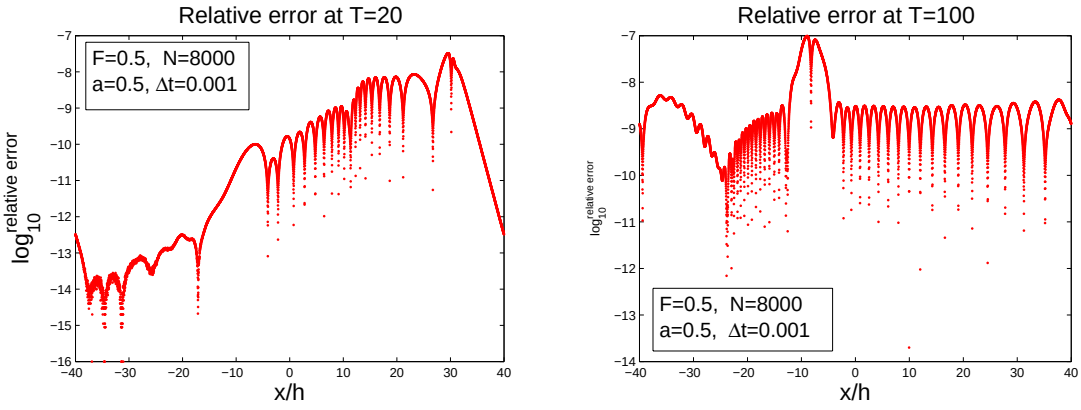

Figure 3.14 From left to right, these figures represent the relative error between the numerical solutions and the analytical solutions of the downstream-propagating solitary waves with $F = 0.5$ at $T = 20$ and $T = 100$, respectively.

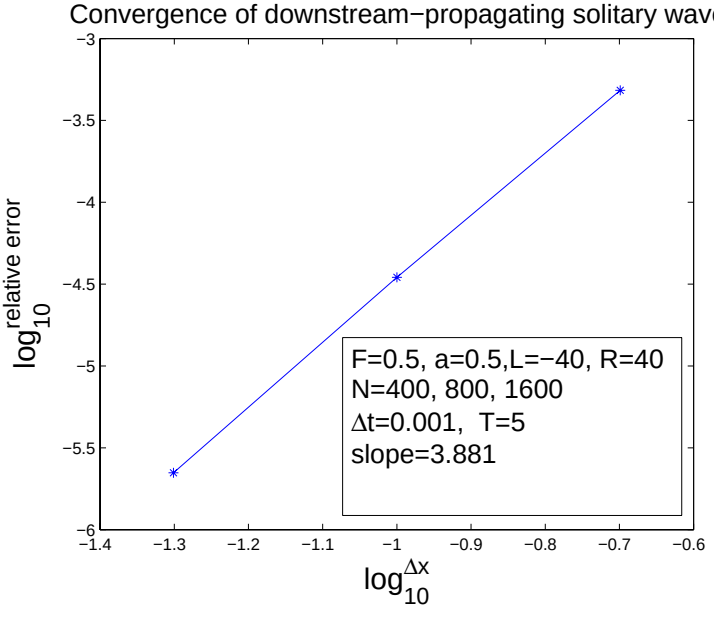

Figure 3.15 Convergence in space of the downstream-propagating solitary waves with reducing $\triangle x$ for fixing time step of $\triangle t = 0.001$, where $F = 0.5$, $T = 5$, $\triangle x = 0.2,\ 0.1,\ 0.05$, respectively.

We also notice that equations (3.1)–(3.2) can be written in conserved forms given by

$$\eta_t + F\eta\eta_x + (\eta u)_x = 0, \tag{3.22}$$

$$\left(u + \frac{1}{6}\eta^2 u_{xx}\right)_t + \left(\frac{1}{2}u^2 + \eta\right)_x = H_x, \tag{3.23}$$

$$\left(\eta u + \frac{F}{2}\eta^2\right)_t + \left(\eta u^2 + \frac{1}{2}\eta^2 + F\eta^2 u + \frac{F^2}{3}\eta^3\right)_x = G_x, \tag{3.24}$$

where

$$H = \frac{\eta^2}{2}\left(u_{xt} + \frac{2}{3}uu_{xx} - u_x^2 + \frac{2}{3}F\eta u_{xx}\right), \tag{3.25}$$

$$G = \frac{\eta^3}{3}\left(u_{xt} + uu_{xx} - u_x^2 - u_x^2 + F\eta u_{xx}\right). \tag{3.26}$$

After integrating these three conservation equations with respect to x over the interval $[-L,L]$, respectively, we have

$$\frac{\partial}{\partial t}\int_{-L}^{L} \eta \, dx = 0, \tag{3.27}$$

$$\frac{\partial}{\partial t}\int_{-L}^{L} \left(u + \frac{1}{6}\eta^2 u_{xx}\right) dx = 0, \tag{3.28}$$

$$\frac{\partial}{\partial t}\int_{-L}^{L} \left(\eta u + \frac{F}{2}\eta^2\right) dx = 0, \tag{3.29}$$

where we use periodic boundary conditions

$$\eta(-L,t) = \eta(L,t), \quad u(-L,t) = u(L,t).$$

Then we have conservation of mass:

$$\int_{-L}^{L} \eta \, dx,$$

conservation of vorticity:

$$\int_{-L}^{L} \left(u + \frac{1}{6}\eta^2 u_{xx}\right) dx,$$

and conservation of horizontal momentum:

$$\int_{-L}^{L} \left(\eta u + \frac{F}{2} \eta^2 \right) dx.$$

In order to test conservation laws, we use the trapezoidal rule to take integration numerically. For $F = 0.5$, the numerical results of the conservation of mass, horizontal momentum and vorticity of the upstream-propagating and downstream-propagating solitary waves are shown from Figure 3.16 to Figure 3.18, respectively. All these quantities are conserved with relative error less than 10^{-11}, as we expected.

So far, we can claim that our numerical method is reliable based on the numerical results of the convergence, the maximum relative error and the conservation law as shown before.

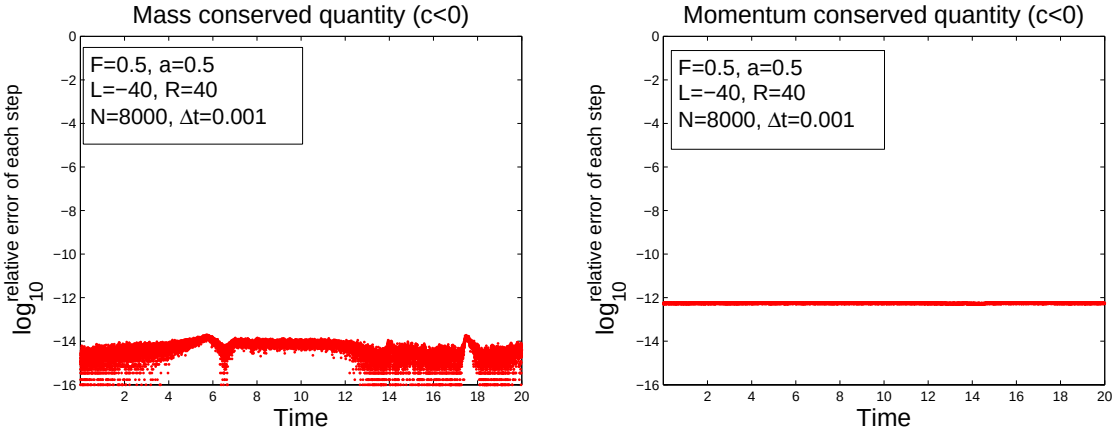

Figure 3.16 Mass conserved quantity and momentum conserved quantity of the up-stream propagating solitary waves are shown in the left panel and right panel at time $T = 20$ with relative error about 10^{-14} and 10^{-12}, respectively. Where $F = 0.5$, $a = 0.5$, $\triangle t = 0.001$, and $\triangle x = 0.01$.

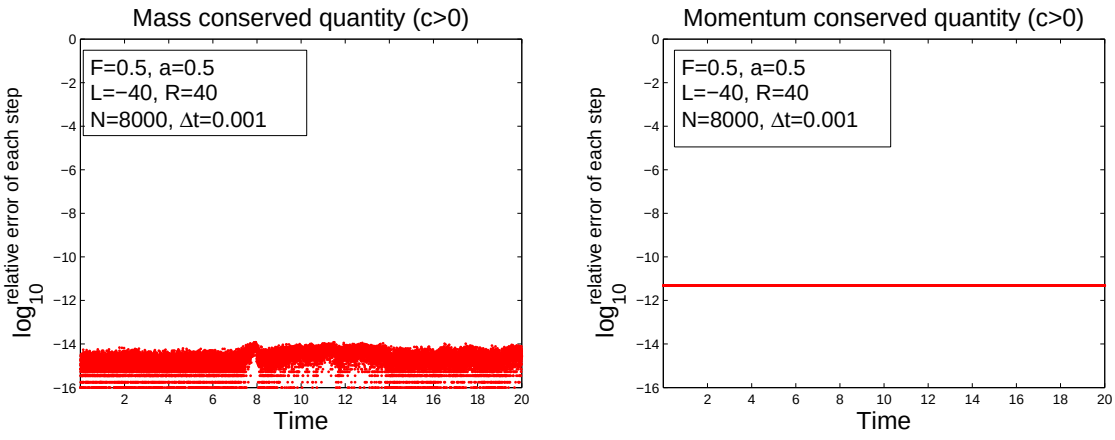

Figure 3.17 Mass conserved quantity and momentum conserved quantity of the down-stream propagating solitary waves are shown in the left panel and right panel at time $T = 20$ with relative error about 10^{-14} and 10^{-11}, respectively. Where $F = 0.5$, $a = 0.5$, $\triangle t = 0.001$, and $\triangle x = 0.01$.

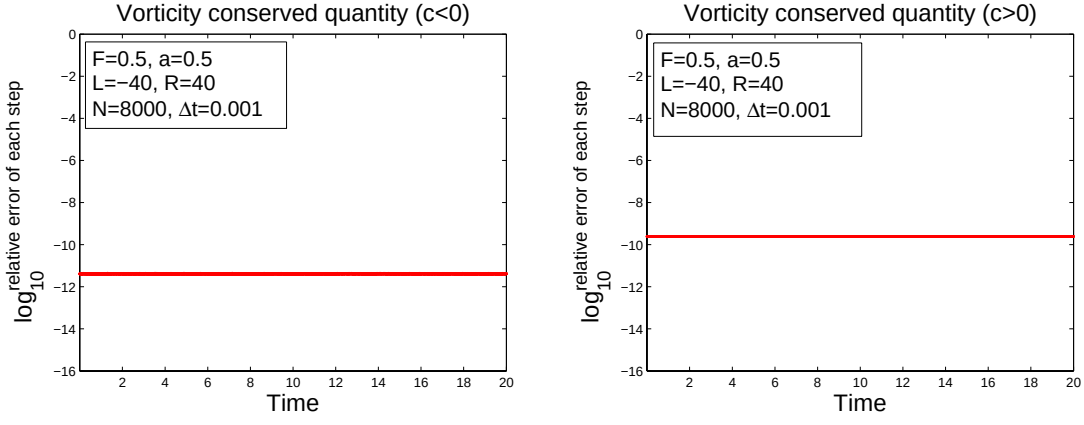

Figure 3.18 Vorticity conserved quantity of the upstream-propagating and downstream propagating solitary waves at time $T = 20$ are shown in the left panel and right panel with relative error about 10^{-11} and 10^{-10}, respectively. Where $F = 0.5$, $a = 0.5$, $\triangle t = 0.001$, and $\triangle x = 0.01$.

3.4 Weakly Nonlinear Analysis for Wave Interactions in Uniform Shear Flows

A weakly nonlinear bidirectional long wave model without shear was studied by Wu [37], and applied to evaluate interactions between multiple solitary waves propagating in both directions in a uniform channel of rectangular cross-section. In particular, the detailed processes of the head-on and overtaking collisions are described in detail [38]. Here we first generalize his analysis to the model with uniform shear. Then we will use this model to investigate the interaction of solitary waves, including head-on and overtaking collision in an uniform shear flow.

In order to obtain a weakly nonlinear bidirectional long wave model in an uniform shear flow, we assume that $\alpha = \frac{a}{h} \ll 1$, $\epsilon = \frac{h}{\lambda} \ll 1$, and $\alpha = O(\epsilon^2)$ (a is the wave amplitude. h is the water depth and λ is the wavelength). Then the weakly nonlinear long wave model [7] is given by

$$\zeta_t + F(1+\zeta)\zeta_x + [(1+\zeta)u]_x = 0, \tag{3.30}$$

$$u_t + uu_x + \zeta_x = \frac{1}{3}(u_{xxt} + Fu_{xxx}), \tag{3.31}$$

where the subscripts x and t denote derivatives with respect to x and t, respectively. F is the Froude number. ζ is the surface elevation and u is the depth-averaged horizontal velocity.

We introduce a velocity potential ϕ where $u = \phi_x$. After substituting $u = \phi_x$ into equation (3.31) and integrating it once time, we can obtain the following equation

$$\zeta + \phi_t + \frac{1}{2}\phi_x^2 - \frac{1}{3}(\phi_{xxt} + F\phi_{xxx}) = 0. \tag{3.32}$$

Then, substituting $u = \phi_x$ and equation (3.32) into equation (3.30) to eliminate ζ, at last we obtain the equation for ϕ:

$$\phi_{tt} - \phi_{xx} + F\phi_{xt} = \frac{\phi_{xxtt} + 2F\phi_{xxxt} + F^2\phi_{xxxx}}{3} - \left(\phi_x^2 + \frac{1}{2}\phi_t^2\right)_t - \left(\frac{F}{2}\phi_x^2\right)_x. \tag{3.33}$$

In deriving equation (3.33), we have used $\phi_{xx} = \phi_{tt} + F\phi_{xt}$ to convert the quadratic term $(\phi_t\phi_x)_x$ into $\phi_x\phi_{xt}+\phi_t\phi_{tt}+F\phi_t\phi_{xt}$ without changing the order of approximation.

Now we use a multiple scale method to expand equation (3.33) in terms of new variables

$$X_+ = \epsilon\left(t - \frac{1}{\beta_1}x\right),\ X_- = \epsilon\left(t - \frac{1}{\beta_2}x\right),\ \tau = \epsilon^3 t,$$

with

$$\phi(x,t) = \epsilon\left[\phi_0(X_+, X_-, \tau) + \epsilon^2\phi_1(X_+, X_-, \tau) + \cdots\right], \tag{3.34}$$

where $\beta_1 = \frac{F}{2} + \sqrt{1 + \frac{F^2}{4}}$ and $\beta_2 = \frac{F}{2} - \sqrt{1 + \frac{F^2}{4}}$. The corresponding differential operators are related by

$$\partial_x = \epsilon\left(\beta_2\partial_+ + \beta_1\partial_-\right),\ \partial_t = \epsilon\left(\partial_+ + \partial_- + \epsilon^2\partial_\tau\right),$$

where

$$\partial_+ = \frac{\partial}{\partial X_+},\ \partial_- = \frac{\partial}{\partial X_-},\ \partial_\tau = \frac{\partial}{\partial \tau}.$$

With this asymptotic expansion, substituting equation (3.34) into equation (3.33) yields the leading order term of $O(\epsilon^3)$:

$$\left(4 + F^2\right)\partial_+\partial_-\phi_0 = 0, \tag{3.35}$$

which has the general solution

$$\phi_0 = \phi_+(X_+, \tau) + \phi_-(X_-, \tau). \tag{3.36}$$

In equation (3.36), ϕ_+ and ϕ_- represent the right-going and left-going waves, respectively, and will be determined later.

The next order term of $O(\epsilon^5)$ is given by

$$
\begin{aligned}
&\left(4+F^2\right)\partial_+\partial_-\phi_1 = \\
&-(2+F\beta_2)\,\partial_\tau\partial_+\phi_+ - \left(\frac{1}{2}+\beta_2^2+\frac{F}{2}\beta_2^3\right)\partial_+\left(\partial_+\phi_+\right)^2 + \frac{1}{3}\left(\beta_2^2+2F\beta_2^3+F^2\beta_2^4\right)\partial_+^4\phi_+ \\
&-(2+F\beta_1)\,\partial_\tau\partial_-\phi_- - \left(\frac{1}{2}+\beta_1^2+\frac{F}{2}\beta_1^3\right)\partial_-\left(\partial_-\phi_-\right)^2 + \frac{1}{3}\left(\beta_1^2+2F\beta_1^3+F^2\beta_1^4\right)\partial_-^4\phi_- \\
&+\left[(F\beta_2-1)\,\partial_+ + (F\beta_1-1)\,\partial_-\right]\left(\partial_+\phi_+\right)\left(\partial_-\phi_-\right). \qquad (3.37)
\end{aligned}
$$

The solvability condition to prevent ϕ_1 from growing linearly with increasing X_+ or X_- requires that the secular terms on the right-hand side of the equation (3.37) vanish separately with respect to X_+ and X_-. Then we have

$$\partial_\tau\partial_+\phi_+ + \frac{\left(\frac{1}{2}+\beta_2^2+\frac{F}{2}\beta_2^3\right)}{2+F\beta_2}\partial_+\left(\partial_+\phi_+\right)^2 - \frac{\left(\beta_2^2+2F\beta_2^3+F^2\beta_2^4\right)}{3\left(2+F\beta_2\right)}\partial_+^4\phi_+ = 0, \qquad (3.38)$$

$$\partial_\tau\partial_-\phi_- + \frac{\left(\frac{1}{2}+\beta_1^2+\frac{F}{2}\beta_1^3\right)}{2+F\beta_1}\partial_-\left(\partial_-\phi_-\right)^2 - \frac{\left(\beta_1^2+2F\beta_1^3+F^2\beta_1^4\right)}{3\left(2+F\beta_1\right)}\partial_+^4\phi_+ = 0, \qquad (3.39)$$

$$\left(4+F^2\right)\partial_+\partial_-\phi_1 = \left[(F\beta_2-1)\,\partial_+ + (F\beta_1-1)\,\partial_-\right]\left(\partial_+\phi_+\right)\left(\partial_-\phi_-\right). \qquad (3.40)$$

For the surface elevation, we expand $\zeta(X_+, X_-, \tau)$ as

$$\zeta(X_+, X_-, \tau) = \epsilon^2\left[\zeta_+(X_+,\tau) + \zeta_-(X_-,\tau) + \epsilon^2\zeta_1(X_+, X_-, \tau) + \cdots\right].$$

After substituting the expansion of ϕ and ζ into equation (3.32), the leading order term of $O(\epsilon^2)$ gives that $\zeta(x,t) = \phi_t(x,t)$, and, from equation (3.34) and equation (3.36), we can obtain

$$\zeta_\pm(X_\pm,\tau) = -\partial_\pm\phi_\pm(X_\pm,\tau). \qquad (3.41)$$

The next order term of $O(\epsilon^4)$ is given by

$$
\begin{aligned}
\zeta_1 \;=& -\left(\partial_+ + \partial_-\right)\phi_1 - \partial_\tau\left(\phi_+ + \phi_-\right) + \zeta_+\zeta_- \\
&-\frac{1}{2}\left(\beta_2^2\zeta_+^2 + \beta_1^2\zeta_-^2\right) - \frac{1}{3}\left[\left(\beta_2^2+F\beta_2^3\right)\partial_+^2\zeta_+ + \left(\beta_1^2+F\beta_1^3\right)\partial_-^2\zeta_-\right]. \qquad (3.42)
\end{aligned}
$$

And we also have following relationships

$$\partial_\tau \phi_+ = \frac{1}{2+F\beta_2}\left[\left(\frac{1}{2}+\beta_2^2+\frac{F}{2}\beta_2^3\right)\zeta_+^2+\frac{1}{3}\left(\beta_2^2+2F\beta_2^3+F^2\beta_2^4\right)\partial_+^2\zeta_+\right], \quad (3.43)$$

$$\partial_\tau \phi_- = \frac{1}{2+F\beta_1}\left[\left(\frac{1}{2}+\beta_1^2+\frac{F}{2}\beta_1^3\right)\zeta_-^2+\frac{1}{3}\left(\beta_1^2+2F\beta_1^3+F^2\beta_1^4\right)\partial_-^2\zeta_-\right], \quad (3.44)$$

$$\phi_1 = \frac{1}{4+F^2}\left[\left(F\beta_2-1\right)\phi_-\zeta_+ + \left(F\beta_1-1\right)\phi_+\zeta_-\right] + A_+(X_+) + A_-(X_-), \quad (3.45)$$

where equation (3.43)–(3.44) are the first integrals of equations (3.38)–(3.39). Equation (3.45) is obtained by integrating equation (3.40) with two arbitrary integral constants $A_+(X_+)$ and $A_-(X_-)$. To finalize the resulting equations, we must assure that arbitrary initial conditions can be prescribed for ζ up to $O(\epsilon^4)$. This requirement is fulfilled if the terms in equation (3.42) with $\zeta_\pm^2$ and $\partial_\pm^2\zeta_\pm$ are cancelled by choosing appropriately complementary parts of $A_\pm$. With this condition satisfied, we obtain the final expression for ζ_1 as

$$\zeta_1 = \frac{1}{4+F^2}\left[\left(1-F\beta_2\right)\phi_-\partial_+\zeta_+ + \left(1-F\beta_1\right)\phi_+\partial_-\zeta_-\right] + \frac{2+2F^2}{4+F^2}\zeta_+\zeta_-. \quad (3.46)$$

We therefore have bidirectional long wave model:

$$\zeta(x,t) = \zeta_+(x,t) + \zeta_-(x,t) + \zeta_1(x,t), \quad (3.47)$$

$$\zeta_+ = \beta_1\partial_x\phi_+, \quad \zeta_- = \beta_2\partial_x\phi_-, \quad (3.48)$$

$$\zeta_1 = \frac{\beta_1\left(F\beta_2-1\right)\phi_-\partial_x\zeta_+ + \beta_2\left(F\beta_1-1\right)\phi_+\partial_x\zeta_-}{4+F^2} + \frac{2+2F^2}{4+F^2}\zeta_+\zeta_-, \quad (3.49)$$

$$D_1\zeta_+ + \frac{\beta_1\left(\frac{1}{2}+\beta_2^2+\frac{F}{2}\beta_2^3\right)}{2+F\beta_2}\partial_x\zeta_+^2 + \frac{\beta_1^3\left(\beta_2^2+2F\beta_2^3+F^2\beta_2^4\right)}{3\left(2+F\beta_2\right)}\partial_x^3\zeta_+ = 0, \quad (3.50)$$

$$D_2\zeta_- + \frac{\beta_2\left(\frac{1}{2}+\beta_1^2+\frac{F}{2}\beta_1^3\right)}{2+F\beta_1}\partial_x\zeta_-^2 + \frac{\beta_2^3\left(\beta_1^2+2F\beta_1^3+F^2\beta_1^4\right)}{3\left(2+F\beta_1\right)}\partial_x^3\zeta_- = 0, \quad (3.51)$$

where $D_1 = \partial_t + \beta_1\partial_x$, and $D_2 = \partial_t + \beta_2\partial_x$.

It also can be expressed in terms of $X_+,\ X_-$ and τ as

$$\zeta = \zeta_+(X_+,\tau) + \zeta_-(X_-,\tau) + \zeta_1(X_+,X_-,\tau), \tag{3.52}$$

$$\zeta_\pm = -\partial_\pm \phi_\pm, \tag{3.53}$$

$$\zeta_1 = -\frac{(F\beta_2 - 1)\,\phi_-\partial_+\zeta_+ + (F\beta_1 - 1)\,\phi_+\partial_-\zeta_-}{4+F^2} + \frac{2+2F^2}{4+F^2}\zeta_+\zeta_-, \tag{3.54}$$

$$\partial_\tau\zeta_+ - \frac{\frac{1}{2}+\beta_2^2+\frac{F}{2}\beta_2^3}{2+F\beta_2}\partial_+\zeta_+^2 - \frac{\beta_2^2+2F\beta_2^3+F^2\beta_2^4}{3\,(2+F\beta_2)}\partial_+^3\zeta_+ = 0, \tag{3.55}$$

$$\partial_\tau\zeta_- - \frac{\frac{1}{2}+\beta_1^2+\frac{F}{2}\beta_1^3}{2+F\beta_1}\partial_-\zeta_-^2 - \frac{\beta_1^2+2F\beta_1^3+F^2\beta_1^4}{3\,(2+F\beta_1)}\partial_-^3\zeta_- = 0. \tag{3.56}$$

We also can rewrite equation (3.47) equivalently with the same order of approximation as

$$\begin{aligned}\zeta = {} & \zeta_+(X_+ + \frac{1-F\beta_2}{4+F^2}\phi_-,\tau) + \zeta_-(X_- + \frac{1-F\beta_1}{4+F^2}\phi_+,\tau) \\ & + \frac{2+2F^2}{4+F^2}\zeta_+(X_+,\tau)\zeta_-(X_-,\tau).\end{aligned} \tag{3.57}$$

Now we can use this bidirectional long wave model to investigate the interaction of solitary waves in an uniform shear flow. We first consider the head-on collision between two solitons, ζ_+ and ζ_-, of arbitrary amplitudes, α_+ and α_-, respectively. We define c_{11}, c_{12}, c_{21}, and c_{22} as following

$$c_{11} = \frac{\frac{1}{2}+\beta_1^2+\frac{F}{2}\beta_1^3}{2+F\beta_1}, \quad c_{12} = \frac{\beta_1^2+2F\beta_1^3+F^2\beta_1^4}{3\,(2+F\beta_1)}, \tag{3.58}$$

$$c_{21} = \frac{\frac{1}{2}+\beta_2^2+\frac{F}{2}\beta_2^3}{2+F\beta_2}, \quad c_{22} = \frac{\beta_2^2+2F\beta_2^3+F^2\beta_2^4}{3\,(2+F\beta_2)}. \tag{3.59}$$

Since equations (3.55)–(3.56) for $\zeta_\pm$ in an uniform shear flow are uncoupled, they have the classical KdV solutions given by

$$\zeta_+ = \alpha_+\mathrm{sech}^2\theta_+, \quad \theta_+ = \left(\frac{c_{21}\alpha_+}{6c_{22}}\right)^{1/2}\left(X_+ + \frac{2\alpha_+c_{21}}{3}t + s_+\right), \tag{3.60}$$

$$\zeta_- = \alpha_-\mathrm{sech}^2\theta_-, \quad \theta_- = \left(\frac{c_{11}\alpha_-}{6c_{12}}\right)^{1/2}\left(X_- + \frac{2\alpha_-c_{11}}{3}t + s_-\right), \tag{3.61}$$

$$\phi_+ = -\left(\frac{6c_{22}\alpha_+}{c_{21}}\right)^{1/2}\tanh\theta_+, \quad \phi_- = -\left(\frac{6c_{12}\alpha_-}{c_{11}}\right)^{1/2}\tanh\theta_-, \tag{3.62}$$

where $s_\pm$ are arbitrary phase constants for the initial position of each soliton, and $\phi_\pm$ are integrals of equation (3.53), with their integration constants incorporated with $s_\pm$ in the argument of $\zeta_\pm$. From equation (3.57), it can be seen that the maximum amplitude occurs at $\theta_+ = \theta_- = 0$, and is given by

$$\zeta_{\max} = \alpha_+ + \alpha_- + \frac{2+2F^2}{4+F^2}\alpha_+\alpha_-. \tag{3.63}$$

If we set $s_\pm = 0$, the maximum wave amplitude $\zeta_{\max}$ appears at $x = 0$ and $t = 0$.

Two interacting solitons are continuously retarded from their own individual phase lines. From equations (3.60)–(3.62), we obtain the total phase shift through the head-on collision for $\zeta_\pm$, which can be expressed in terms of the terminal time retardation (for fixed x) as

$$\begin{aligned}\triangle t_+ &= -\frac{1-F\beta_2}{4+F^2}\left[\phi_-\left(\theta_+ = 0, t = \infty\right) - \phi_-\left(\theta_+ = 0, t = -\infty\right)\right] \\ &= \frac{2\left(1-F\beta_2\right)}{4+F^2}\left(\frac{6c_{12}}{c_{11}}\alpha_-\right)^{1/2}, \end{aligned} \tag{3.64}$$

$$\begin{aligned}\triangle t_- &= -\frac{1-F\beta_1}{4+F^2}\left[\phi_+\left(\theta_- = 0, t = \infty\right) - \phi_+\left(\theta_- = 0, t = -\infty\right)\right] \\ &= \frac{2\left(1-F\beta_1\right)}{4+F^2}\left(\frac{6c_{22}}{c_{21}}\alpha_+\right)^{1/2}. \end{aligned} \tag{3.65}$$

Similarly, we can express the phase shift in terms of space retardation (for fixed t) as

$$\triangle x_+ = -\triangle t_+ = -\frac{2\left(1-F\beta_2\right)}{4+F^2}\left(\frac{6c_{12}}{c_{11}}\alpha_-\right)^{1/2}, \tag{3.66}$$

$$\triangle x_- = \triangle t_- = \frac{2\left(1-F\beta_1\right)}{4+F^2}\left(\frac{6c_{22}}{c_{21}}\alpha_+\right)^{1/2}. \tag{3.67}$$

Thus the time retardation of one wave is proportional to the square-root of the wave amplitude of the other. As both solitons are retarded during the collision, the decrease in total kinetic energy must be offset by an equal and opposite increase in the potential energy. This increase arises in the quadratic term $\frac{2+2F^2}{4+F^2}\zeta_+\zeta_-$ which makes the resultant wave height greater than the sum of ζ_+ and ζ_- upon merging. This

particular nonlinear effect fades out rapidly before and after the encounter, leaving the phase shift as the only permanent nonlinear mark of the collision event.

Next we use the bidirectional long wave model to investigate overtaking collision between two or more solitary waves. We first treat the general case when there are m right-going solitons and n left-going solitons propagating along the real x-axis as a soliton street. Since the KdV equations (3.55)–(3.56) are uncoupled, we can evaluate ζ_+ and ζ_- separately by applying Hirota's method [17]. Here we adopt the transformation (e.g. [35], §17.2)

$$\zeta_\pm = -\partial_\pm \phi_+, \quad \phi_+ = -\frac{6c_{22}}{c_{21}}\partial_+ \left(\log f^+\right), \quad \phi_- = -\frac{6c_{12}}{c_{11}}\partial_- \left(\log f^-\right), \tag{3.68}$$

where c_{11}, c_{12}, c_{21}, and c_{22} are defined in equations (3.58)–(3.59).

Substituting equation (3.68) into equations (3.55)–(3.56), we have

$$\left(f^+_X - f^+\partial_X\right)\left(f^+_\tau - c_{22}f^+_{XXX}\right) + 3c_{22}\left[\left(f^+_{XX}\right)^2 - f^+_X f^+_{XXX}\right] = 0, \tag{3.69}$$

$$\left(f^-_X - f^-\partial_X\right)\left(f^-_\tau - c_{12}f^-_{XXX}\right) + 3c_{12}\left[\left(f^-_{XX}\right)^2 - f^-_X f^-_{XXX}\right] = 0, \tag{3.70}$$

where we omit subindices $\pm$ for X_+ and X_-, respectively, as understood. For a single soliton, we know that

$$f^\pm = 1 + f^\pm_j, \qquad (j = 1), \tag{3.71}$$

$$f^+_j = \exp(\theta^+_j), \quad \theta^+_j = \gamma_j\left(X_+ + s_j\right) + \gamma_j^3 c_{22} t, \tag{3.72}$$

$$f^-_j = \exp(\theta^-_j), \quad \theta^-_j = \gamma_j\left(X_- + s_j\right) + \gamma_j^3 c_{12} t, \tag{3.73}$$

where γ_j is a real parameter and s_j is an arbitrary phase constant. $f^\pm$ are general solutions of equation (3.62). From equations (3.60)–(3.61), $\zeta_\pm$ can be obtained as

$$\zeta_+ = \frac{3c_{22}\gamma_j^2}{2c_{21}}\mathrm{sech}^2\left(\frac{\theta^+_j}{2}\right), \tag{3.74}$$

$$\zeta_- = \frac{3c_{12}\gamma_j^2}{2c_{11}}\mathrm{sech}^2\left(\frac{\theta^-_j}{2}\right). \tag{3.75}$$

For the general system of m right-going solitons and n left-going solitons, we take Hirota solutions [17] for each of ζ_+ and ζ_-:

$$\zeta_+ = -\partial_+\phi_+, \quad \zeta_- = -\partial_-\phi_-, \tag{3.76}$$

$$\phi_+ = -\frac{6c_{22}}{c_{21}}\partial_+\left(\log f^+\right), \quad \phi_- = -\frac{6c_{12}}{c_{11}}\partial_-\left(\log f^-\right), \tag{3.77}$$

$$f^\pm = \det|f^\pm_{jk}|, \qquad f^\pm_{ik} = \delta_{jk} + \frac{2\gamma_j}{\gamma_j+\gamma_k}f^\pm_j, \tag{3.78}$$

where δ_{jk} is Kronecker's delta, $f^\pm_j$ are given by equations (3.72)–(3.73). The determinant is that of the $m \times m$ matrix of $[f^+_{jk}]$ $(j,k = 1,2,\cdots,m)$ for ζ_+ and that of the $n \times n$ matrix of $[f^-_{jk}]$ $(j,k = 1,2,\cdots,n)$ for ζ_-. The resultant wave profile is given by equation (3.57).

As a simple example for the overtaking collision between two right-going solitary waves with different wave amplitudes α_1 and α_2 with $\alpha_1 > \alpha_2$ i.e., $\gamma_1 > \gamma_2$, we choose $m = 2$ and set $f^- = 0$ to eliminate all left-going waves. From equations (3.76)–(3.78), we have

$$f^+_j = \exp(\theta_j), \quad \theta_j = \gamma_j\left(X_+ + s_j\right) + \gamma_j^3 c_{j2}t, \quad j = 1,2, \tag{3.79}$$

$$f^+ = 1 + f^+_1(X_+,\tau) + f^+_2(X_+,\tau) + a_{12}f^+_1(X_+,\tau)f^+_2(X_+,\tau), \tag{3.80}$$

$$\zeta = \zeta_+ = -\partial_+\phi_+, \quad \phi_+ = -\frac{6c_{22}}{c_{21}}\partial_+\left(\log f^+\right), \tag{3.81}$$

where a_{12} is given by

$$a_{12} = \left(\frac{\gamma_1-\gamma_2}{\gamma_1+\gamma_2}\right)^2.$$

After simplification, in terms of x and t

$$\zeta(x,t) = \frac{6c_{22}}{c_{21}}\frac{\gamma_1^2 f^+_1 + \gamma_2^2 f^+_2 + f^+_{12}}{\left(1 + f^+_1 + f^+_2 + a_{12}f^+_1 f^+_2\right)^2}, \tag{3.82}$$

where f^+_{12} is defined as

$$f^+_{12} = 2\left(\gamma_1-\gamma_2\right)^2 f^+_1 f^+_2 + a_{12}\left[\gamma_1^2 f^+_1 (f^+_2)^2 + \gamma_2^2 (f^+_1)^2 f^+_2\right].$$

From equation (3.82), it is easy to determine that as $t \to -\infty$, the peak of ζ_1 falls on

$$x = \beta_1 \left[\left(1 + c_{22}\gamma_1^2\right) t + s_1 \right],$$

and the peak of ζ_2 falls on

$$x = \beta_1 \left[\left(1 + c_{22}\gamma_2^2\right) t + s_2 + \frac{1}{\gamma_2} \log(a_{12}) \right].$$

As $t \to +\infty$, the peak of ζ_1 falls on

$$x = \beta_1 \left[\left(1 + c_{22}\gamma_1^2\right) t + s_1 + \frac{1}{\gamma_1} \log(a_{12}) \right],$$

and the peak of ζ_2 falls on

$$x = \beta_1 \left[\left(1 + c_{22}\gamma_2^2\right) t + s_2 \right].$$

Thus, we can see that a greater soliton overtaking a smaller one gains momentum, having accelerated forward with a forward phase shift $\triangle x_1 = \frac{\beta_1}{\gamma_1} \log(a_{12})$, while the smaller one suffering a backward phase shift $\triangle x_2 = \frac{\beta_1}{\gamma_2} \log(a_{12})$, and the interaction occurs in the neighborhood of

$$t = \frac{s_1 - s_2}{c_{22}\left(\gamma_2^2 - \gamma_1^2\right)},\ x = \frac{\left(c_{22}\gamma_2^2 + 1\right) s_1 - \left(c_{22}\gamma_1^2 + 1\right) s_2}{c_{22}\left(\gamma_2^2 - \gamma_1^2\right)}.$$

If we choose $s_j = -\frac{\log(a_{12})}{2\gamma_j},\ j = 1, 2$, then at $t = 0$, we know $\zeta(x, 0) = \zeta(-x, 0)$ and

$$f_j^+(x, 0) = a \exp\left(-\frac{\gamma_j}{\beta_1} x\right),\quad j = 1, 2,$$

where a is given by

$$a^2 = \frac{1}{a_{12}} \quad \text{i.e.,} \quad a = \frac{\gamma_1 + \gamma_2}{\gamma_1 - \gamma_2}.$$

After some straightforward manipulation, we find that

$$\zeta(0,0) = \alpha_1 - \alpha_2, \tag{3.83}$$

$$\zeta_x(0,0) = 0, \tag{3.84}$$

$$\zeta_{xx}(0,0) = \frac{-c_{21}}{3c_{22}\beta_1^2}(\alpha_1 - \alpha_2)(\alpha_1 - 3\alpha_2), \tag{3.85}$$

where $\alpha_j = \frac{3c_{22}}{2c_{21}}\gamma_j^2$ $(j = 1, 2)$ are the original wave amplitudes of ζ_j, and, during the above procedure, we assume $\alpha_1 > \alpha_2$ i.e., $\gamma_1 > \gamma_2$. Equation (3.85) provides the critical amplitude ratio $\frac{\alpha_1}{\alpha_2} = 3$. If $\frac{\alpha_1}{\alpha_2} > 3$, then the two solitary waves merge into one single peak wave, whereas for $1 < \frac{\alpha_1}{\alpha_2} < 3$, the two solitary waves remain separated (i.e., we can see two wave peaks all the time during the interaction). At the critical condition of $\frac{\alpha_1}{\alpha_2} = 3$, the single peak becomes flattened with zero curvature. From equation (3.83), we know that the wave elevation at the center of symmetry $x = 0$ and $t = 0$ is $\alpha_1 - \alpha_2$, just the difference between the two initial wave amplitudes.

For the overtaking collision between two left-going solitary waves, we have the same results just replace c_{21} by c_{11}, c_{22} by c_{12} and β_1 by β_2 in equations (3.79)–(3.85).

3.5 Numerical Simulation of Solitary Wave Interaction

The interaction of small amplitude solitary waves including head-on and overtaking collisions has been studied extensively in the absence of background shear using the weakly nonlinear models such as the KdV equation and the Boussinesq equations [16, 17, 21, 22, 32, 34, 40, 41, 42]. The interaction of large amplitude solitary waves has been also investigated by solving numerically the Euler equations, and the strongly nonlinear long wave models such as the Su-Gardner equations [11, 24, 25, 29, 31, 43]. In the presence of shear, we already have presented weakly nonlinear analysis for the wave interaction. Now we will describe our numerical solutions for the interaction of strongly nonlinear solitary waves in uniform shear flows. By comparing our numerical solutions with weakly nonlinear analysis, we show the effects of strong nonlinearity and shear on the interactions. In particular, the detailed procedure of the wave interaction will be illustrated for head-on and overtaking collisions between two solitary waves of wave amplitudes a_1 and a_2.

3.5.1 Head-on Collision of Two Solitary Waves

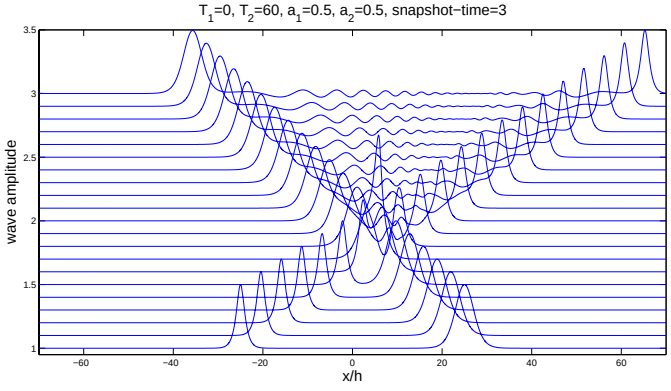

Figure 3.19 Head-on collision of two solitary waves with $a_1 = a_2 = 0.5$ for $F = 0.5$.

When $F \neq 0$, we can see that the behavior of head-on collision between two solitary waves is quite similar to that for $F = 0$. Before they collide, two solitary

waves maintain the initial shapes, and, then, they will merge into one single peak wave with wave amplitude larger than $a_1 + a_2$. After their interaction, oscillatory tails are observed as shown in Figure 3.19. This indicates that the strongly nonlinear model is not integrable and the interaction is inelastic.

From the weakly nonlinear analysis, we learned that the maximum wave amplitude during the head-on collision is estimated as $\zeta_{\max} = a_1 + a_2 + \frac{2+2F^2}{4+F^2} a_1 a_2$. For $F = 0$, from the numerical solution of the strongly nonlinear model, the maximum wave amplitude is found larger than the maximum value given by the weakly analysis, because of the effect of higher order nonlinearity. For example, if $a_1 = 0.5$ and $a_2 = 0.5$, $a_1 + a_2 + \frac{a_1 a_2}{2} = 1.125$ which is less than 1.1504, the computed maximum value at $t = 21$. On the other hand, when $F \neq 0$, the maximum wave amplitude is smaller than the maximum value predicted by the weakly nonlinear analysis, because of the background shear. For example, if $a_1 = 0.5$ and $a_2 = 0.5$, $a_1 + a_2 + \frac{2+2F^2}{4+F^2} a_1 a_2 = 1.1471$ which is greater than 1.136, the computed maximum value at $t = 20.3$. These results are shown in Figure 3.20.

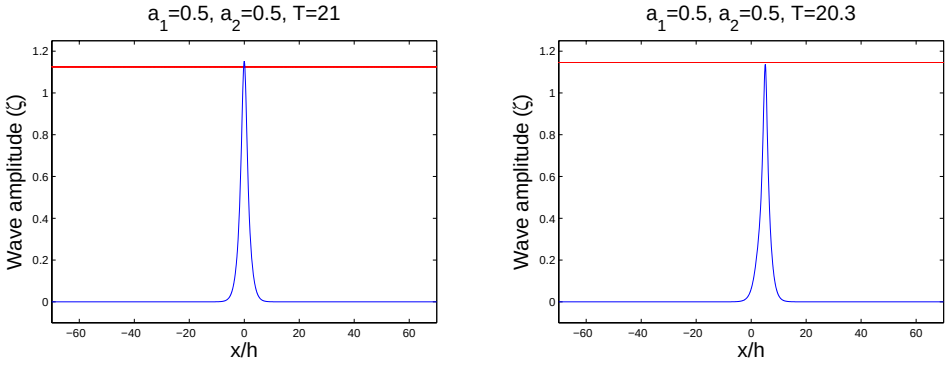

Figure 3.20 The surface wave profile during the head-on collision with $a_1 = a_2 = 0.5$ for $F = 0$ and $F = 0.5$ are shown in the left and right panels, respectively, and the maximum wave amplitude are measured at $T = 21$ and $T = 20.3$ numerically as well. The flat solid lines are the predicted maximum values from the weakly nonlinear analysis.

From the weakly nonlinear analysis, we also know that phase shift is the only permanent nonlinear mark of the collision event. When $F = 0$, the phase shift in x for the right going wave is $\triangle x_+ = -\sqrt{\frac{a_-}{3}}$ and for the left going wave is $\triangle x_- = \sqrt{\frac{a_+}{3}}$, where a_+ and a_- are the wave amplitudes of the right-going and left-going waves, respectively. When we choose the wave amplitudes of the right-going and left-going waves as $a_1 = 0.5$, $a_2 = 0.5$, respectively, the absolute value of the phase shift after the head-on collision is 0.705 at $T = 60$, which is larger than $\triangle x_- = |\triangle x_+| = 0.408$ given by the weakly nonlinear analysis, as shown in Figure 3.21.

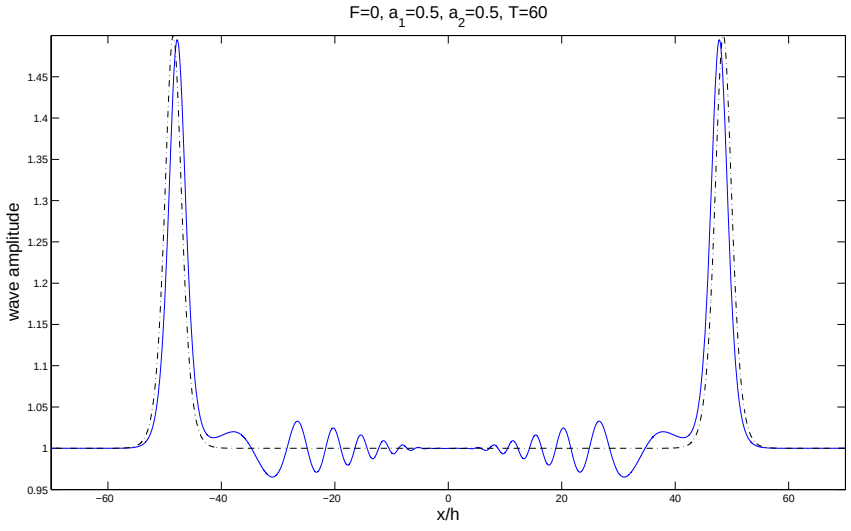

Figure 3.21 Symmetric phase shift for the right-going and left-going waves for $F = 0$, $a_1 = 0.5$ and $a_2 = 0.5$. Where the solid line is the numerical result after head-on collision and the dash dot line is the solitary wave solution without head-on collision at time $T = 60$.

When $F \neq 0$, (in the presence of the background shear), the phase shift in x for the right-going wave is $\triangle x_+ = -\frac{2(1-F\beta_2)}{4+F^2}\sqrt{\frac{6c_{12}a_-}{c_{11}}}$ and for the left going wave is $\triangle x_- = \frac{2(1-F\beta_1)}{4+F^2}\sqrt{\frac{6c_{22}a_+}{c_{21}}}$, where β_1, β_2, c_{11}, c_{12}, c_{21}, and c_{22} are defined as before. Notice that these phase shifts are no longer symmetric since the solitary waves of the same amplitude are different, depending on the wave propagation direction. When we choose $F = 0.5$, the wave amplitudes of the right-going and left-going waves as

$a_1 = 0.5$, $a_2 = 0.5$, respectively, after head-on collision, at $T = 60$, the absolute value of the phase shift for the right-going wave is 0.837, which is smaller than $|\triangle x_+| = 0.842$, however, the absolute phase shift value for the left-going wave is 0.437, which is larger than $\triangle x_- = 0.081$ as shown in Figure 3.22.

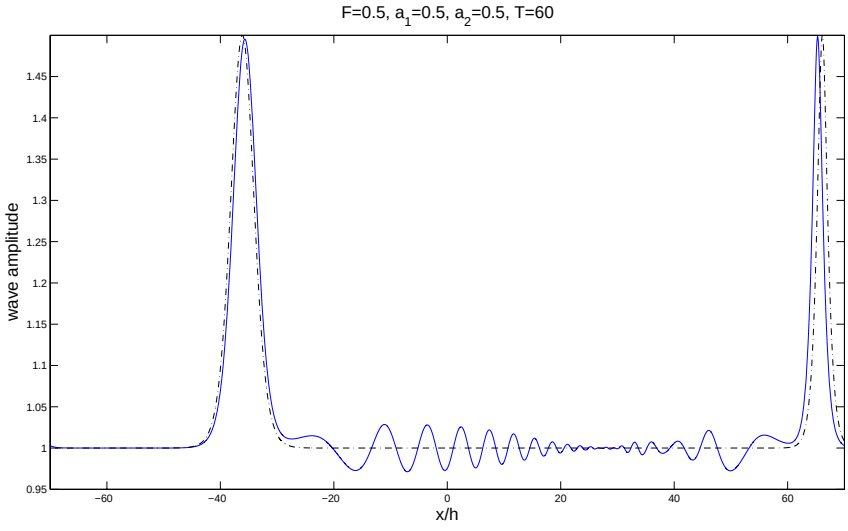

Figure 3.22 Asymmetric phase shift for the right-going and left-going waves for $F = 0.5$, $a_1 = 0.5$ and $a_2 = 0.5$. Where the solid line is the numerical result after head-on collision and the dash dot line is the solitary wave solution without head-on collision at time $T = 60$.

3.5.2 Overtaking Collision of Two Solitary Waves

For overtaking collision between two solitary waves of the KdV equation, it is well known that, the two waves can either remain separated or merge into one single peak wave during the collision depending on the ratio of wave amplitudes. From the weakly analysis presented in [35, 37], the critical amplitude ratio is 3.

Overtaking collision of strongly nonlinear solitary waves without shear is studied numerically in [24]. It was shown that when the amplitude ratio is smaller than 3 ($a_1/a_2 = 1.8$), two waves never merge into a single peak, however, when the amplitude ratio is larger than 3 ($a_1/a_2 = 7.8$), the larger wave merges into the smaller wave to

form a single peak during the interaction and the amplitude of the merged peak is smaller than the amplitude of the larger wave.

After studying overtaking collision of strongly nonlinear solitary waves numerically in uniform shear flows (i.e., $F \neq 0$), we can show that whether two solitary waves merge into one single peak wave also depends on a critical amplitude ratio as shown below.

Figure 3.23 shows overtaking collision of two upstream-propagating solitary waves with wave amplitudes $a_1 = 0.4$ and $a_2 = 0.2$ for $F = 0.5$. Notice that with this amplitude ratio $\frac{a_1}{a_2} = 2$, in this case, two waves never merge into a single peak wave.

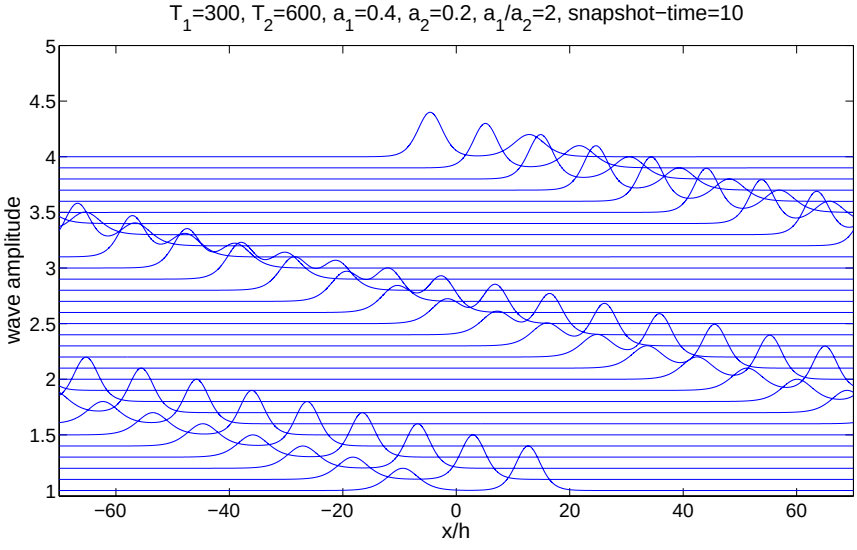

Figure 3.23 Overtaking collision of two solitary waves between $T_1 = 300$ and $T_2 = 600$ with $F = 0.5$, $a_1 = 0.4$, and $a_2 = 0.2$.

In Figure 3.24, we show that overtaking collision of two upstream-propagating solitary waves with wave amplitudes $a_1 = 0.4$ and $a_2 = 0.08$ for $F = 0.5$. Notice that with this amplitude ratio $\frac{a_1}{a_2} = 5$, in this case, two waves will merge into a single peak wave during the overtaking collision.

For overtaking collision of downstream-propagating solitary waves, we can get similar results as upstream-propagating solitary waves: when the amplitude ratio is

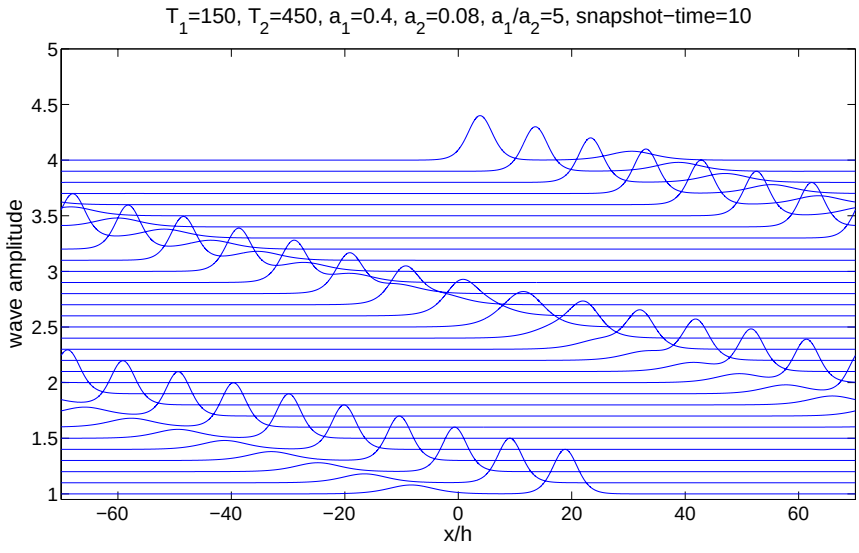

Figure 3.24 Overtaking collision of two solitary waves between $T_1 = 150$ and $T_2 = 450$ with $F = 0.5,\ a_1 = 0.4,$ and $a_2 = 0.08$.

smaller than the critical amplitude ratio, two solitary waves remain separated; and when the amplitude ratio is larger than the critical amplitude ratio, two solitary waves merge into one single peak wave during the overtaking collision, however, the critical amplitude ratios are differents for the same Froude number F.

From weakly nonlinear analysis, the critical number for overtaking collision only depends on the ratio of wave amplitude, if the ratio is larger than this critical number, then two solitary waves will merge into a single peak wave during the interaction, if the ratio is smaller than this critical number, then two solitary waves never merge into a single peak wave. If the amplitude ratio is equal to this critical number, then two solitary waves merge into a single wave with flat peak [35, 37]. However, for strongly nonlinear solitary waves, we can show numerically that this critical number not only depends on the amplitude ratio, but also depends on wave amplitudes, the Froude number F, and the direction of the wave propagation, as shown below.

For $F = 0$, fixing ratio $\frac{a_1}{a_2} = 3.4$ with different wave amplitudes a_1 and a_2, after numerical simulation, we can see that when $a_1 = 0.4$ and $a_2 = 0.1176$, two solitary

waves will merge into a single wave with flat peak; when $a_1 = 0.8$ and $a_2 = 0.2353$, two wave peaks remain separated. This implies that the critical number depends on the wave amplitudes and the results are shown in Figure 3.25 and Figure 3.26.

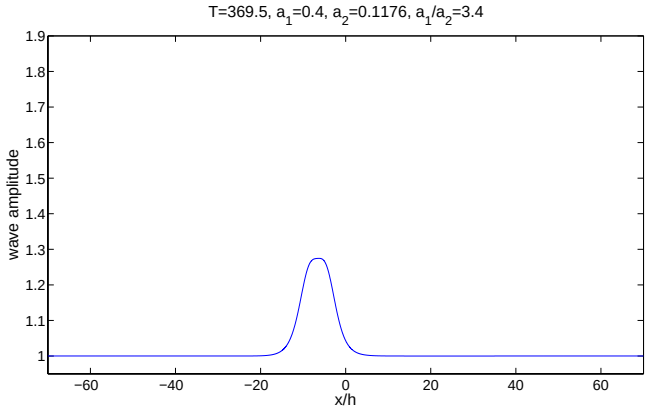

Figure 3.25 Two solitary waves merge into a single wave with flat peak during the overtaking collision at time $T = 369.5$. Where $F = 0$, $a_1 = 0.4$, and $a_2 = 0.1176$ with fixed ratio $\frac{a_1}{a_2} = 3.4$.

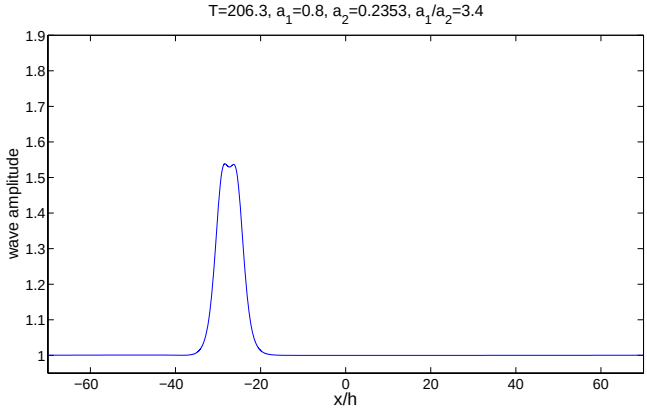

Figure 3.26 Two solitary waves remain separated during the overtaking collision, for $F = 0$, $a_1 = 0.8$, and $a_2 = 0.2353$ with fixed ratio $\frac{a_1}{a_2} = 3.4$.

For $F = 0.5$, fixing ratio $\frac{a_1}{a_2} = 3.2$ for upstream-propagating solitary waves with different wave amplitudes a_1 and a_2, when $a_1 = 0.4$ and $a_2 = 0.125$, two solitary waves merge into a single wave with flat peak, when $a_1 = 0.8$ and $a_2 = 0.25$, two

wave peaks remain separated as shown in Figure 3.28. After comparing Figure 3.25 with Figure 3.27, we know that the critical number also depends the Froude number.

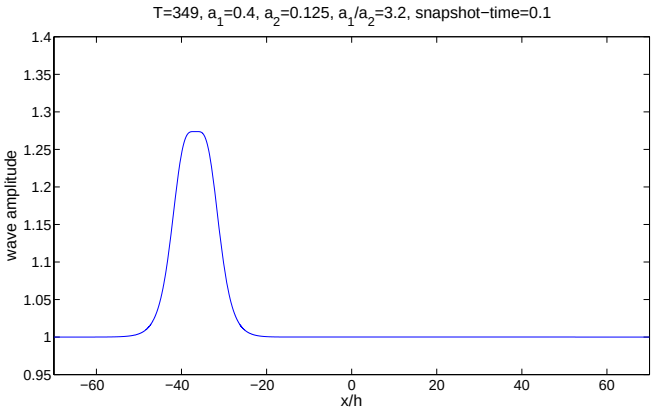

Figure 3.27 Two upstream-propagating solitary waves merge into a single wave with flat peak during the overtaking collision at time $T = 349$. Where $F = 0.5$, $a_1 = 0.4$, and $a_2 = 0.125$ with fixed ratio $\frac{a_1}{a_2} = 3.2$.

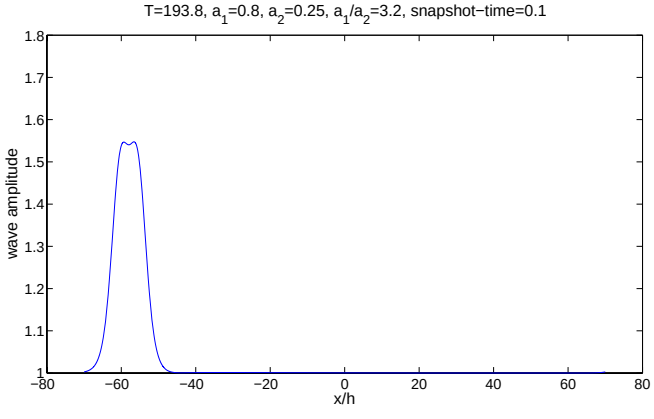

Figure 3.28 Two upstream-propagating solitary waves remain separated during the overtaking collision. Where $F = 0.5$, $a_1 = 0.4$, and $a_2 = 0.125$ with fixed ratio $\frac{a_1}{a_2} = 3.2$.

For $F = 0.5$, fixing ratio $\frac{a_1}{a_2} = 3.55$ for downstream-propagating solitary waves with wave amplitudes $a_1 = 0.4$ and $a_2 = 0.1127$, two solitary waves merge into a single wave with flat peak as shown in Figure 3.29. After comparing Figure 3.27 with

Figure 3.29, we know that the critical number depends on the direction of the wave propagation as well.

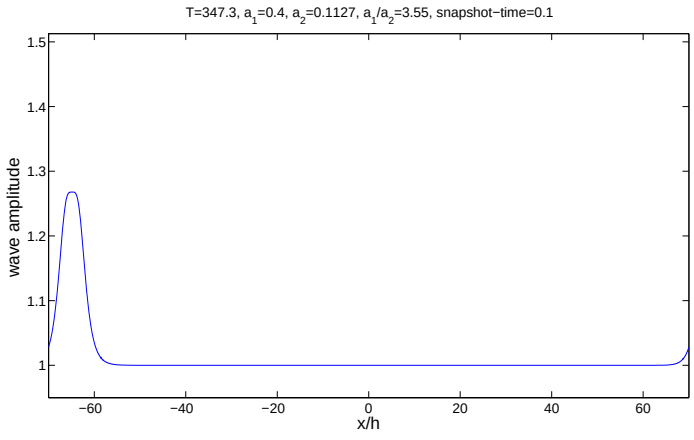

Figure 3.29 Two downstream-propagating solitary waves merge into a single wave with flat peak during the overtaking collision at time $T = 347.3$. Where $F = 0.5$, $a_1 = 0.4$, and $a_2 = 0.1127$ with fixed ratio $\frac{a_1}{a_2} = 3.55$.

3.5.3 Disintegration of an Initial Elevation into Solitary Waves

The evolution of a single (Gaussian) elevation of large amplitude without shear ($F = 0$) has been investigated by Li, Hyman and Choi [24]. Here we will study the disintegration of an initial elevation in uniform shear flows ($F \neq 0$) with different initial conditions for the horizontal velocity u at $t = 0$.

For upstream-propagating waves, we choose initial conditions as

$$\eta(x) = 1 + a \exp^{-0.5x^2}, \tag{3.86}$$

$$u(x) = \left(1 - \frac{1}{\eta}\right)\left[c - \frac{F}{2}(1+\eta)\right], \tag{3.87}$$

where a is the wave amplitude. F is the Froude number, and

$$c = \frac{F}{2} - \sqrt{1 + a + \frac{F^2}{12}(a^2 + 4a + 3)},$$

is the wave speed. The relation between η, u, and the wave speed c for solitary waves given in equation (3.87) is used at $t = 0$.

As shown in Figure 3.30, a single elevation of amplitude $a = 0.5$ quickly breaks into a higher wave traveling to the left and a smaller depression wave traveling to the right. The maximum amplitude of these waves is smaller than the initial wave amplitude because wave propagates in the opposite direction of the shear flow at $t = 0$.

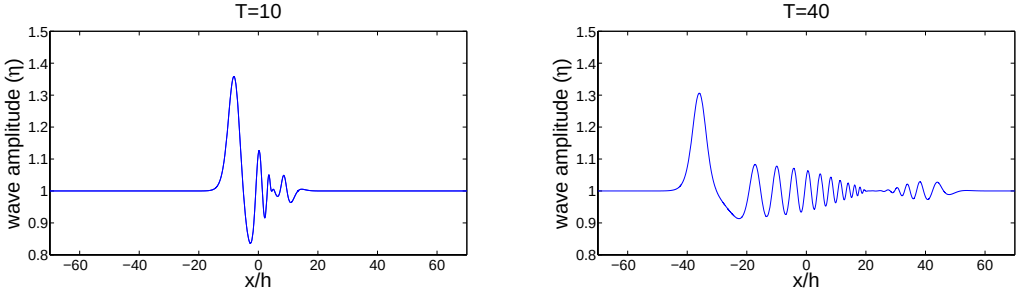

Figure 3.30 Disintegration of a upstream-propagating single elevation of amplitude $a = 0.5$ in the shear flow with $F = 0.5$ at $t = 10$ and $t = 40$. We use the relation between η and u for traveling solitary waves at $t = 0$.

For downstream-propagating waves, we choose initial conditions as

$$\eta(x) = 1 + a\exp^{-0.5x^2}, \tag{3.88}$$

$$u(x) = \left(1 - \frac{1}{\eta}\right)\left[c - \frac{F}{2}(1+\eta)\right], \tag{3.89}$$

where a is the wave amplitude. F is the Froude number, and

$$c = \frac{F}{2} + \sqrt{1 + a + \frac{F^2}{12}(a^2 + 4a + 3)},$$

is the wave speed. The relation between η, u, and the wave speed c for solitary waves given in equation (3.89) is used at $t = 0$.

As shown in Figure 3.31, a single elevation of amplitude $a = 0.5$ quickly breaks into a higher wave traveling to the right and a smaller depression wave traveling to the left. The amplitude of the highest wave is larger than the initial wave amplitude, and the disturbance is smaller comparing with the upstream-propagating wave because wave propagates in the direction of the shear flow at $t = 0$.

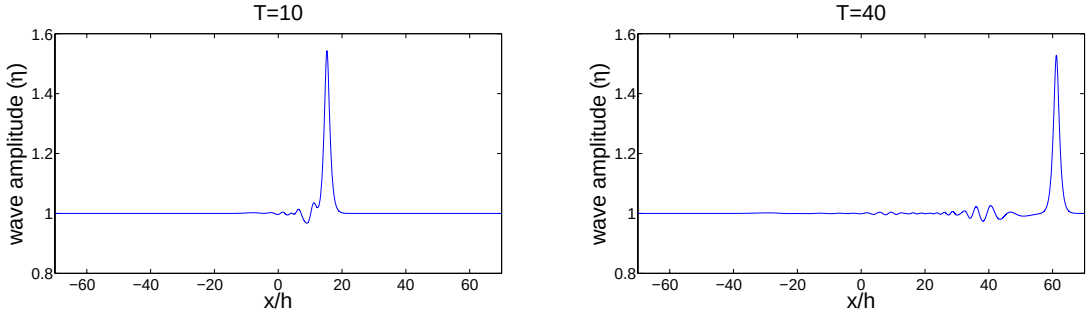

Figure 3.31 Disintegration of a downstream-propagating single elevation of amplitude $a = 0.5$ in the shear flow with $F = 0.5$ at $t = 10$ and $t = 40$. We use the relation between η and u for traveling solitary waves at $t = 0$.

We also can choose initial conditions as

$$\eta(x) = 1 + a\exp^{-0.5x^2}, \tag{3.90}$$

$$u(x) = 0. \tag{3.91}$$

Notice that $u = 0$ at $t = 0$, which means that the initial elevation propagate in both directions at $t = 0$. As shown in Figure 3.32, because of background shear, they are not symmetric with respect to $x = 0$, and the wave traveling to the right is higher than the wave traveling to the left.

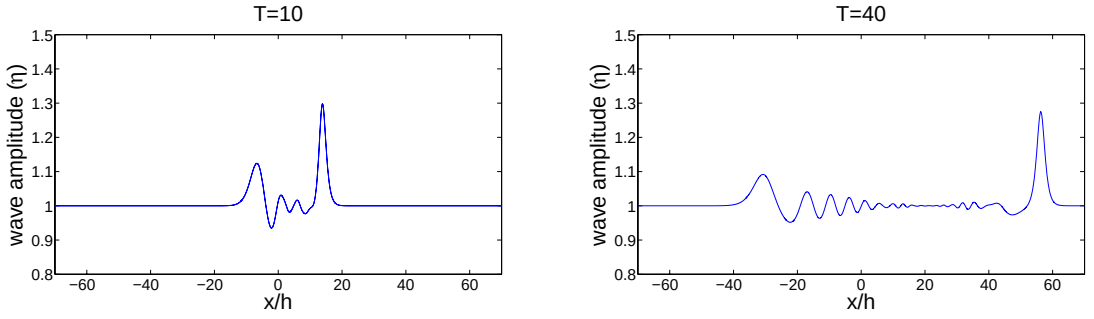

Figure 3.32 Disintegration of a single elevation of amplitude $a = 0.5$ in the shear flow with $F = 0.5$ at $t = 10$ and $t = 40$. At $t = 0$, we set $u = 0$.

3.6 Uniform Shear Flow Interacting with Bottom Topography

It is well-known that a uniform flow in shallow water past over an obstacle with a transcritical velocity can generate a succession of solitary waves propagating ahead of the obstacle and a train of weakly dispersive waves developing behind the obstacle (Wu [36]). When the flow is not critical, in other words, the speed of the oncoming flow (U_0) is not close to the linear long wave speed ($c = \sqrt{gh_0}$) in water of undisturbed depth h_0, linear theory may be used to describe the wave field. However, for the critical flow ($\frac{U_0}{\sqrt{gh_0}}$ is close to unity), linear theory fails, and it is necessary to include nonlinear effects to obtain a physically correct solution. This phenomenon has been studied extensively using the forced Korteweg-de Vries (fKdV) equation and the forced Su-Gardner equations for the weakly nonlinear and strongly nonlinear regimes, respectively.

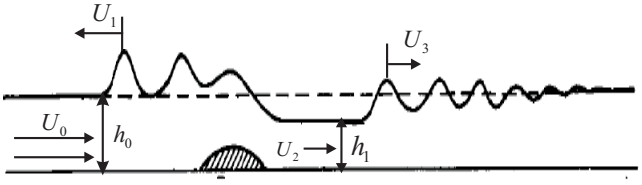

Figure 3.33 A schematic of uniform flow past topography.

As illustrated in Figure 3.33, at criticality ($\frac{U_0}{\sqrt{gh_0}} \approx 1$), it has been shown numeri-cally (Wu [36] based on the fKdV equation, or by El [10] based on the forced Su-Gardner equations) that the flow in the vicinity of a localized obstacle is not steady, but undergoes a time periodic motion, producing solitary waves periodically propagating upstream with velocity U_1 which depends on the wave amplitude. Behind the obstacle, there is a region of depressed water with nearly uniform depth h_1 and fluid velocity U_2 which is in turn followed by a train of waves oscillating about the initial free surface level with the wave height decreasing with distance and with the train length increasing with time.

Here we are interested in investigating this phenomenon in an uniform shear flow past topography, as sketched in Figure 3.34. First we will derive the strongly nonlinear long wave model under the sole assumption that wave length is much longer than the depth of the fluid. This model will reduced to the Su-Gardner equations if the Froude number $F = 0$ and the bottom is flat. After that we will study numerically the model to investigate the interaction of a uniform shear flow with topography. In order to see the effects of background shear, we will compare our numerical solutions for $F \neq 0$ with the results for $F = 0$.

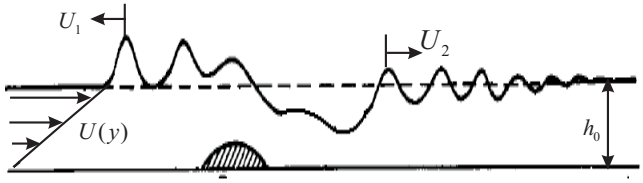

Figure 3.34 A schematic of uniform shear flow past topography.

3.6.1 Derivation of the Governing Equations

For an inviscid and incompressible fluid of density ρ, the two-dimensional velocity components (U, V) in Cartesian coordinates and the pressure P satisfy the Euler equations and the continuity equation given by

$$U_t + UU_x + VU_y = -\frac{P_x}{\rho}, \tag{3.92}$$

$$V_t + UV_x + VV_y = -\frac{P_y}{\rho} - g, \tag{3.93}$$

$$U_x + V_y = 0, \tag{3.94}$$

where g is the gravity acceleration. The boundary conditions at the free surface and the bottom are given by

$$\zeta_t + U\zeta_x = V, \quad \text{at} \quad y = h_0 + \zeta(x, t), \tag{3.95}$$

$$V - Uf_x = 0, \quad \text{at} \quad y = f(x), \tag{3.96}$$

where $\zeta(x,t)$ is the surface elevation. h_0 is the quiescent fluid depth, and $f(x)$ is the localized topographic obstacle.

To derive the model, we first nondimensionalize physical variables as

$$x = Lx^*,\ y = h_0 y^*, t = \frac{L}{\sqrt{gh_0}}t^*,\ P = \rho g h_0 P^*, \tag{3.97}$$

$$U = \sqrt{gh_0}U^*,\ V = \epsilon\sqrt{gh_0}V^*,\ \zeta = h_0\zeta^*,\ f(x) = h_0 f^*(x), \tag{3.98}$$

where L is the typical horizontal length scale and $\epsilon = \frac{h_0}{L}$ is assumed to be small for long waves. When we substitute equations (3.97)–(3.98) into the horizontal momentum equation (3.92) and the continuity equation (3.94), we have, after taking the depth mean of the equations and dropping all the asterisks,

$$\zeta_t + \left(\eta\overline{U}\right)_x = 0, \tag{3.99}$$

$$\left(\eta\overline{U}\right)_t + \left(\eta\overline{U^2}\right)_x = -\eta\overline{P_x}, \tag{3.100}$$

where $\eta = 1 + \zeta(x,t) - f(x)$, $\overline{H}$ is the depth mean quantity defined by

$$\overline{H} = \frac{1}{\eta}\int_{f(x)}^{1+\zeta} H dy.$$

The vertical momentum equation (3.93) can be written as

$$P_y = -1 - \epsilon^2\left(V_t + UV_x + VV_y\right), \tag{3.101}$$

and the vorticity ω is given by

$$\omega = -U_y + \epsilon^2 V_x. \tag{3.102}$$

For uniform shear flows, we decompose the velocity field into

$$U = U_0 + u,\ V = v,\ U_0(y) = Fy, \tag{3.103}$$

where F is the Froude number. $U_0(y)$ is the rotational basic flow and (u, v) are the irrotational perturbation velocity components.

Now we assume that all physical variables for irrotational flows can be expanded as

$$R(x, y, t) = R_0 + \epsilon^2 R_1 + O\left(\epsilon^4\right), \quad R = (u, v, P). \tag{3.104}$$

Substituting equations (3.103)–(3.104) into equations (3.101)–(3.102) with $\omega = -F$, and boundary conditions

$$\zeta_t + U\zeta_x = V, \quad \text{at} \quad y = 1 + \zeta(x), \tag{3.105}$$

$$V - Uf_x = 0, \quad \text{at} \quad y = f(x), \tag{3.106}$$

we obtain the leading-order equations as

$$u_{0y} = 0, \ v_{0y} = -u_{0x}, \ P_{0y} = -1, \tag{3.107}$$

where the continuity equation $u_x + v_y = 0$ has been used. Then the first-order solutions can be found as

$$u_0 = u_0(x, t), \ v_0 = -u_{0x}(y - f) + (Ff + u_0)f_x, \ P_0 = -(y - 1 - \zeta), \tag{3.108}$$

where the boundary conditions, $v_0 = (Ff + u_0)f_x$ at $y = f(x)$ and $P_0 = 0$ at $y = 1 + \zeta$, have been imposed.

Similarly the second-order solutions can be found, at $O(\epsilon^2)$, as

$$u_1(x, y, t) = -\frac{1}{2}u_{0xx}y^2 + (u_{0x}f + u_0 f_x + Fff_x)_x y + g(x, t), \tag{3.109}$$

and from equation (3.101), the second-order pressure P_1 is given by

$$P_1 = \frac{F}{3}u_{0xx}\left[y^3 - (1 + \zeta)^3\right] + \frac{G_0 - FQ_x}{2}\left[y^2 - (1 + \zeta)^2\right] - R(y - 1 - \zeta), \tag{3.110}$$

where

$$G_0 = u_{0xt} + u_0 u_{0xx} - u_{0x}^2,\ Q = u_{0x} f + u_0 f_x + F f f_x,\ R = Q_t + u_0 Q_x - u_{0x} Q.$$

After using the boundary condition $P_1 = 0$ on $y = 1 + \zeta$, we have

$$\begin{aligned}\overline{P_x} &= \zeta_x - \frac{1}{\eta}\left[\frac{3\eta^4 + 8\eta^3 f + 6\eta^2 f^2}{12} F u_{0xx} + \frac{2\eta^3 + 3\eta^2 f}{6}\left(G_0 - F Q_x\right) - \frac{\eta^2}{2} R\right]_x \\ &\quad - f_x\left[\frac{\eta^3 + 3\eta^2 f + 3\eta f^2}{3} F u_{0xx} + \frac{\eta^2 + 2\eta f}{2}\left(G_0 - F Q_x\right) - R\eta\right] + O\left(\epsilon^4\right).\end{aligned}$$

Also, we have

$$\eta\overline{U} = \frac{\eta^2 + 2\eta f}{2} F + \eta\overline{u}, \tag{3.111}$$

$$\eta\overline{U^2} = \frac{\eta^3 + 3\eta^2 f + 3\eta f^2}{3} F^2 + 2F\int_{f(x)}^{1+\zeta} y u dy + \eta\overline{u^2}, \tag{3.112}$$

$$\eta\overline{U}^2 = \frac{\eta\left(\eta^2 + 4\eta f + 4f^2\right)}{4} F^2 + F\left(\eta + 2f\right)\eta\overline{u} + \eta\overline{u^2}, \tag{3.113}$$

$$2F\int_{f(x)}^{1+\zeta} y u dy = F\left(\eta + 2f\right)\eta\overline{u} - F\left(\frac{\eta^4 + 2\eta^3 f}{12}\overline{u_{xx}} - \frac{\eta^3 Q}{6}\right), \tag{3.114}$$

$$\eta\overline{u^2} = \eta\overline{u}^2 + O\left(\epsilon^4\right),\quad u_0 = \overline{u} + O\left(\epsilon^2\right). \tag{3.115}$$

By substituting equations (3.111)–(3.115) into equations (3.99)–(3.100), after dropping bar, we obtain the following evolution equations for η and u:

$$\begin{aligned}\eta_t + \left[\frac{F}{2}\left(\eta^2 + 2\eta f\right) + \eta u\right]_x &= 0, \\ u_t + u u_x + \zeta_x &= \frac{1}{\eta}\left[\frac{\eta^3}{3} G - \frac{\eta^2}{2} D\left(u f_x\right) + F A - F^2\frac{\eta^2\left(\eta + f\right)\left(f f_x\right)_x}{2}\right]_x \\ &\quad + f_x\left[\frac{\eta}{2} G - D(u f_x) + F B - F^2\frac{\left(\eta + 2f\right)\left(f f_x\right)_x}{2}\right] - F(f u + \frac{F}{2} f^2)_x,\end{aligned}$$

where

$$\begin{aligned}&G = u_{xt} + u u_{xx} - u_x^2,\quad D = \partial_t + u\partial_x, \\ &A = \frac{\left(\eta + f\right)\eta^3 u_{xx}}{3} - \frac{\eta^2\left(\eta + f\right)\left(u f_{xx} + 2 f_x u_x\right)}{2} - \frac{\eta^2\left[u\left(f f_x\right)_x - f f_x u_x\right]}{2}, \\ &B = \frac{2\eta^2 + 3\eta f}{6} u_{xx} - \frac{\left(\eta + 2f\right)\left(2 f_x u_x + u f_{xx}\right)}{2}.\end{aligned}$$

3.6.2 Numerical Simulations

The numerical scheme is developed by using a 4th-order finite difference method in space x and a 4th-order Admas-Bashforth method in time t. Therefore, the error is $O(\triangle x^4, \triangle t^4)$, where $\triangle x$ is the grid size and $\triangle t$ is the time step. For numerical simulations, we use function $f(x) = f_m \exp^{\left(-x^2/w^2\right)}$ for bottom topography, where f_m is the maximum height of the topography and w is a constant.

The general features of our numerical results with narrow localized topography can been seen from the following typical examples for

$$f_m = 0.2,\ w = 2.0,\ u(x,0) = 1.0,\ F = 0.5, \tag{3.116}$$

$$f_m = -0.2,\ w = 2.0,\ u(x,0) = 1.0,\ F = 0.5, \tag{3.117}$$

where F is the Froude number. $u(x,0)$ is the velocity of the irrotational part of the uniform shear flow at $t = 0$. A positive f_m means the surface of the topography is convex, as shown in Figure 3.34 and negative represents the opposite.

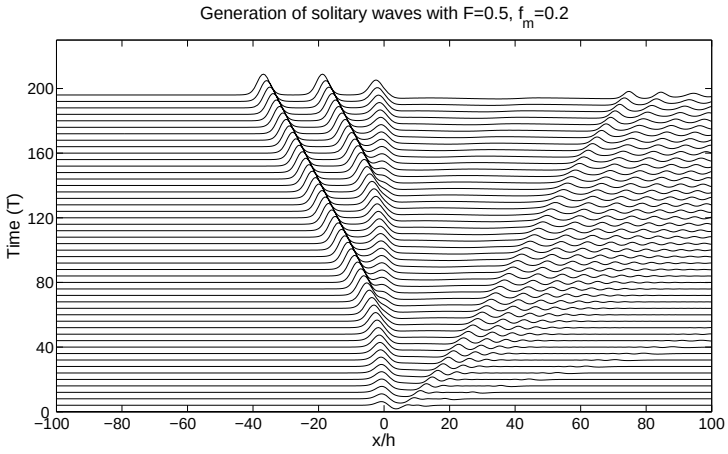

Figure 3.35 Uniform shear flow interacts with non-uniform convex topography between $T = 0$ and $T = 200$. Where $f_m = 0.2,\ w = 2.0,\ u(x,0) = 1.0$, and $F = 0.5$.

For the case of the positive forcing ($f_m > 0$), as shown in Figure 3.35, a conspicuous feature of the numerical result is that a solitary wave emerges in the

left side of the topography, and eventually breaks away to propagate upstream as a free solitary wave. This is followed by another new solitary wave emerging through the same cycle and this process seems to continue periodically. Behind the topography, there is a region of depressed water with small oscillation, which is in turn followed by a train of conoidal-like waves about the initial free surface level, with the wave height decreasing with distance and with the train length increasing with time. Numerical results of the uniform flow ($F = 0$) past the topography with the same parameter values are shown in Figure 3.36. After comparing with Figure 3.35, we can see that the amplitude of the solitary wave upstream-propagating in the uniform shear flow is close to 1.07 which is larger than that of the solitary wave generated in uniform flow which is close to 0.717. The period of upstream-propagating solitary waves in uniform shear flow is also much longer than that in uniform flow. The length of the region of depressed water behind the topography in the uniform shear flow is much longer than that in the uniform flow as well, and the depth is no longer uniform. However, in the uniform shear flow, the maximum amplitude of the train waves following the depressed water region is smaller than that in the uniform flow.

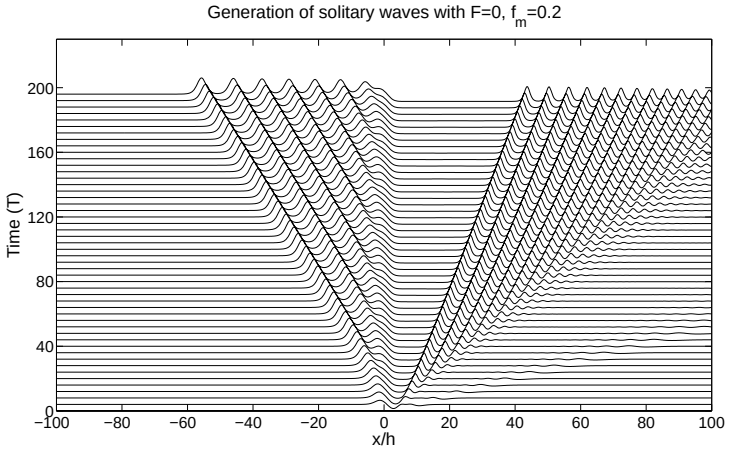

Figure 3.36 Uniform flow interacts with non-uniform convex topography between $T = 0$ and $T = 200$. Where $f_m = 0.2,\ w = 2.0,\ u(x, 0) = 1.0$, and $F = 0$.

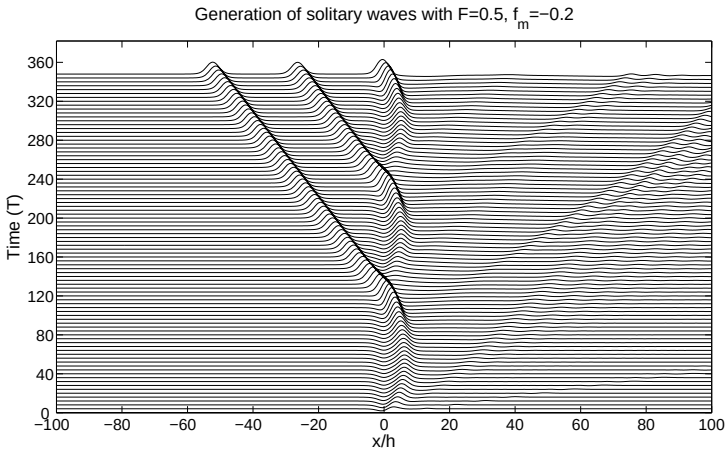

Figure 3.37 Uniform shear flow interacts with non-uniform concave topography between $T = 0$ and $T = 350$. Where $f_m = -0.2,\ w = 2.0,\ u(x, 0) = 1.0$, and $F = 0.5$.

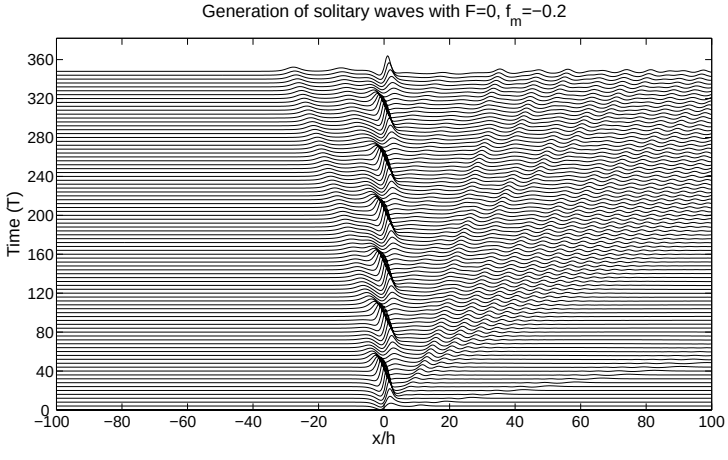

Figure 3.38 Uniform flow interacts with non-uniform concave topography between $T = 0$ and $T = 350$. Where $f_m = -0.2,\ w = 2.0,\ u(x, 0) = 1.0$, and $F = 0$.

When the surface of the topography is concave ($f_m < 0$), the numerical result in the uniform shear flow is shown in Figure 3.37, we can see that the local wave is continuous to be excited with a relatively large amplitude within the region of the topography before it breaks away, and soon it will settle to a upstream-propagating solitary wave with a smaller amplitude. This procedure will generate a succession

of solitary waves with very close amplitude. Behind the topography, the depressed water region is not uniform in depth, which is in turn followed by a train of waves oscillating about the initial free surface level. After comparing the numerical result of the uniform flow, as shown in Figure 3.38, we can see that, due to the shear effect, the amplitude of the excited wave and the generated solitary wave are larger in a uniform shear flow than those in a uniform flow. Since the excess mass of the upstream-propagating solitary wave comes from the region of surface depression, this is consistent with the numerical result that the length of the region of depressed water is larger in the uniform shear flow case.

CHAPTER 4

TRANSVERSE INSTABILITY OF SOLITARY WAVES

Here we will study transverse stability (or instability) of large amplitude solitary waves subject to transverse perturbations whose wavelength is much greater than the characteristic length scale in the wave propagation direction. One-dimensional stability of the solitary wave solutions of the Su-Gardner equations was examined analytically by Li [23] using the Evans function method and it was found that solitary waves of small amplitude are neutrally stable. Nevertheless, no conclusion on large amplitude solitary waves was made.

Consider an irrotational flow in an inviscid and incompressible ideal fluid of uniform depth h under the action of uniform gravitational acceleration g. Under the assumption that the ratio between fluid depth h and wavelength L is small, the dimensionless Green-Naghdi equations [15] in two horizontal dimensions can be derived from the Euler equations as

$$\frac{\partial \eta}{\partial t} + \frac{\partial \eta u}{\partial x} + \frac{\partial \eta v}{\partial y} = 0 \,, \tag{4.1}$$

$$\frac{\partial u}{\partial t} + u\frac{\partial u}{\partial x} + v\frac{\partial u}{\partial y} + \frac{\partial \eta}{\partial x} = \frac{1}{\eta}\frac{\partial}{\partial x}\left(\frac{\eta^3}{3}G\right) \,, \tag{4.2}$$

$$\frac{\partial v}{\partial t} + u\frac{\partial v}{\partial x} + v\frac{\partial v}{\partial y} + \frac{\partial \eta}{\partial y} = \frac{1}{\eta}\frac{\partial}{\partial y}\left(\frac{\eta^3}{3}G\right) \,, \tag{4.3}$$

where u and v are the horizontal velocities in the x and y directions, η is the wave elevation, and G is defined as

$$G\left(x,y,t\right) = \boldsymbol{\nabla}\cdot\boldsymbol{u_t} + \boldsymbol{u}\cdot\boldsymbol{\nabla}\left(\boldsymbol{\nabla}\cdot\boldsymbol{u}\right) - \left(\boldsymbol{\nabla}\cdot\boldsymbol{u}\right)^2 .$$

We seek a solitary wave solution of equations (4.1)–(4.3) in the following form

$$u = -c + u_s(x), \quad \eta = \eta_s(x), \quad v = 0, \tag{4.4}$$

where u_s and η_s tend to zero as $x \to \pm\infty$ and c is a positive wave speed. Then, $\eta_s(x)$ and $u_s(x)$ satisfy the following equations:

$$\frac{\partial}{\partial x}\left[(-c + u_s)\,\eta_s\right] = 0\ , \tag{4.5}$$

$$(-c + u_s)\,\frac{\partial u_s}{\partial x} + \frac{\partial \eta_s}{\partial x} = \frac{1}{\eta_s}\frac{\partial}{\partial x}\left[\frac{\eta_s^3}{3}\left((-c + u_s)\,\frac{\partial^2 u_s}{\partial x^2} - \left(\frac{\partial u_s}{\partial x}\right)^2\right)\right]. \tag{4.6}$$

Now we carry out linear stability analysis of the solitary wave solution given by equation (4.4). First we assume the solutions of equations (4.1)–(4.3) can be written as

$$\eta(x, y, t) = \eta_s(x) + \hat{\eta}(x)\exp^{\lambda t + i\epsilon y}\ , \tag{4.7}$$

$$u(x, y, t) = -c + u_s(x) + \hat{u}(x)\exp^{\lambda t + i\epsilon y}\ , \tag{4.8}$$

$$v(x, y, t) = \hat{v}(x)\exp^{\lambda t + i\epsilon y}\ , \tag{4.9}$$

where ϵ is the wave number in the y direction and λ is a complex constant which will be determined by solving a set of equations for $\hat{u},\ \hat{v}$, and $\hat{\eta}$ derived from equations (4.1)–(4.3). The steady solutions given by (4.4) are unstable if λ has a positive real part; otherwise they are stable. By Substituting equations (4.7)–(4.9) into equations (4.1)–(4.3), linearizing with respect to $(\hat{u},\ \hat{v},\ \hat{\eta})$, and imposing the zero boundary conditions as $x \to \pm\infty$, we obtain the following set of linear equations for $\hat{u},\ \hat{v}$, and $\hat{\eta}$:

$$L_1\left[\hat{u},\ \hat{\eta}\right] = -i\epsilon\eta_s\hat{v} - \lambda\hat{\eta}, \tag{4.10}$$

$$\begin{aligned} L_2\left[\hat{u},\ \hat{\eta}\right] = {} & \frac{i\epsilon}{3\eta_s}\frac{\partial}{\partial x}\left\{\eta_s^3\left[(-c + u_s)\,\frac{\partial \hat{v}}{\partial x} - 2\frac{\partial u_s}{\partial x}\hat{v}\right]\right\} \\ & -\lambda\left\{\hat{u} - \frac{1}{3\eta_s}\frac{\partial}{\partial x}\left[\eta_s^3\left(\frac{\partial \hat{u}}{\partial x} + i\epsilon\hat{v}\right)\right]\right\}, \end{aligned} \tag{4.11}$$

$$(-c+u_s)\frac{\partial \hat{v}}{\partial x} = \epsilon L_3[\hat{u},\ \hat{\eta}] - \epsilon^2 \frac{\eta_s^2}{3}\left[(-c+u_s)\frac{\partial \hat{v}}{\partial x} - 2\frac{\partial u_s}{\partial x}\hat{v}\right] + \lambda\left[i\epsilon\frac{\eta_s^2}{3}\frac{\partial \hat{u}}{\partial x} - \left(1+\epsilon^2\right)\hat{v}\right], \tag{4.12}$$

where the linear operators $L_1,\ L_2$, and Ł$_3$ are defined as

$$L_1[\hat{u},\hat{\eta}] = \frac{\partial}{\partial x}\left(\eta_s \hat{u}\right) + \frac{\partial}{\partial x}\left[(-c+u_s)\,\hat{\eta}\right], \tag{4.13}$$

$$\begin{aligned} L_2[\hat{u},\hat{\eta}] = &-\frac{1}{3\eta_s}\frac{\partial}{\partial x}\left\{\eta_s^3\left[(-c+u_s)\frac{\partial^2 \hat{u}}{\partial x^2} + \hat{u}\frac{\partial^2 u_s}{\partial x^2} - 2\frac{\partial u_s}{\partial x}\frac{\partial \hat{u}}{\partial x}\right]\right\} \\ &+\frac{\partial}{\partial x}\left[(-c+u_s)\,\hat{u}\right] + \frac{1}{3}\eta_s\hat{\eta}\left[(-c+u_s)\frac{\partial^3 u_s}{\partial x^3} - \frac{\partial u_s}{\partial x}\frac{\partial^2 u_s}{\partial x^2}\right] \\ &+\frac{\partial \hat{\eta}}{\partial x} - \frac{\partial}{\partial x}\left\{(\eta_s\hat{\eta})\left[(-c+u_s)\frac{\partial^2 u_s}{\partial x^2} - \left(\frac{\partial u_s}{\partial x}\right)^2\right]\right\}, \end{aligned} \tag{4.14}$$

$$\begin{aligned} L_3[\hat{u},\ \hat{\eta}] = &\ i\frac{\eta_s^2}{3}\left[(-c+u_s)\frac{\partial^2 \hat{u}}{\partial x^2} + \frac{\partial^2 u_s}{\partial x^2}\hat{u} - 2\frac{\partial u_s}{\partial x}\frac{\partial \hat{u}}{\partial x}\right] \\ &+i\left\{\eta_s\left[(-c+u_s)\frac{\partial^2 u_s}{\partial x^2} - \left(\frac{\partial u_s}{\partial x}\right)^2\right] - 1\right\}\hat{\eta}. \end{aligned} \tag{4.15}$$

The boundary conditions to be imposed are given by

$$\hat{u}\,(x) \to 0,\ \hat{v}\,(x) \to 0,\ \hat{\eta}\,(x) \to 0 \ \text{ as } \ x \to \pm\infty. \tag{4.16}$$

When there are no perturbations in the y direction (i.e., $\epsilon = 0$ and $\hat{v} = 0$), equations (4.10)–(4.12) can be reduced to

$$L_1[\hat{u},\hat{\eta}] = -\lambda\hat{\eta}, \tag{4.17}$$

$$L_2[\hat{u},\hat{\eta}] = -\lambda\left(\hat{u} - \eta_s\frac{\partial \eta_s}{\partial x}\frac{\partial \hat{u}}{\partial x} - \frac{\eta_s^2}{3}\frac{\partial^2 \hat{u}}{\partial x^2}\right). \tag{4.18}$$

This is an eigenvalue problem for $\hat{u}$ and $\hat{\eta}$. Notice that $\lambda = 0$ is always an eigenvalue of equations (4.17)–(4.18) and is in fact the only eigenvalue of equations (4.17)–(4.18) when the speed of a solitary wave is close to the linear wave speed [23].

In order to study stability of the solitary wave solution given by (4.4) subject to long wavelength transverse perturbations, we assume that ϵ is small and expand

$\lambda,\ \hat{\eta},\ \hat{u}$, and $\hat{v}$ as

$$\hat{u}(x) = \hat{u}_0(x) + \epsilon\hat{u}_1(x) + \epsilon^2\hat{u}_2(x) + \epsilon^3\hat{u}_3(x) + \cdots\cdots\ , \tag{4.19}$$

$$\hat{\eta}(x) = \hat{\eta}_0(x) + \epsilon\hat{\eta}_1(x) + \epsilon^2\hat{\eta}_2(x) + \epsilon^3\hat{\eta}_3(x) + \cdots\cdots\ , \tag{4.20}$$

$$\hat{v}(x) = \hat{v}_0(x) + \epsilon\hat{v}_1(x) + \epsilon^2\hat{v}_2(x) + \epsilon^3\hat{v}_3(x) + \cdots\cdots\ , \tag{4.21}$$

$$\lambda = \epsilon\lambda_1 + \epsilon^2\lambda_2 + \epsilon^3\lambda_3 + \cdots\cdots\ . \tag{4.22}$$

Substituting the expansions of $\lambda,\ \hat{\eta},\ \hat{u}$, and $\hat{v}$ into equations (4.10)–(4.12) and collecting the same order terms in ϵ, we have

$$L_1[\hat{u}_n, \hat{\eta}_n] = F_n, \tag{4.23}$$

$$L_2[\hat{u}_n, \hat{\eta}_n] = G_n, \tag{4.24}$$

$$(-c + u_s)\frac{\partial \hat{v}_n}{\partial x} = L_3[\hat{u}_{n-1}, \hat{\eta}_{n-1}] + H_n, \tag{4.25}$$

where $L_1,\ L_2$, and L_3 are defined in equations (4.13)–(4.15) and

$$F_n = -\lambda_j\hat{\eta}_{n-j} - i\eta_s\hat{v}_{n-1}, \tag{4.26}$$

$$\begin{aligned} G_n = &-\lambda_j\left[\hat{u}_{n-j} - \frac{1}{3\eta_s}\frac{\partial}{\partial x}\left(\eta_s^3\frac{\partial \hat{u}_{n-j}}{\partial x} + i\hat{v}_{n-1-j}\right)\right] \\ &+\frac{i}{3\eta_s}\frac{\partial}{\partial x}\left\{\eta_s^3\left[(-c + u_s)\frac{\partial \hat{v}_{n-1}}{\partial x} - 2\frac{\partial u_s}{\partial x}\hat{v}_{n-1}\right]\right\}, \end{aligned} \tag{4.27}$$

$$\begin{aligned} H_n = &\lambda_j\left(\frac{i\eta_s^2}{3}\frac{\partial \hat{u}_{n-1-j}}{\partial x} - \hat{v}_{n-j} - \hat{v}_{n-2-j}\right) \\ &-\frac{\eta_s^2}{3}\left[(-c + u_s)\frac{\partial \hat{v}_{n-2}}{\partial x} - 2\frac{\partial u_s}{\partial x}\hat{v}_{n-2}\right]. \end{aligned} \tag{4.28}$$

We remark that $\hat{u}_{-j} = 0$, $\hat{v}_{-j} = 0$, and $\hat{\eta}_{-j} = 0$, $j = 1,\ 2,\ \cdots$, $n = 0,\ 1,\ 2,\ \cdots$.

After solving following equation

$$\int_{-\infty}^{\infty}\left(\eta^* L_1[\eta, u] + u^* L_2[\eta, u]\right)\ dx = \int_{-\infty}^{\infty}\left(\eta L_1^*[\eta^*, u^*] + u^* L_2^*[\eta^*, u^*]\right)\ dx,$$

we obtain the adjoint equations of the homogeneous parts of equations (4.23)–(4.24), given by

$$L_1^*[u^*,\ \eta^*] = 0, \qquad L_2^*[u^*,\ \eta^*] = 0, \tag{4.29}$$

where L_1^* and L_2^* are the adjoint operators of L_1 and L_2 and are defined by

$$\begin{aligned} L_1^*[u^*,\ \eta^*] = &-\frac{\partial u^*}{\partial x} + \eta_s \frac{\partial}{\partial x}\left\{\left[(-c+u_s)\frac{\partial^2 u_s}{\partial x^2} - \left(\frac{\partial u_s}{\partial x}\right)^2\right]u^*\right\} \\ &- (-c+u_s)\frac{\partial \eta^*}{\partial x} - \frac{2\eta_s}{3}\left[(-c+u_s)\frac{\partial^3 u_s}{\partial x^3} - \frac{\partial u_s}{\partial x}\frac{\partial^2 u_s}{\partial x^2}\right]u^*, \end{aligned} \tag{4.30}$$

$$\begin{aligned} L_2^*[u^*,\ \eta^*] = &-\eta_s\frac{\partial \eta^*}{\partial x} - (-c+u_s)\frac{\partial u^*}{\partial x} \\ &-\frac{u^*}{3\eta_s}\frac{\partial}{\partial x}\left(\eta_s^3\frac{\partial^2 u_s}{\partial x^2}\right) - \frac{\partial}{\partial x}\left[2\eta_s\frac{\partial \eta_s}{\partial x}\frac{\partial u_s}{\partial x}u^* + \frac{\eta_s^2}{3}\frac{\partial^2 u_s}{\partial x^2}u^*\right] \\ &+\frac{\partial^3}{\partial x^3}\left[\frac{\eta_s^2}{3}(-c+u_s)u^*\right] - \frac{\partial^2}{\partial x^2}\left[\eta_s\frac{\partial \eta_s}{\partial x}(-c+u_s)u^* - \frac{\eta_s^2}{3}\frac{\partial u_s}{\partial x}u^*\right]. \end{aligned} \tag{4.31}$$

From equations (4.5)–(4.6), we know $u^* = \eta_s$ and $\eta^* = u_s$ are the solutions of the adjoint equations. Therefore, for the inhomogeneous equations given by (4.23)–(4.24) to have solutions, their inhomogeneous terms on the right-hand sides should satisfy the following solvability condition:

$$\int_{-\infty}^{\infty}(u_s F_n + \eta_s G_n)dx = 0. \tag{4.32}$$

For $n = 0$, we have

$$L_1[\hat{u}_0, \hat{\eta}_0] = 0, \tag{4.33}$$

$$L_2[\hat{u}_0, \hat{\eta}_0] = 0, \tag{4.34}$$

$$(-c+u_s)\frac{\partial \hat{v}_0}{\partial x} = 0. \tag{4.35}$$

The nontrivial solutions of the homogeneous equations (4.33)–(4.35) satisfying the boundary conditions given by equation (4.16) as $x \to \pm\infty$ can be found as

$$\hat{u}_0 = \frac{\partial u_s}{\partial x},\ \hat{\eta}_0 = \frac{\partial \eta_s}{\partial x},\ \text{and } \hat{v}_0 = 0.$$

For $n = 1$, we have

$$L_1[\hat{u}_1, \hat{\eta}_1] = -\lambda_1 \hat{\eta}_0, \tag{4.36}$$

$$L_2[\hat{u}_1, \hat{\eta}_1] = -\lambda_1 (\hat{u}_0 - \eta_s \frac{\partial \eta_s}{\partial x} \frac{\partial \hat{u}_0}{\partial x} - \frac{\eta_s^2}{3} \frac{\partial^2 \hat{u}_0}{\partial x^2}), \tag{4.37}$$

$$(-c + u_s) \frac{\partial \hat{v}_1}{\partial x} = i(-c + u_s) \frac{\partial u_s}{\partial x}. \tag{4.38}$$

The solvability condition given by equation (4.32) is satisfied automatically, i.e.,

$$-\lambda_1 \int_{-\infty}^{\infty} \left[\frac{\partial}{\partial x} (\eta_s u_s) - \frac{1}{3} \frac{\partial}{\partial x} \left(\eta_s^3 \frac{\partial^2 u_s}{\partial x^2} \right) \right] dx = 0, \tag{4.39}$$

and, therefore, λ_1 cannot be determined at this order. Then, the general solutions of equations (4.36)–(4.38) satisfying the boundary conditions given by equation (4.16) $x \to \pm\infty$ are

$$\hat{u}_1 = r_1 \frac{\partial u_s}{\partial x} - \lambda_1 \frac{\partial u_s}{\partial c}, \ \hat{\eta}_1 = r_1 \frac{\partial \eta_s}{\partial x} - \lambda_1 \frac{\partial \eta_s}{\partial c}, \text{ and } \hat{v}_1 = i u_s,$$

where r_1 is an arbitrary constant, $\frac{\partial u_s}{\partial c}$ and $\frac{\partial \eta_s}{\partial c}$ represent the derivatives of u_s and η_s with respect to c for fixed x,

For $n = 2$, we have

$$L_1[\hat{u}_2, \hat{\eta}_2] = -\lambda_2 \hat{\eta}_0 - \lambda_1 \hat{\eta}_1 + \eta_s u_s, \tag{4.40}$$

$$\begin{aligned} L_2[\hat{u}_2, \hat{\eta}_2] &= -\lambda_2 \left[\hat{u}_0 - \frac{1}{3\eta_s} \frac{\partial}{\partial x} \left(\eta_s^3 \frac{\partial \hat{u}_0}{\partial x} \right) \right] - \lambda_1 \hat{u}_1 \\ &\quad + \frac{\lambda_1}{3\eta_s} \frac{\partial}{\partial x} \left(\eta_s^3 \frac{\partial \hat{u}_1}{\partial x} \right) - \frac{1}{3\eta_s} \frac{\partial}{\partial x} \left\{ \eta_s^3 \left[(-c - u_s) \frac{\partial u_s}{\partial x} \right] \right\}, \end{aligned} \tag{4.41}$$

$$\begin{aligned} (-c + u_s) \frac{\partial \hat{v}_2}{\partial x} &= i \frac{\eta_s^2}{3} \left[(-c + u_s) \frac{\partial^2 \hat{u}_1}{\partial x^2} + \frac{\partial^2 u_s}{\partial x^2} \hat{u}_1 - 2 \frac{\partial u_s}{\partial x} \frac{\partial \hat{u}_1}{\partial x} \right] - \lambda_1 \hat{v}_1 \\ &\quad + i\lambda_1 \frac{\eta_s^2}{3} \frac{\partial \hat{u}_0}{\partial x} + i \left\{ \eta_s \left[(-c + u_s) \frac{\partial^2 u_s}{\partial x^2} - \left(\frac{\partial u_s}{\partial x} \right)^2 \right] - 1 \right\} \hat{\eta}_1. \end{aligned} \tag{4.42}$$

The solvability condition given in equation (4.32) is

$$-\lambda_1^2 \int_{-\infty}^{\infty} \frac{\partial}{\partial c} (\eta_s u_s) dx = \int_{-\infty}^{\infty} \eta_s u_s^2 dx, \tag{4.43}$$

which determines λ_1. From the fact that the steady solution u_s and η_s satisfy equations (4.5)–(4.6), we can see that $\eta_s u_s^2 > 0$, $\frac{\partial}{\partial c}(\eta_s u_s) > 0$, and

$$\lambda_1 = \pm i \sqrt{\frac{\int_{-\infty}^{\infty} \eta_s u_s^2 dx}{\int_{-\infty}^{\infty} \frac{\partial}{\partial c}(\eta_s u_s)\, dx}}. \tag{4.44}$$

The real part of λ_1 is zero so that the stability of the solitary wave solutions is not determined at this order; therefore, we have to proceed to the next order.

For $n = 3$, the solvability condition given by equation (4.32) is

$$\lambda_1 \lambda_2 \int_{-\infty}^{\infty} \frac{\partial}{\partial c}(\eta_s u_s) dx - \lambda_1 \int_{-\infty}^{\infty} (u_s \hat{\eta}_2 + \eta_s \hat{u}_2) dx = \int_{-\infty}^{\infty} i \eta_s u_s \hat{v}_2 dx. \tag{4.45}$$

To evaluate λ_2, notice that we have to find solutions of equations (4.40)–(4.42) for $\hat{u}_2$, $\hat{\eta}_2$, and $\hat{v}_2$. Since L_1, L_2 are linear operates, we can decompose $\hat{u}_2$ and $\hat{\eta}_2$ into three parts

$$\hat{u}_2 = (-\lambda_2 - \lambda_1 r_1)\hat{u}_{20} + \lambda_1^2 \hat{u}_{21} + \hat{u}_{22}, \quad \hat{\eta}_2 = (-\lambda_2 - \lambda_1 r_1)\hat{\eta}_{20} + \lambda_1^2 \hat{\eta}_{21} + \hat{\eta}_{22}, \tag{4.46}$$

where $\hat{u}_{20}$, $\hat{\eta}_{20}$, $\hat{u}_{21}, \hat{\eta}_{21}$, $\hat{u}_{22}$, and $\hat{\eta}_{22}$ satisfy the following equations

$$L_1[\hat{u}_{20}, \hat{\eta}_{20}] = \hat{\eta}_0, \tag{4.47}$$

$$L_2[\hat{u}_{20}, \hat{\eta}_{20}] = \hat{u}_0 - \frac{1}{3\eta_s} \frac{\partial}{\partial x} \left(\eta_s^3 \frac{\partial \hat{u}_0}{\partial x} \right), \tag{4.48}$$

$$L_1[\hat{u}_{21}, \hat{\eta}_{21}] = \frac{\partial u_s}{\partial c}, \tag{4.49}$$

$$L_2[\hat{u}_{21}, \hat{\eta}_{21}] = \frac{\partial u_s}{\partial c} - \frac{1}{3\eta_s} \frac{\partial}{\partial x} \left[\eta_s^3 \frac{\partial}{\partial x} \left(\frac{\partial u_s}{\partial c} \right) \right], \tag{4.50}$$

$$L_1[\hat{u}_{22}, \hat{\eta}_{22}] = \eta_s u_s, \tag{4.51}$$

$$L_2[\hat{u}_{22}, \hat{\eta}_{22}] = -\frac{1}{3\eta_s} \frac{\partial}{\partial x} \left\{ \eta_s^3 \left[(-c + u_s) \frac{\partial u_s}{\partial x} \right] \right\}. \tag{4.52}$$

From equations (4.47)–(4.48), we can find $\hat{u}_{20}$ and $\hat{\eta}_{20}$ as

$$\hat{u}_{20} = \frac{\partial u_s}{\partial c} + r_2 \frac{\partial u_s}{\partial x}, \ \hat{\eta}_{20} = \frac{\partial \eta_s}{\partial c} + r_2 \frac{\partial \eta_s}{\partial x},$$

where r_2 is an arbitrary constant.

Substituting equation (4.46) into equation (4.45) and using the fact $\int_{-\infty}^{\infty} \frac{\partial}{\partial x}(u_s\eta_s) = 0$, the solvability condition can be rewritten as

$$i\int_{-\infty}^{\infty}(\eta_s u_s \hat{v}_2)dx = \left(2\lambda_1\lambda_2 + r_1\lambda_1^2\right)\frac{\partial}{\partial c}\int_{-\infty}^{\infty}(\eta_s u_s)dx \\ -\lambda_1^3\int_{-\infty}^{\infty}(\hat{\eta}_{21}u_s + \hat{u}_{21}\eta_s)dx - \lambda_1\int_{-\infty}^{\infty}(\hat{\eta}_{22}u_s + \hat{u}_{22}\eta_s)dx. \quad (4.53)$$

Since u_s, η_s, $\frac{\partial u_s}{\partial c}$, and $\frac{\partial \eta_s}{\partial c}$ are even functions with respect to x, the right-hand sides of equations (4.49)–(4.50) are even functions. Then, by replacing x by $-x$ in equations (4.49)–(4.50), it can be noticed that

$$L_1[\hat{u}_{21}(x), \hat{\eta}_{21}(x)] = -L_1[\hat{u}_{21}(-x), \hat{\eta}_{21}(-x)], \quad (4.54)$$

$$L_2[\hat{u}_{21}(x), \hat{\eta}_{21}(x)] = -L_2[\hat{u}_{21}(-x), \hat{\eta}_{21}(-x)], \quad (4.55)$$

which imply that $\hat{u}_{21}(x)$ and $\hat{\eta}_{21}(x)$ are odd functions. Therefore, we have

$$\int_{-\infty}^{\infty}(\hat{\eta}_{21}u_s + \hat{u}_{21}\eta_s)dx = 0. \quad (4.56)$$

Likewise, from

$$L_1[\hat{u}_{22}(x), \hat{\eta}_{22}(x)] = -L_1[\hat{u}_{22}(-x), \hat{\eta}_{22}(-x)], \quad (4.57)$$

$$L_2[\hat{u}_{22}(x), \hat{\eta}_{22}(x)] = -L_2[\hat{u}_{22}(-x), \hat{\eta}_{22}(-x)]. \quad (4.58)$$

we can see that $\hat{u}_{22}(x)$ and $\hat{\eta}_{22}(x)$ are odd functions, which gives

$$\int_{-\infty}^{\infty}(\hat{\eta}_{22}u_s + \hat{u}_{22}\eta_s)dx = 0. \quad (4.59)$$

Substituting equations (4.56) and (4.59) into equation (4.53), the solvability condition can be further reduced to

$$(2\lambda_1\lambda_2 + r_1\lambda_1^2)\frac{\partial}{\partial c}\int_{-\infty}^{\infty}(\eta_s u_s)dx = i\int_{-\infty}^{\infty}(\eta_s u_s \hat{v}_2)dx. \quad (4.60)$$

To evaluate λ_2, we have to find $\hat{v}_2$ by solving equation (4.42). By substituting the solutions of $\hat{\eta}_1$, $\hat{u}_1$, and $\hat{v}_1$ into equation (4.42), and combining with equation (4.6), we can obtain

$$-c\frac{\partial \hat{v}_2}{\partial x} = -i\lambda_1 \left(\eta_s u_s - \eta_s \frac{\partial \eta_s}{\partial c} + \frac{1}{3}\frac{\partial D}{\partial c} \right) - icr_1 \frac{\partial u_s}{\partial x}, \tag{4.61}$$

where

$$D = \eta_s^3 \left[(-c + u_s) \frac{\partial^2 u_s}{\partial x^2} - \left(\frac{\partial u_s}{\partial x} \right)^2 \right].$$

After substituting into equation (4.60) the solitary wave solutions u_s and η_s given, from equations (4.5)–(4.6), by

$$\eta_s(x) = 1 + a\ \mathrm{sech}^2(kx),\ u_s(x) = \frac{ac\ \mathrm{sech}^2(kx)}{1 + a\ \mathrm{sech}^2(kx)},\ \text{and}\ \eta_s(-c + u_s) = -c,$$

with $k^2 = \frac{3a}{4(1+a)}$ and integrating the left-hand side of equation (4.60) by parts, we obtain

$$\int_{-\infty}^{\infty} (\eta_s u_s \hat{v}_2)\, dx = \frac{ac}{k} \left[\hat{v}_2(+\infty) + \hat{v}_2(-\infty) \right] + ir_1 \int_{-\infty}^{\infty} \left(\eta_s u_s^2 \right) dx, \tag{4.62}$$

where we have used

$$\int_{-\infty}^{\infty} \tanh(kx) \left(\eta_s u_s - \eta_s \frac{\partial \eta_s}{\partial c} + \frac{1}{3}\frac{\partial D}{\partial c} \right) dx = 0. \tag{4.63}$$

By using equations (4.43) and (4.62), we can simplify equation (4.60) to obtain

$$2\lambda_1\lambda_2 \frac{\partial}{\partial c} \int_{-\infty}^{\infty} (\eta_s u_s)\, dx = i\frac{ac}{k} \left[\hat{v}_2(+\infty) + \hat{v}_2(-\infty) \right]. \tag{4.64}$$

Therefore, in order to find λ_2, we only need to find the value of $\hat{v}_2$ at $x = \pm\infty$. Integrating equation (4.61) with respect to x once yields

$$\begin{aligned} \frac{c}{i\lambda_1}\hat{v}_2(x) = &\left[\frac{ac}{k} - \frac{\partial}{\partial c}\left(\frac{3a + a^2}{3k} \right) + \frac{1}{6}\frac{\partial}{\partial c}\left(\frac{8}{3}kac^2 + 8kc^2 \right) \right] \tanh(kx) \\ &- \frac{1}{6}\frac{\partial}{\partial c} \left[\left(8k^2ac^2 + 8k^2c^2 \right) \int_{-\infty}^{x} \frac{dt}{a + \cosh^2(kt)} \right] + \mathrm{Term}(x) + E, \end{aligned} \tag{4.65}$$

where E is an integration constant and

$$\begin{aligned}\mathrm{Term}(x) = -icr_1 u_s(x) - \frac{(3a+a^2)\,\frac{\partial k}{\partial c}x}{3k\cosh^2(kx)} - \frac{\frac{\partial}{\partial c}\left(\frac{a^2}{6k}\right)\sinh(kx)}{\cosh^3(kx)} \\ + \frac{\partial}{\partial c}\left(\frac{2kac^2\sinh(kx)}{9\cosh^3(kx)}\right) - \frac{a^2\left(\cosh^2(kx) - 3\sinh^2(kx)\right)\frac{\partial k}{\partial c}x}{3k\cosh^4(kx)},\end{aligned}$$

which vanishes as $x \to \pm\infty$.

From equation (4.65), we can see that as $x \to \pm\infty$, $\hat{v}_2(x)$ does not tend to zero no matter what the integration constant E is, i.e., this solution $\hat{v}_2(x)$ does not satisfy the boundary conditions shown in equation (4.16). We should call that $\hat{u}_2$, $\hat{v}_2$, and $\hat{\eta}_2$ near-field solutions. In order to satisfy the boundary conditions as $x \to \pm\infty$, we need to find far-field solutions whose varies much more slowly in x. By matching the near-field and far-field solutions, we can find the values of $\hat{v}_2(\infty)$ and $\hat{v}_2(-\infty)$ to determine the value of λ_2.

In order to find far-field solutions, we introduce two slow scales x_1 and x_2 defined by

$$x_1 = \epsilon x, \quad x_2 = \epsilon^2 x, \tag{4.66}$$

where ϵ is the small parameter measuring the small wave number in the transverse direction. Then we look for solutions of equations (4.10)–(4.12) in the following power series in ϵ which depend on x_1 and x_2 as

$$\hat{u}(x_1, x_2) = \epsilon^2 \hat{u}_{F2} + \epsilon^3 \hat{u}_{F3} + \cdots, \tag{4.67}$$

$$\hat{\eta}(x_1, x_2) = \epsilon^4 \hat{\eta}_{F4} + \epsilon^5 \hat{\eta}_{F5} + \cdots, \tag{4.68}$$

$$\hat{v}(x_1, x_2) = \epsilon^2 \hat{v}_{F2} + \epsilon^3 \hat{v}_{F3} + \cdots, \tag{4.69}$$

where subscript F represents far-field solutions.

Substituting equations (4.67)–(4.69) into equations (4.10)–(4.12), collecting the same order terms in ϵ, and using the fact that

$$u_s(x) = 0,\ \eta_s(x) = 1 \text{ as } x \to \pm\infty,$$

we have, for order $O(\epsilon^3)$,

$$\frac{\partial \hat{u}_{F2}}{\partial x_1} + i\hat{v}_{F2} = 0, \tag{4.70}$$

$$\lambda_1 \hat{u}_{F2} - c\frac{\partial \hat{u}_{F2}}{\partial x_1} = 0, \tag{4.71}$$

$$\lambda_1 \hat{v}_{F2} - c\frac{\partial \hat{v}_{F2}}{\partial x_1} = 0. \tag{4.72}$$

whose solutions can be found as

$$\hat{u}_{F2}(x_1, x_2) = A(x_2)e^{(\frac{\lambda_1}{c}x_1)}, \quad \hat{v}_{F2}(x_1, x_2) = i\frac{\lambda_1}{c}A(x_2)e^{(\frac{\lambda_1}{c}x_1)}, \tag{4.73}$$

where $A(x_2)$ is an arbitrary function of x_2.

For order $O(\epsilon^4)$, we have

$$\frac{\partial \hat{u}_{F3}}{\partial x_1} + \frac{\partial \hat{u}_{F2}}{\partial x_2} + i\hat{v}_{F3} = 0, \tag{4.74}$$

$$\lambda_1 \hat{u}_{F3} - c\frac{\partial \hat{u}_{F3}}{\partial x_1} = c\frac{\partial \hat{u}_{F2}}{\partial x_2} - \lambda_2 \hat{u}_{F2}, \tag{4.75}$$

$$\lambda_1 \hat{v}_{F3} - c\frac{\partial \hat{v}_{F3}}{\partial x_1} = c\frac{\partial \hat{v}_{F2}}{\partial x_2} - \lambda_2 \hat{v}_{F2}. \tag{4.76}$$

In order to remove the secular terms, the inhomogeneous terms in equations (4.75)–(4.76) should vanish, which gives

$$c\frac{\partial \hat{u}_{F2}}{\partial x_2} - \lambda_2 \hat{u}_{F2} = 0, \tag{4.77}$$

$$c\frac{\partial \hat{v}_{F2}}{\partial x_2} - \lambda_2 \hat{v}_{F2} = 0. \tag{4.78}$$

After solving equations (4.77)–(4.78), we have, from equation (4.73),

$$A(x_2) = D_{\pm}e^{\frac{\lambda_2}{c}x_2}, \quad \hat{v}_{F2}(x_1, x_2) = iD_{\pm}\frac{\lambda_1}{c}e^{\frac{\lambda_2}{c}x_2}e^{\frac{\lambda_1}{c}x_1}, \tag{4.79}$$

where $D_\pm$ are constants for $x_2 > 0$ and $x_2 < 0$, respectively.

Next we have to match the near-field solution $\hat{v}_2$ in equation (4.65) with the far-field solution $\hat{v}_{F2}$ in equation (4.79).

Without losing generality, we assume $c > 0$. If $\mathrm{Re}(\lambda_2) < 0$, we have, after imposing the boundary condition on the far-field solution and matching $\hat{v}_2$ with $\hat{v}_{F2}$ at $x = -\infty$

$$D_- = 0,\ \hat{v}_2(-\infty) = 0,\ E = A,\ \hat{v}_2(+\infty) = \frac{i\lambda_1}{c}(2A - B),\ D_+ = 2A - B,$$

where A and B are defined by

$$A = \frac{ac}{k} - \frac{\partial}{\partial c}\left(\frac{3a + a^2}{3k}\right) + \frac{1}{6}\frac{\partial}{\partial c}\left(\frac{8}{3}kac^2 + 8kc^2\right),$$
$$B = \frac{1}{6}\frac{\partial}{\partial c}\left[(8k^2ac^2 + 8k^2c^2)\int_{-\infty}^{\infty}\frac{dx}{a + \cosh^2(kx)}\right].$$

From equation

$$2\lambda_1\lambda_2\frac{\partial}{\partial c}\int_{-\infty}^{\infty}(\eta_s u_s)dx = i\frac{ac}{k}[\hat{v}_2(+\infty) + \hat{v}_2(-\infty)],$$

and using the fact that $\frac{\partial}{\partial c}\int_{-\infty}^{\infty}(\eta_s u_s)dx > 0$, we find that

$$2\lambda_2\frac{\partial}{\partial c}\int_{-\infty}^{\infty}(\eta_s u_s)dx = -\frac{a}{k}(2A - B), \quad \text{when} \ \ (2\mathrm{A} - \mathrm{B}) > 0. \tag{4.80}$$

If $\mathrm{Re}(\lambda_2) > 0$, we obtain, after imposing the boundary condition on the far-field solution and matching $\hat{v}_2$ with $\hat{v}_{F2}$ at $x = +\infty$,

$$D_+ = 0,\ \hat{v}_2(+\infty) = 0,\ E = B - A,\ \hat{v}_2(-\infty) = \frac{i\lambda_1}{c}(B - 2A),\ D_- = B - 2A,$$

and

$$2\lambda_2\frac{\partial}{\partial c}\int_{-\infty}^{\infty}(\eta_s u_s)dx = \frac{a}{k}(2A - B), \quad \text{when} \ \ (2\mathrm{A} - \mathrm{B}) > 0. \tag{4.81}$$

Finally we can find an expression of λ_2 as:

$$\lambda_2 = \begin{cases} \pm\frac{a(2A-B)}{2k\frac{\partial}{\partial c}\int_{-\infty}^{\infty}(\eta_s u_s)dx} & : \text{ if } (2\text{A} - \text{B}) > 0, \\ \text{no solution} & : \text{ if } (2\text{A} - \text{B}) < 0 \end{cases}$$

which gives us a sufficient condition for transverse instability as $a > 3.41$.

CHAPTER 5

NUMERICAL STUDY OF THE STRONGLY NONLINEAR WEAKLY 2D LONG WAVE MODEL

5.1 Linear Dispersion Relationship

An accurate numerical method to solve the strongly nonlinear long wave model should at least preserve the original dispersion relationship when the model is discretized. To develop a grid system that better represents the dispersion relationship of the continuous system, we first will consider the linearized system of equations (2.1)–(2.2).

After non-dimensionalizing equations (2.1)–(2.2) with respect to h and $(h/g)^{1/2}$ which are the characteristic length and time scales, respectively, we first substitute $u = u'$, $v = v'$, and $\eta = 1 + \eta'$ into (2.1)–(2.2). Then, by assuming that $|u'| \ll 1$, $|v'| \ll 1$, and $|\eta'| \ll 1$. we can obtain the linearized system, after dropping the primes, as

$$\frac{\partial \eta}{\partial t} = -\left(\frac{\partial u}{\partial x} + \frac{\partial v}{\partial y}\right), \tag{5.1}$$

$$\frac{\partial}{\partial t}\left[u - \frac{1}{3}\left(\frac{\partial^2 u}{\partial x^2} + \frac{\partial^2 v}{\partial x \partial y}\right)\right] = -\frac{\partial \eta}{\partial x}, \tag{5.2}$$

$$\frac{\partial}{\partial t}\left[v - \frac{1}{3}\left(\frac{\partial^2 u}{\partial x \partial y} + \frac{\partial^2 v}{\partial y^2}\right)\right] = -\frac{\partial \eta}{\partial y}. \tag{5.3}$$

After substituting the following equations (5.4)–(5.7) into equations (5.1)–(5.3)

$$u(x, y, t) = a \exp^{i(k_1 x + k_2 y - \omega t)}, \tag{5.4}$$

$$v(x, y, t) = b \exp^{i(k_1 x + k_2 y - \omega t)}, \tag{5.5}$$

$$\eta(x, y, t) = d \exp^{i(k_1 x + k_2 y - \omega t)}, \tag{5.6}$$

we can obtain the following linear dispersion relationship for the continuous system:

$$\omega(k_1, k_2) = k\sqrt{\frac{3}{3 + k^2}}, \tag{5.7}$$

where $k^2 = k_1^2 + k_2^2$.

When we use an uniform grid finite difference method to solve the linearized equations (5.1)–(5.3), three different arrangements of grid points are possible:
A. We evaluate $u(x, y, t)$ and $v(x, y, t)$ on the grid points, but evaluate $\eta(x, y, t)$ in the middle of each grid cell, as shown in the Figure 5.1.

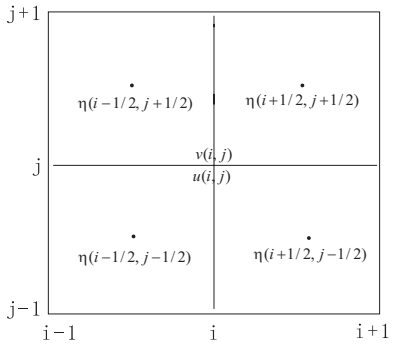

Figure 5.1 First arrangement of the grid points.

Then, the corresponding dispersion relationship is given by

$$\omega_1^2(k_1, k_2) = \frac{3\left[B + 4\sin^2\frac{k_1h_1}{2}\sin^2(k_2h_2) - 2\sin^2(k_1h_1)\sin^2(k_2h_2)\right]}{A - \sin^2(k_1h_1)\sin^2(k_2h_2)}, \tag{5.8}$$

where h_1 and h_2 are the grid sizes in the x- and y-directions, respectively, and

$$A = h_1^2\left(9h_2^2 + 12\sin^2\frac{k_2h_2}{2}\right) + \sin^2\frac{k_1h_1}{2}\left(12h_2^2 + 16\sin^2\frac{k_2h_2}{2}\right),$$
$$B = 12h_2^2\sin^2\frac{k_1h_1}{2}\cos^2\frac{k_2h_2}{2} + 4\sin^2\frac{k_2h_2}{2}\left[\sin^2(k_1h_1) + 3h_1^2\cos^2\frac{k_1h_1}{2}\right].$$

B. We evaluate $\eta(x, y, t)$ on the grid points, but evaluate $u(x, y, t)$ and $v(x, y, t)$ on the faces of each grid cell, as shown in Figure 5.2.

Then, the corresponding dispersion relationship is given by

$$\omega_2^2(k_1, k_2) = \frac{3\left[B - \sin^2(k_1h_1)\sin^2(k_2h_2)\right]}{A - \sin^2(k_1h_1)\sin^2(k_2h_2)}, \tag{5.9}$$

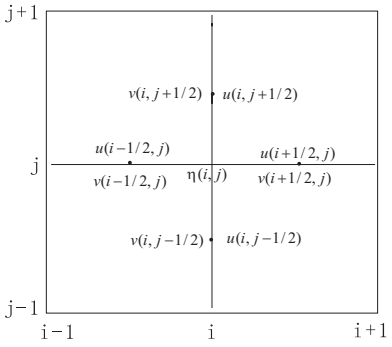

Figure 5.2 Second arrangement of the grid points.

where

$$A = h_1^2\left(9h_2^2 + 12\sin^2\frac{k_2h_2}{2}\right) + \sin^2\frac{k_1h_1}{2}\left(12h_2^2 + 16\sin^2\frac{k_2h_2}{2}\right),$$
$$B = 12h_2^2\sin^2\frac{k_1h_1}{2} + 3\sin^2(k_2h_2)\cos^2\frac{k_1h_1}{2} + 16\sin^2\frac{k_1h_1}{2}\sin^2\frac{k_2h_2}{2}.$$

C. We evaluate $\eta(x, y, t)$, $u(x, y, t)$, and $v(x, y, t)$ on the same grid points, as shown in Figure 5.3.

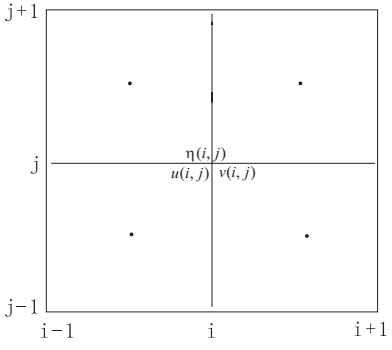

Figure 5.3 Third arrangement of the grid points.

Then, the corresponding dispersion relationship is given by

$$\omega_3^2(k_1, k_2) = \frac{3\left[B + 3h_1^2\sin^2(k_2h_2) - 2\sin^2(k_1h_1)\sin^2(k_2h_2)\right]}{A - \sin^2(k_1h_1)\sin^2(k_2h_2)}, \tag{5.10}$$

where

$$A = h_1^2\left(9h_2^2 + 12\sin^2\frac{k_2h_2}{2}\right) + \sin^2\frac{k_1h_1}{2}\left(12h_2^2 + 16\sin^2\frac{k_2h_2}{2}\right),$$

$$B = 3h_2^2\sin^2(k_1h_1) + 4\left[\sin^2(k_1h_1)\sin^2\frac{k_2h_2}{2} + \sin^2\frac{k_1h_1}{2}\sin^2(k_2h_2)\right].$$

As shown in Figure 5.4, when comparing these dispersion relationships ω_1, ω_2, ω_3 with ω, we can see that ω_1 matches with ω better than ω_2 and ω_3; therefore a staggered grid system A for η, u, and v is chosen to solve the 2D long wave model numerically.

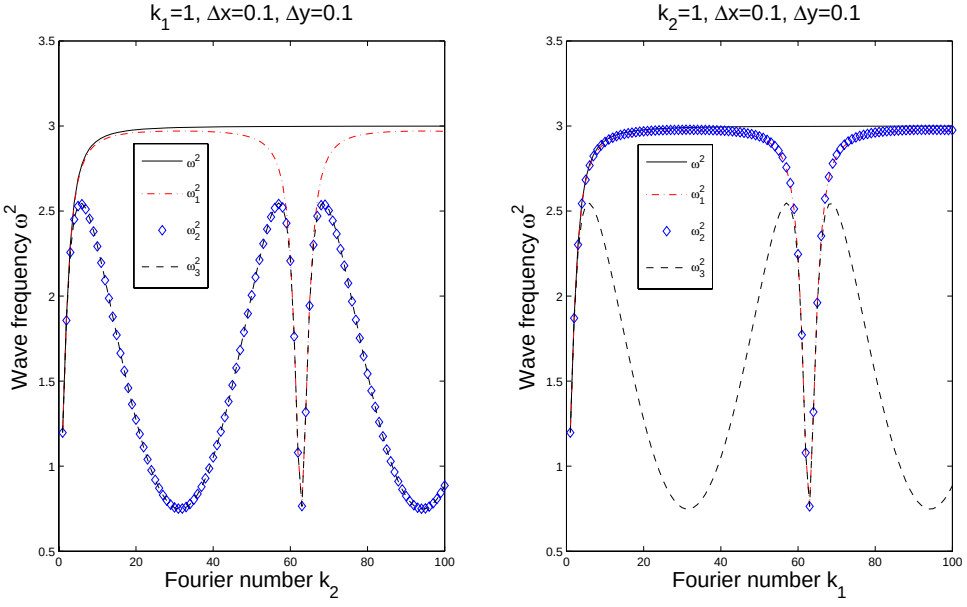

Figure 5.4 Comparison of dispersion relationships: solid line, dash dot line, $\diamond$ line and dash line represents ω, ω_1, ω_2, and ω_3, respectively. In the left panel, $k_1 = 1$ is fixed, and $\triangle x = \triangle y = 0.1$. In the right panel, $k_2 = 1$ is fixed, and $\triangle x = \triangle y = 0.1$.

5.2 Numerical Method to Solve the Weakly 2D Long Wave Model

In §2.2, the weakly 2D long wave model was derived as

$$\frac{\partial \eta}{\partial t} = -\left[\frac{\partial}{\partial x}(\eta u) + \frac{\partial}{\partial y}(\eta v)\right], \tag{5.11}$$

$$\frac{\partial}{\partial t}\left[\eta u - \frac{\partial}{\partial x}\left(\frac{\eta^3}{3}\frac{\partial u}{\partial x}\right)\right] = -\frac{\partial}{\partial x}\left(\eta u^2 + \frac{\eta^2}{2}\right) - \frac{\partial}{\partial y}(\eta u v) + \frac{\partial}{\partial x}\left[\frac{\partial}{\partial x}\left(\frac{\eta^3}{3}u\frac{\partial u}{\partial x}\right) + \frac{\eta^3}{3}\left(\frac{\partial u}{\partial x}\right)^2\right], \tag{5.12}$$

$$\frac{\partial}{\partial t}\left[\eta v - \frac{\partial}{\partial y}\left(\frac{\eta^3}{3}\frac{\partial u}{\partial x}\right)\right] = -\frac{\partial}{\partial x}(\eta u v) - \frac{\partial}{\partial y}\left(\eta v^2 + \frac{\eta^2}{2}\right) + \frac{\partial}{\partial y}\left[\frac{\partial}{\partial x}\left(\frac{\eta^3}{3}u\frac{\partial u}{\partial x}\right) + \frac{\eta^3}{3}\left(\frac{\partial u}{\partial x}\right)^2\right], \tag{5.13}$$

where $\eta = 1 + \zeta$ with ζ being the surface wave elevation. u and v are the depth-averaged horizontal velocities in the x- and y-directions, respectively. In this section, we will describe a finite difference method to solve equations (5.11)–(5.13) numerically.

Let

$$U = \eta u - \eta^2 \frac{\partial \eta}{\partial x}\frac{\partial u}{\partial x} - \frac{\eta^3}{3}\frac{\partial^2 u}{\partial x^2}, \tag{5.14}$$

$$V = \eta v - \eta^2 \frac{\partial \eta}{\partial y}\frac{\partial u}{\partial x} - \frac{\eta^3}{3}\frac{\partial^2 u}{\partial x \partial y}, \tag{5.15}$$

$$E = \frac{\partial}{\partial x}(\eta u) + \frac{\partial}{\partial y}(\eta v), \tag{5.16}$$

$$F = -\frac{\partial}{\partial x}\left(\eta u^2 + \frac{\eta^2}{2}\right) - \frac{\partial}{\partial y}(\eta u v) + \frac{\partial H}{\partial x}, \tag{5.17}$$

$$G = -\frac{\partial}{\partial x}(\eta u v) - \frac{\partial}{\partial y}\left(\eta v^2 + \frac{\eta^2}{2}\right) + \frac{\partial H}{\partial y}, \tag{5.18}$$

where

$$H = \frac{\partial}{\partial x}\left(\frac{\eta^3}{3}u\frac{\partial u}{\partial x}\right) + \frac{\eta^3}{3}\left(\frac{\partial u}{\partial x}\right)^2.$$

Then, the weakly 2D model given by (5.11)–(5.13) can be rewritten as

$$\frac{\partial \eta}{\partial t} = -E, \quad \frac{\partial U}{\partial t} = F, \quad \frac{\partial V}{\partial t} = G. \tag{5.19}$$

We first discretize the independent space variables as $x = i\triangle x,\ i = 1, 2, \cdots,\ N_1$, $y = j\triangle y,\ j = 1, 2, \cdots,\ N_2$, where N_1 and N_2 are the numbers of grid points in the x- and y-directions, respectively. Then we use 4th-order finite difference formulas to approximate spatial derivatives. Then, the discretized system can be written as

$$\frac{\partial \eta_{i+\frac{1}{2},j+\frac{1}{2}}}{\partial t} = -E_{i+\frac{1}{2},j+\frac{1}{2}}, \quad \frac{\partial U_{i,j}}{\partial t} = F_{i,j}, \quad \frac{\partial V_{i,j}}{\partial t} = G_{i,j}, \tag{5.20}$$

where the subscript (i, j) represents a position at $(x, y) = (i\triangle x, j\triangle y)$ while $\left(i + \frac{1}{2}, j + \frac{1}{2}\right)$ represents a position at $(x, y) = \left(\left(i + \frac{1}{2}\right)\triangle x, \left(j + \frac{1}{2}\right)\triangle y\right)$.

After the right-hand sides of (5.20) are evaluated, we use a 4th-order Adams-Bashforth (predictor-corrector) method introduced in Section 3.3 to integrate (5.20) in time. Once $\eta_{i+\frac{1}{2},j+\frac{1}{2}}$, $u_{i,j}$, and $v_{i,j}$ are known at time levels $n-4,\ n-3,\ n-2,\ n-1$, where $n = 1, 2, \cdots M$ with M being the total number of time steps, it is straightforward to compute $\eta_{i+\frac{1}{2},j+\frac{1}{2}}$, $U_{i,j}$ and $V_{i,j}$ at time level n from equations (5.20).

To find the horizontal velocity $u_{i,j}$ at time level n for a fixed j, we have to solve a linear system of $Au_{i,j} = U_{i,j}$, where A is a $N_1 \times N_1$ pentacyclic matrix which can be inverted effectively. Once $V_{i,j}$, $u_{i,j}$, and $\eta_{i,j}$ are known at time level n, it is easy to compute $v_{i,j}$ from equation (5.14) at time level n.

To compute $\eta_{i,j}$, $u_{i+\frac{1}{2},j+\frac{1}{2}}$, and $v_{i+\frac{1}{2},j+\frac{1}{2}}$ from $\eta_{i+\frac{1}{2},j+\frac{1}{2}}$, $u_{i,j}$, and $v_{i,j}$, we use the following fourth-order averaging method for consistency with our spatial discretization:

$$\begin{aligned} f_{i,j} = {} & \frac{9\left(f_{i+\frac{1}{2},j+\frac{1}{2}} + f_{i-\frac{1}{2},j+\frac{1}{2}} + f_{i-\frac{1}{2},j-\frac{1}{2}} + f_{i+\frac{1}{2},j-\frac{1}{2}}\right)}{32} \\ & - \frac{f_{i-\frac{3}{2},j+\frac{3}{2}} + f_{i+\frac{3}{2},j+\frac{3}{2}} + f_{i-\frac{3}{2},j-\frac{3}{2}} + f_{i+\frac{3}{2},j-\frac{3}{2}}}{32} + O\left((\triangle x)^4, (\triangle y)^4\right), \end{aligned} \tag{5.21}$$

$$\begin{aligned} f_{i+\frac{1}{2},j+\frac{1}{2}} = {} & \frac{9\left(f_{i+1,j+1} + f_{i,j+1} + f_{i,j} + f_{i+1,j}\right)}{32} \\ & - \frac{f_{i-1,j+2} + f_{i+2,j+2} + f_{i-1,j-1} + f_{i+2,j-1}}{32} + O\left((\triangle x)^4, (\triangle y)^4\right), \end{aligned} \tag{5.22}$$

where $f = (\eta,\ u,\ v)$. Because the Adams-Bashforth method is a multiple step method, we use a 4th-order Runge-Kutta method to compute $\eta_{i+\frac{1}{2},j+\frac{1}{2}}$, $u_{i,j}$, and $v_{i,j}$ at the first time levels, $n = 1, 2, 3$.

We validate our numerical method for a solitary wave propagating in the x-direction, for which η and u can be written as

$$\eta\,(x,t) = 1 + a\ \mathrm{sech}^2[k\,(x - ct)], \tag{5.23}$$

$$u\,(x,t) = \frac{c\,(\eta - 1)}{\eta}, \quad v\,(x,t) = 0, \tag{5.24}$$

with initial conditions

$$\eta\,(x,0) = 1 + a\ \mathrm{sech}^2(kx), \tag{5.25}$$

$$u\,(x,0) = ac\ \frac{\mathrm{sech}^2\,(kx)}{1 + a\ \mathrm{sech}^2(kx)}, \tag{5.26}$$

$$v\,(x,0) = 0, \tag{5.27}$$

where a is the wave amplitude. c is the wave speed given by $c = 1+a^2$, and $k^2 = \frac{3a}{4(1+a)}$. For our numerical computation for a solitary wave of $a = 0.5$, the computational domain is chosen to be $[-30, 30] \times [-500, 500]$. The numerical solution for a single solitary wave at $T = 100$ is shown in Figure 5.5 and is compared with the solitary wave solution at $y = 0$ in Figure 5.6. As demonstrated in Figure 5.7, the maximum relative error between the numerical and analytical solutions is smaller than $10^{-5.5}$ at $T = 100$ with $\triangle x = 0.05$ and $\triangle t = 0.005$.

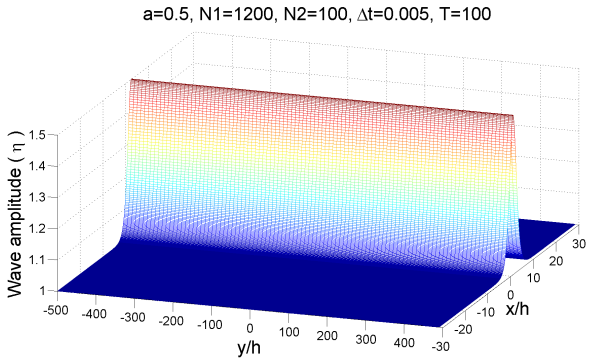

Figure 5.5 Numerical solution for a solitary wave propagating in the x-direction at $T = 100$.

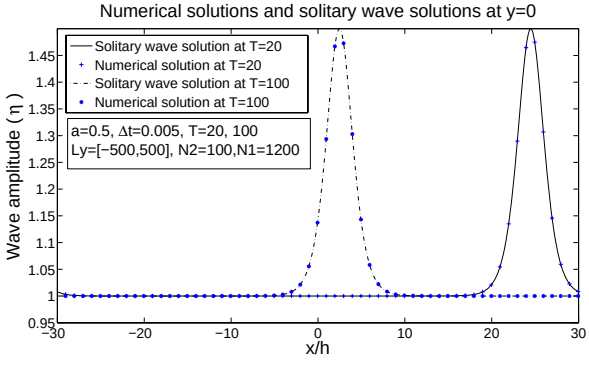

Figure 5.6 Numerical solution compared with the solitary wave solution of the SG equation. The solid line is the solitary wave solution and the '+' line is the numerical solution at $T = 20$. The dashed dot line is the solitary wave solution and * is the numerical solution at $T = 100$.

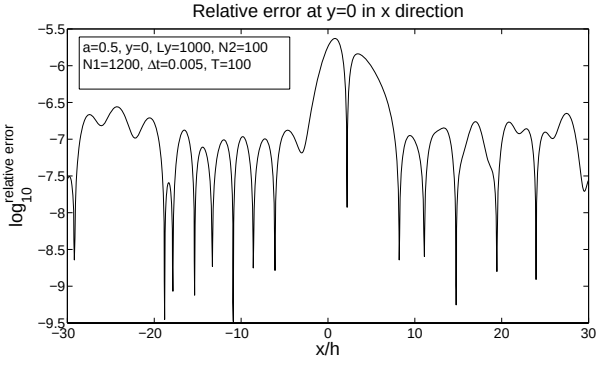

Figure 5.7 The relative error between the numerical solution and solitary wave solution of the SG equation at $T = 100$ for varying x with $y = 0$.

By rewriting the weakly 2D model given by equations (5.11)–(5.13) as

$$\begin{aligned}
\frac{\partial \eta}{\partial t} &= -\left[\frac{\partial}{\partial x}(\eta u) + \frac{\partial}{\partial y}(\eta v)\right], \\
\frac{\partial}{\partial t}(\eta u) &= -\frac{\partial}{\partial y}(\eta u v) - \frac{\partial}{\partial x}\left\{\eta u^2 + \frac{\eta^2}{2} - \frac{\eta^3}{3}\left[\frac{\partial^2 u}{\partial x \partial t} + u\frac{\partial^2 u}{\partial x^2} - \left(\frac{\partial u}{\partial x}\right)^2\right]\right\}, \\
\frac{\partial}{\partial t}(\eta v) &= -\frac{\partial}{\partial x}(\eta u v) - \frac{\partial}{\partial y}\left\{\eta v^2 + \frac{\eta^2}{2} - \frac{\eta^3}{3}\left[\frac{\partial^2 u}{\partial x \partial t} + u\frac{\partial^2 u}{\partial x^2} - \left(\frac{\partial u}{\partial x}\right)^2\right]\right\}.
\end{aligned}$$

it can be seen that the model conserves mass and horizontal momenta defined by

$$\int_{-\frac{L_y}{2}}^{\frac{L_y}{2}}\int_{-\frac{L_x}{2}}^{\frac{L_x}{2}} \eta \, dxdy, \quad \int_{-\frac{L_y}{2}}^{\frac{L_y}{2}}\int_{-\frac{L_x}{2}}^{\frac{L_x}{2}} \eta u \, dxdy, \quad \int_{-\frac{L_y}{2}}^{\frac{L_y}{2}}\int_{-\frac{L_x}{2}}^{\frac{L_x}{2}} \eta v \, dxdy.$$

To monitor these conserved quantities, we use the trapezoidal rule to integrate numerically η, ηu, and ηv over the computational domain and the results for the propagation of a single solitary wave are shown in Figure 5.8.

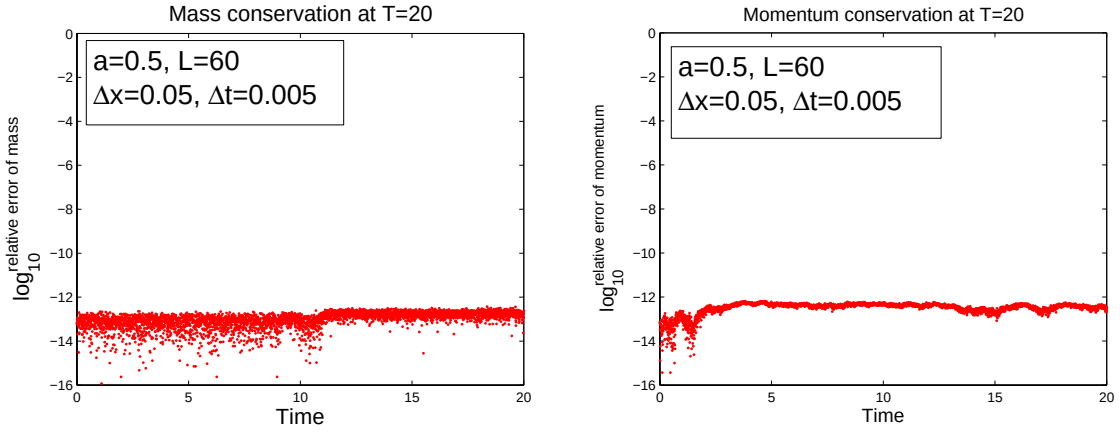

Figure 5.8 Mass and horizontal momentum conserved with relative error less than 10^{-12} and close to 10^{-12} at time $T = 20$ are shown in the left and right panels, respectively.

We also can check convergence of our numerical method in space by fixing time step $\triangle t$ and increasing the number of grids in the x-direction N_1 (i.e., decreasing $\triangle x$), as we did for the one-dimensional case. As shown in Figure 5.9, the slope of relative error is found to be close to 4, which is consistent with the accuracy of our numerical method.

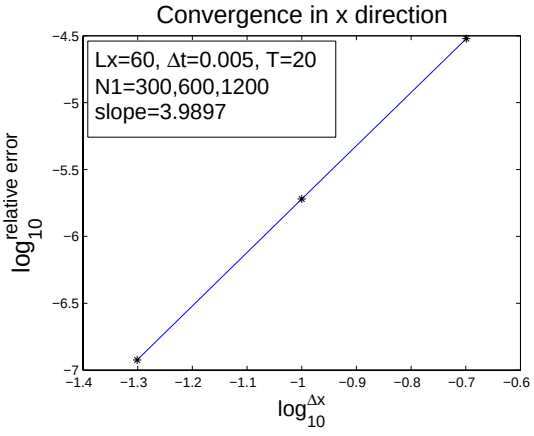

Figure 5.9 Convergence of the numerical method in space with $\triangle t = 0.005$, time $T = 20$ and $\triangle x = 0.2,\ 0.1,\ 0.05$, respectively.

A similar convergence test is carried out for the following initial conditions

$$\eta\left(x,\ y,\ 0\right) = \eta_s\left(x\right) + \gamma \frac{d\eta_s}{dx} \cos\left(\epsilon y\right), \tag{5.28}$$

$$u\left(x,\ y,\ 0\right) = u_s\left(x\right) + \gamma \frac{du_s}{dx} \cos\left(\epsilon y\right), \tag{5.29}$$

$$v\left(x,\ y,\ 0\right) = -\epsilon\gamma u_s\left(x\right) \sin\left(\epsilon y\right), \tag{5.30}$$

where η_s and u_s are the solitary wave solutions of the one-dimensional Su-Gardner equations. ϵ is the wave number in the y-direction, and γ is a small arbitrary constant. After assuming that $W_1,\ W_2$, and W_3 are three numerical solutions of the governing equations (5.11)–(5.13) at a fixed time T corresponding to three different grid sizes of $\triangle x,\ \frac{\triangle x}{2}$, and $\frac{\triangle x}{4}$, respectively, with fixing $\triangle y$ and $\triangle t$. If the error in the x-direction dominates that in the y-direction, we should have

$$\frac{\|W_1 - W_2\|}{\|W_2 - W_3\|} = 2^P,$$

where $\|\cdot\|$ represents infinity norm, P is the accuracy of the numerical method in the x-direction. Similarly, if the error in the y-direction dominates that in the x-direction, we can check convergence in the y-direction in the similar way. Since the accuracy

of our numerical method is 4th order both in the x- and y-directions, the value of P should be close to 4.

Numerical results for the convergence in the x- and y-directions with fixed $\epsilon = 0.01,\ \gamma = 0.1,\ \triangle t = 0.005$, and $T = 20$ are shown in Table 5.1 and Table 5.2, respectively. We can see that the value of the number P is very close to 4, this implies that the numerical accuracy in the x- and y-directions both are 4th-order.

Table 5.1 Convergence in the x-direction with fixed $\triangle y = \frac{\pi}{3}$ and $\triangle x = 0.2,\ 0.1$, and 0.05, respectively

$\triangle y$	$\triangle x_1$	$\triangle x_2$	$\triangle x_3$	P
$\frac{\pi}{3}$	0.2	0.1	0.05	3.98

Table 5.2 Convergence in the y-direction with fixed $\triangle x = 0.01$ and $\triangle y = \frac{20\pi}{3},\ \frac{10\pi}{3}$, and $\frac{5\pi}{3}$, respectively

$\triangle x$	$\triangle y_1$	$\triangle y_2$	$\triangle y_3$	P
0.01	$\frac{20\pi}{3}$	$\frac{10\pi}{3}$	$\frac{5\pi}{3}$	3.96

Conservation of mass and horizontal momenta are also examined and the results are shown in Figure 5.10 and Figure 5.11. It is found that The relative error is found less than 10^{-11}.

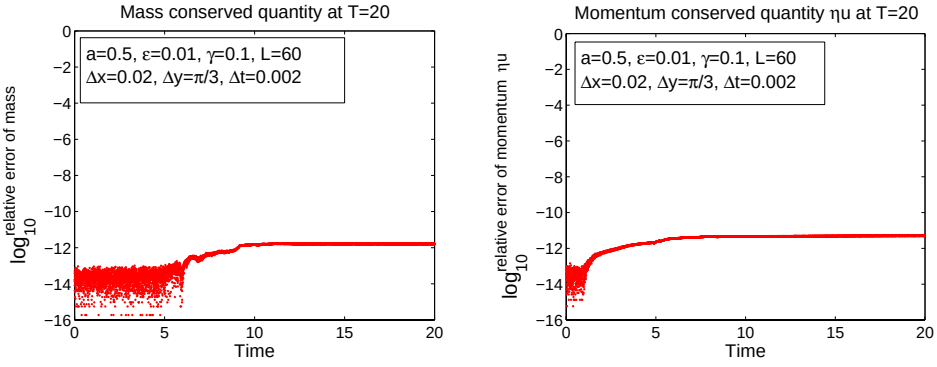

Figure 5.10 Mass η and horizontal momentum ηu conserved with relative error less than 10^{-11} at time $T = 20$ are shown in the left and right panels, respectively.

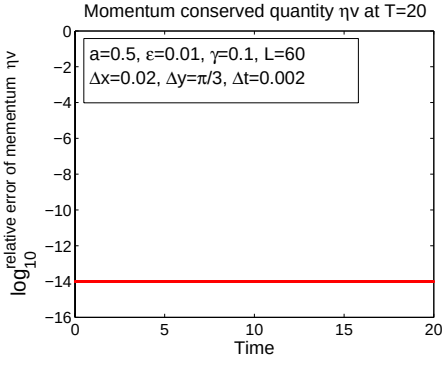

Figure 5.11 Horizontal momentum ηv is conserved with relative error less than 10^{-14} at time $T = 20$.

5.3 Numerical Simulations of Transverse Instability of Solitary Waves

In §4, we found a sufficient condition ($c > 2.1$, i.e., $a > 3.41$) for long wavelength transverse instability of solitary waves. Since the wave number (ϵ) in the y-direction is small, we can use the weakly 2D long wave model to investigate transverse instability numerically.

With assuming that the perturbation in the y-direction is very small, we can choose initial conditions as:

$$\eta\left(x,\ y,\ 0\right) = \eta_s\left(x\right) + \gamma \frac{d\eta_s}{dx} \cos\left(\epsilon y\right), \tag{5.31}$$

$$u\left(x,\ y,\ 0\right) = u_s\left(x\right) + \gamma \frac{du_s}{dx} \cos\left(\epsilon y\right), \tag{5.32}$$

$$v\left(x,\ y,\ 0\right) = -\epsilon\gamma u_s\left(x\right) \sin\left(\epsilon y\right), \tag{5.33}$$

where η_s and u_s are the solitary wave solutions of the one-dimensional Su-Gardner equations. ϵ is the wave number in the y direction, and γ is a small arbitrary constant. We have already shown the convergence of our numerical method for these initial conditions in Section 5.2.

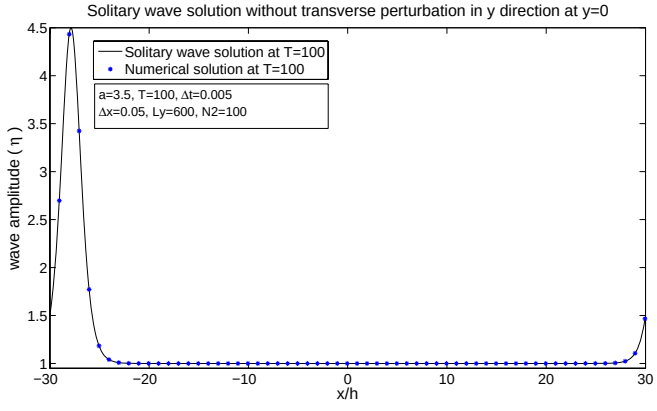

Figure 5.12 The solid line is the solitary wave solution and the '*' line is the numerical solution in the x-direction without transverse perturbation in the y-direction at time $T = 100$ with $y = 0$ and wave amplitude $a = 3.5$.

When there is no perturbation (i.e., $\epsilon = 0,\ \gamma = 0$), the numerical solution for a single solitary wave shows no sign of instability even for the wave amplitude $a = 3.5$, which is above the critical wave amplitude. Figure 5.12 shows the numerical solution at time $T = 100$. The maximum relative error between solitary wave solution and numerical solution at time $T = 100$ is less than 10^{-4}, which will been shown in Figure 5.13.

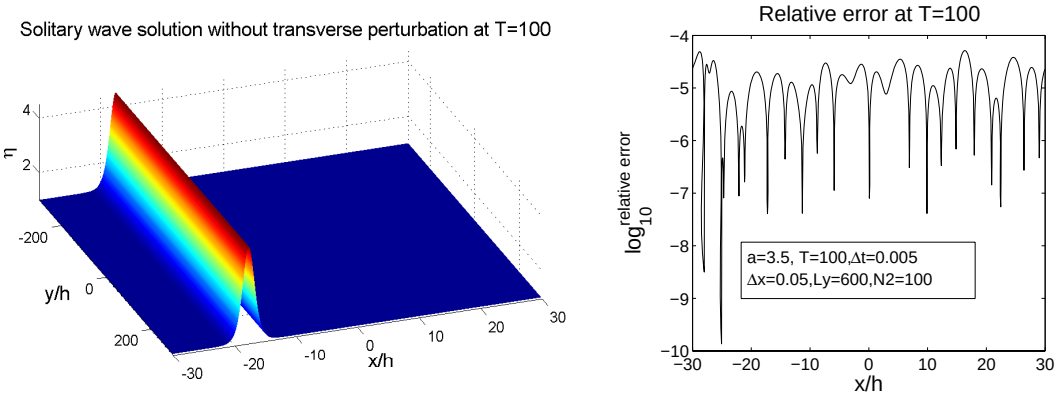

Figure 5.13 Numerical solution of the solitary wave in 3D form and the relative error between solitary wave solution and numerical solution are shown in the right and left panels, respectively. Where $a = 3.5,\ T = 100,\ \triangle t = 0.005,\ \triangle x = 0.05$, and $\triangle y = 6$.

Now we introduce a small perturbation depending on the y-direction with $a = 3.5$, $\epsilon = 0.01$, and $\gamma = 0.1$. Numerical solutions at time $T = 0$ and $T = 52$ are shown in Figure 5.14. We can see that the solitary wave becomes unstable and the growth of the initial perturbation is clearly observed at time $T = 52$. The free surface profiles along the x-direction at time $T = 50$ and $T = 52$ are also shown in Figure 5.15.

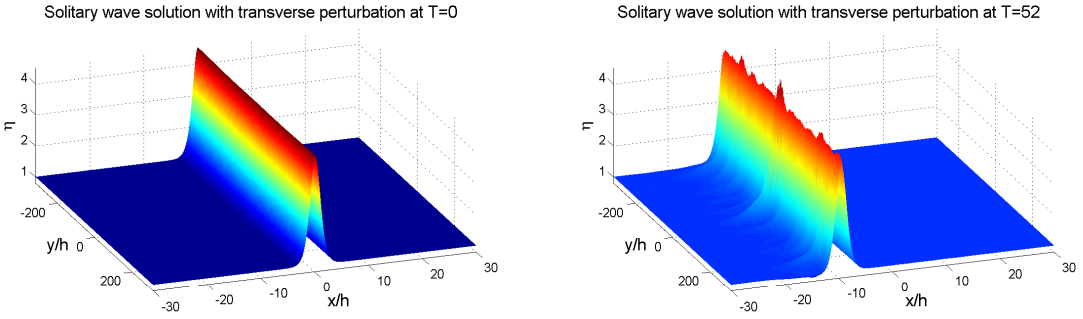

Figure 5.14 Numerical solutions of solitary wave with small transverse perturbation in the y-direction at time $T = 0$ and $T = 52$ are shown in the left and right panels, respectively. Where $a = 3.5$, $\epsilon = 0.01$, $\gamma = 0.1$, $\triangle t = 0.005$, $\triangle x = 0.05$, and $\triangle y = \frac{\pi}{3}$.

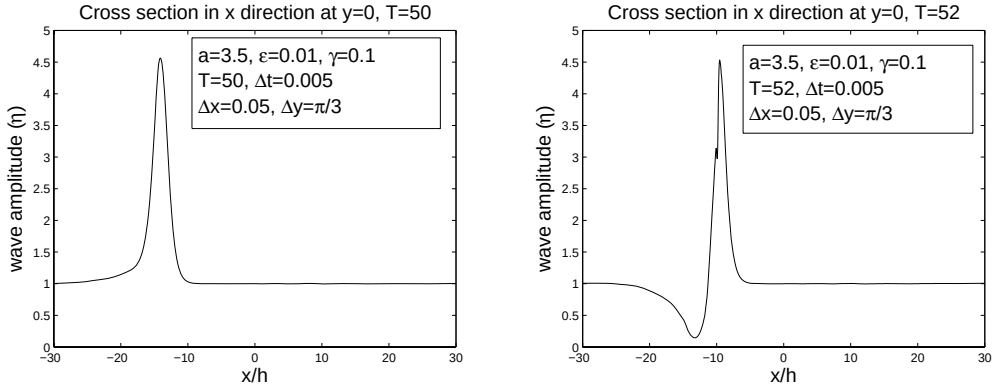

Figure 5.15 The cross section of numerical solutions of solitary wave with $y = 0$ in the x-direction at time $T = 50$ and $T = 52$ are shown in the left and right panels, respectively. Where $a = 3.5$, $\epsilon = 0.01$, $\gamma = 0.1$, $\triangle t = 0.005$, $\triangle x = 0.05$, and $\triangle y = \frac{\pi}{3}$.

As we mentioned before, $a > 3.41$ is only a sufficient condition for transverse instability. In Figure 5.16, when a small perturbation is introduced to a solitary wave with amplitude $a = 2$, we still can observe instability even though the wave amplitude is smaller than the critical value. The time when we observe instability ($T = 204$) is much longer than that for the case of $a = 3.5$. We should remark that this is not due to numerical instability since the solitary wave of the same amplitude is stable at least until $T = 400$, as shown in Figure 5.17.

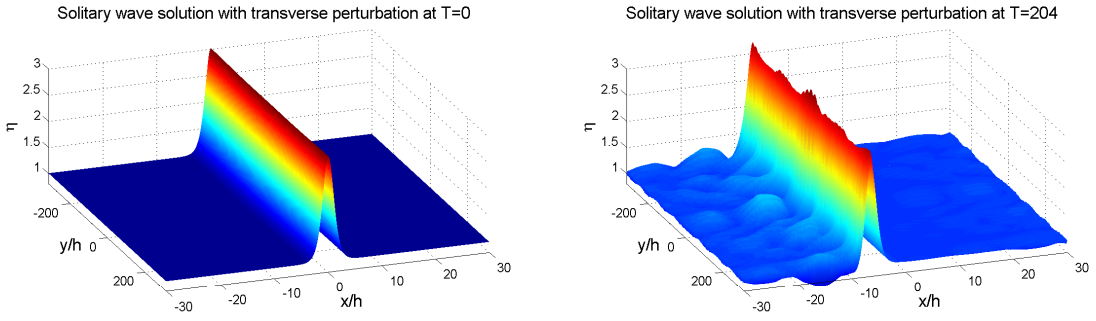

Figure 5.16 Numerical solutions of solitary wave with small transverse perturbation in the y-direction at time $T = 0$ and $T = 204$ are shown in the left and right panels, respectively. Where $a = 2,\ \epsilon = 0.01,\ \gamma = 0.1,\ \triangle t = 0.005,\ \triangle x = 0.05$, and $\triangle y = \frac{\pi}{3}$.

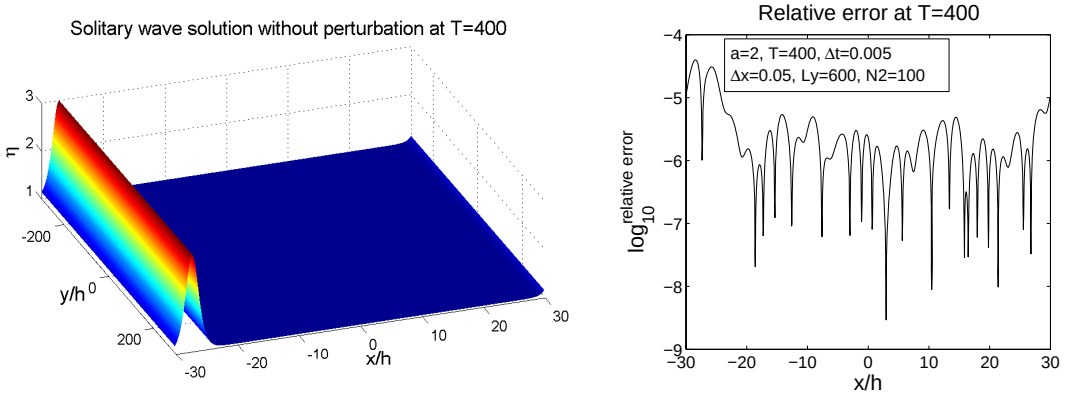

Figure 5.17 Numerical solution of the solitary wave in 3D form and the relative error between solitary wave solution and numerical solution are shown in the left and right panels, respectively. Where $a = 2,\ T = 400,\ \triangle t = 0.005,\ \triangle x = 0.05$, and $\triangle y = 6$.

5.4 Mach Reflection

5.4.1 Background

It has been known that the regular reflection of a solitary wave at a rigid wall is impossible when the incidence angle is sufficiently small. Instead, another type of reflection occurs and it is called 'Mach reflection' due to its geometrical similarity to the corresponding reflection of shock waves. In the Mach reflection, the apex of the incident and reflected waves then moves away from the wall at a constant angle ψ_* and is joined to the wall by a third solitary wave called 'Mach stem', as shown in Figure 5.18.

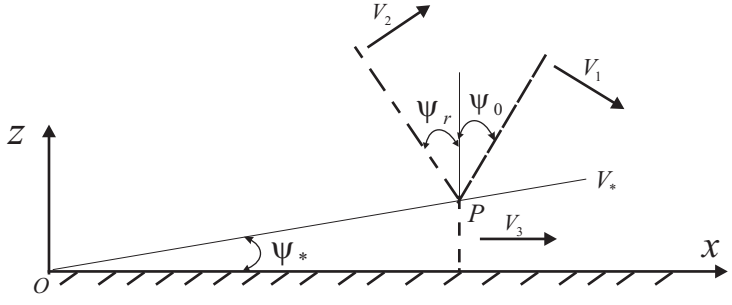

Figure 5.18 Mach reflection pattern, showing the incident wave (– – –), reflected wave (– - –), and the stem wave (- -). The entire pattern is expanding uniformly from the leading edge O, such that the apex P is moving with speed V_*.

The oblique incidence of a solitary wave of small wave amplitude on a vertical wall was studied theoretically by Miles [27] as a special case of the oblique interaction of two small-amplitude solitary waves, since they are equivalent if the viscous effect at the wall is neglected, as shown in Figure 5.19.

According to Miles' analysis [27] valid for the small incident wave amplitude ($a << 1$), the regular reflection is replaced by the Mach reflection when the angle of the incident wave ψ_0 is smaller than the critical angle ψ_c which is equal to $\sqrt{3a}$.

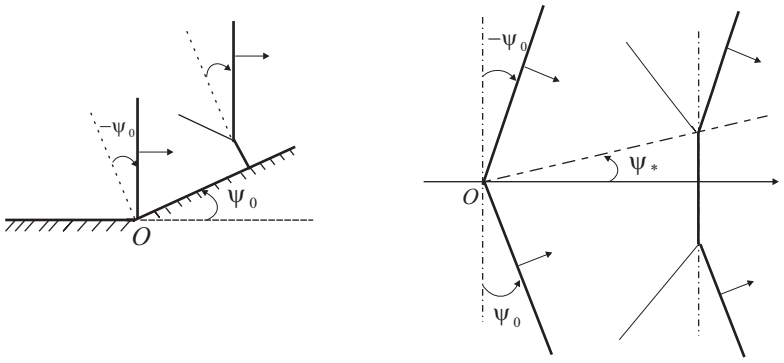

Figure 5.19 The Mach reflection. The left panel illustrates a semi-infinite line-soliton propagating parallel to the wall. The right panel is an equivalent system with two line-solitons propagating to the right when we ignore the viscous effect on the wall.

Then the amplification factor α is given by

$$\alpha = \begin{cases} (1+k)^2 & \text{Mach reflection,} \\ \frac{4}{1+\left(1-\frac{1}{k^2}\right)^{\frac{1}{2}}} & \text{regular reflection and } \psi_0 << 1, \\ 2 + \frac{3a}{\left(2\sin^2\psi_0 - 3 + 2\sin^2\psi_0\right)} & \text{regular reflection } \psi_0 = O(1). \end{cases}$$

where $\alpha = a_M/a$, a_M is the wave amplitude of the Mach stem, and $k = \frac{\psi_0}{\sqrt{3a}}$.

The Kadomtsev Petviashvili (KP) equation is a weakly nonlinear, weakly 2D model, which is relevant to study the Mach reflection when the wave amplitude is small. The KP equation has the exact solutions for not only solitons, but also their interaction [5]. Here, we consider only two types of solutions for the interaction between two solitary waves: one is the O-type solution describing the regular interaction and the other is the so-called (3142)-type solution relevant for the Mach reflection.

Based on the KP theory [5], when the angle of the incident wave ψ_0 is smaller then the critical angle ψ_c^{KP} which is given by $\left(\psi_c^{KP} = \frac{\tan\psi_0}{\sqrt{2A_0}}\right)$, the O-type solution becomes singular, *i.e.*, the Mach reflection occurs. This is illustrated in Figure 5.19.

When an incident wave represented by a vertical line is propagating to the right, and it hits a rigid wall with an angle ψ_0. If the angle of the incident wave is large, the reflected wave behind the incident wave propagates with an angle -ψ_0, i.e., the regular reflection occurs. However, if the angle is small, an intermediate wave called the Mach stem appears, as shown in the Figure 5.19. The critical angle for the Mach reflection is given by the angle ψ_c. From the analysis of the KP equation, it is known the maximum amplitude for this problem occurs at the wall and it was obtained by Kodama [5]: For the O-type solution (regular reflection) with $\tan\psi_0 > \tan\psi_c = \sqrt{2A_0}$, the amplification of the Mach stem A_M is given by

$$A_M = \frac{4A_0}{1+\sqrt{1-k^{-2}}}, \quad \text{with} \quad k = \frac{\tan\psi_0}{\sqrt{2A_0}} > 1, \tag{5.34}$$

while, for (3142)-type solution with $k < 1$, it is given by

$$A_M = A_0\,(1+k)^2\,, \tag{5.35}$$

where A_0 is the incident wave amplitude of the KP solitary wave.

5.4.2 Oblique Interaction of Two Solitary Waves

We study numerically the oblique interaction of two solitary waves with a small angle $2\psi_0$ by using the strongly nonlinear weakly 2D long wave model. Initial conditions are chosen by linearly superposing two solitary wave solutions of the SG equations propagating obliquely with an angle $2\psi_0$, or equivalently, in the x'- and x''-directions, respectively, as shown in Figure 5.20. With these initial conditions, our numerical simulations are equivalent to the (3412)-type solution of the KP equation if the wave amplitude is small. Since the (3412)-type solution and the (3142)-type solution of the KP equation are exactly the same locally near the Mach stem [5], we can simulate the evolution of the Mach stem by studying the oblique interaction of two solitary waves.

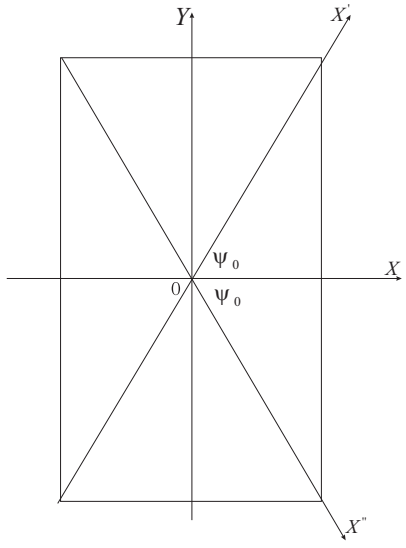

Figure 5.20 Two solitary waves propagate in x'- and x''-directions, respectively.

We first assume that these two solitary waves are periodic with period λ both in the x' and x'' directions. Notice the following relationships between (x, y), (x', y'), and (x'', y''):

$$x' = x\cos\psi_0 + y\sin\psi_0, \quad y' = -x\sin\psi_0 + y\cos\psi_0,$$
$$x'' = x\cos\psi_0 - y\sin\psi_0, \quad y'' = x\sin\psi_0 + y\cos\psi_0.$$

To satisfy the doubly periodic boundary conditions, we choose the lengths of the computational domain as $L_x = \lambda/\cos\psi_0$ for the x-direction and $L_y = \lambda/\sin\psi_0$ for the y-direction. Then, initial conditions can be written as

$$\begin{aligned}
\eta &= 1 + \eta_1 + \eta_2, \\
u &= c\left(\frac{\eta_1}{1+\eta_1} + \frac{\eta_2}{1+\eta_2}\right)\cos\psi_0, \\
v &= c\left(\frac{\eta_1}{1+\eta_1} + \frac{\eta_2}{1+\eta_2}\right)\sin\psi_0,
\end{aligned}$$

where $c^2 = 1 + a$ is the wave speed and

$$\eta_1 = a\ \mathrm{sech}^2\left[k\left(x\cos\psi_0 - y\sin\psi_0\right)\right],$$

$$\eta_2 = a\ \mathrm{sech}^2\left[k\left(x\cos\psi_0 + y\sin\psi_0\right)\right].$$

For the wave amplitude $a = 0.096$ and the incident angle $\psi_0 = \pi/6$ for which $k = \frac{\tan\psi_0}{\sqrt{3a}\cos\psi_0} > 1$, we expect the regular reflection. The numerical solutions for the free surface profiles are shown in Figure 5.21 while their contour plots at T=0,150, and 250 are shown in Figure 5.22.

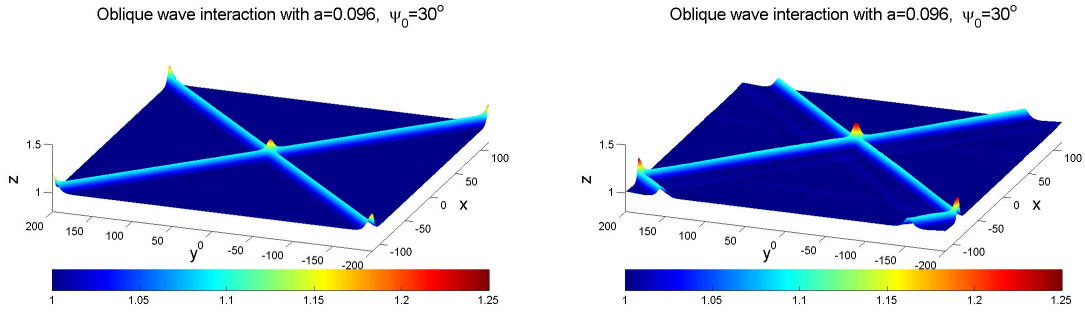

Figure 5.21 From left to right, these panels correspond to the numerical solutions at $T = 0$ and $T = 300$.

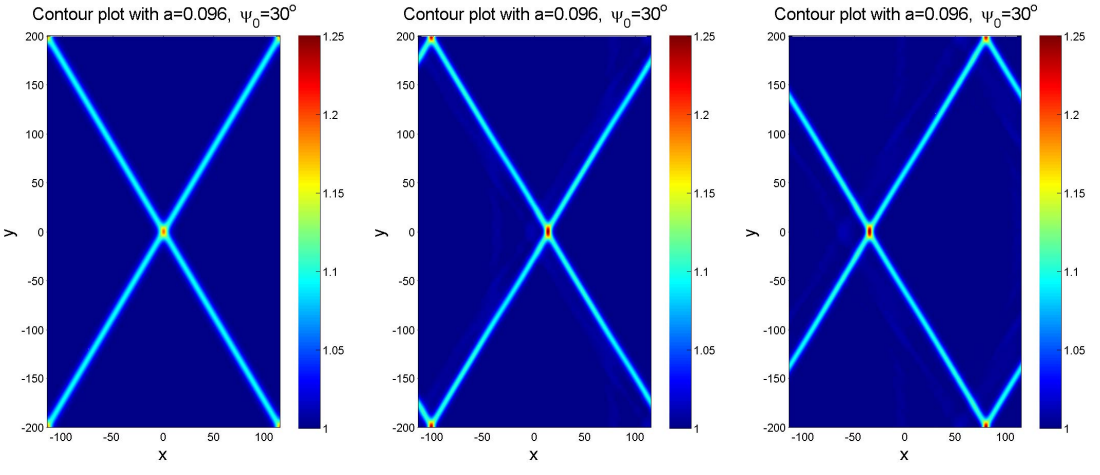

Figure 5.22 From left to right, these panels correspond to the contour plots of the solutions at $T = 0,\ 150,\ \text{and}\ 250$.

When the wave amplitude is increased to $a = 0.367$ with the same incidence angle $\psi_0 = \pi/6$ for which $k = \frac{\tan\psi_0}{\sqrt{3a}\cos\psi_0} < 1$, the reflection is irregular (i.e., we can see the Mach stem). The numerical solutions for the free surface profiles are shown in Figure 5.23 while their contour plots are shown in Figure 5.24. These numerical results are consistent with the KP theory although the critical value for the strongly nonlinear model might be different from the KP prediction.

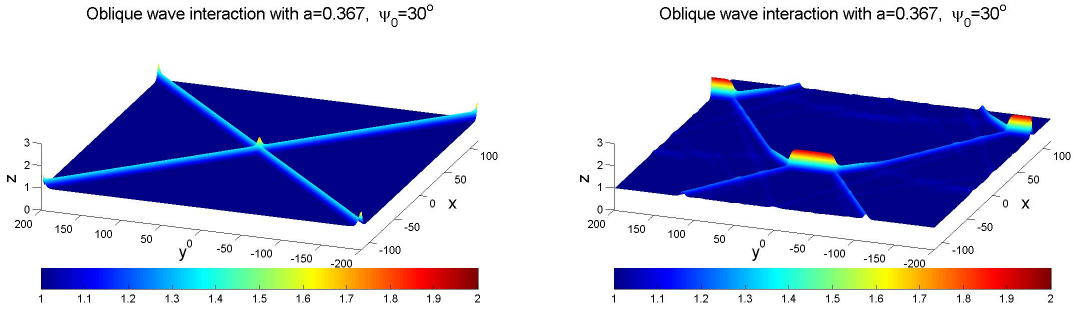

Figure 5.23 From left to right, these panels correspond to the numerical solutions at $T = 0$ and $T = 300$.

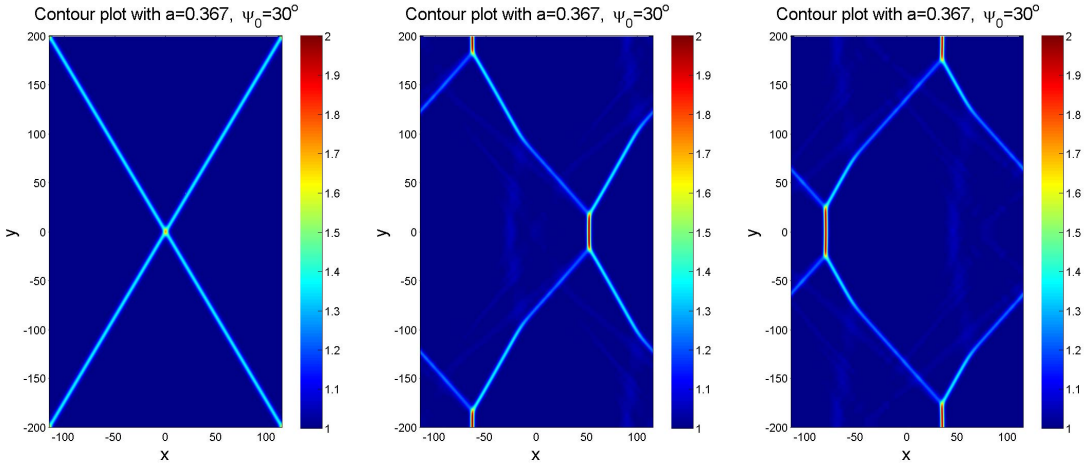

Figure 5.24 From left to right, these panels correspond to the contour plots of the solutions at $T = 0,\ 200,$ and 270.

5.4.3 Comparison with Tanaka's Numerical Solutions

The reflection of an obliquely incident solitary wave by a vertical wall was studied numerically by Tanaka [30] by solving numerically the full Euler equations using the high-order spectral method developed by Dommermuth and Yue [9]. Funakoshi [13] also studied this problem numerically by using the Boussinesq equations and confirmed the results of Miles [27]. Although the Mach reflection described by Miles' model and the KP equation is an asymptotic state as $T \to \infty$, it can be compared well with the long-term numerical solutions, as demonstrated by Funakoshi [14].

Here we investigate the phenomenon of the Mach reflection numerically by using the strongly nonlinear weakly 2D long wave model. We should remark that our initial conditions are different from those of Tanaka although we use the same physical parameters. Nevertheless, it is observed that our solutions compare well with the numerical solutions of Tanaka as T tends to infinity. In addition, we also compare our numerical solutions with Miles' model and the KP solutions.

For $a = 0.1,\ \psi_0 = 23^o$, we can see from Figure 5.25 that the amplification factor $\alpha = \frac{a_M}{a}$ (a_M is the wave amplitude of the Mach stem) is still increasing slightly at $T = 300$, but appears to approach to a value close to 3.00 which is what Miles predicted. The amplification factor α computed by Tanaka [30] is about 2.95 at $T = 300$. This value is smaller than the value 3.39 which is predicted by the KP equation.

As can be seen from Figure 5.26, for $a = 0.3,\ \psi_0 = 40^o$, we can see that the maximum wave amplitude first increases until $T = 250$; after that, it decreases slowly. The amplification factor $\alpha = \frac{a_M}{a}$ has almost reached at a steady value by time $T = 300$ and it is approximately 2.38. In Tanaka's numerical experiment, the amplification factor α is computed to be about 2.4 at time $T = 100$, which is smaller than 3.01 predicted by Miles' model and 2.67 predicted by the KP equation. For this set of parameters, the criticality between the regular and Mach reflections is

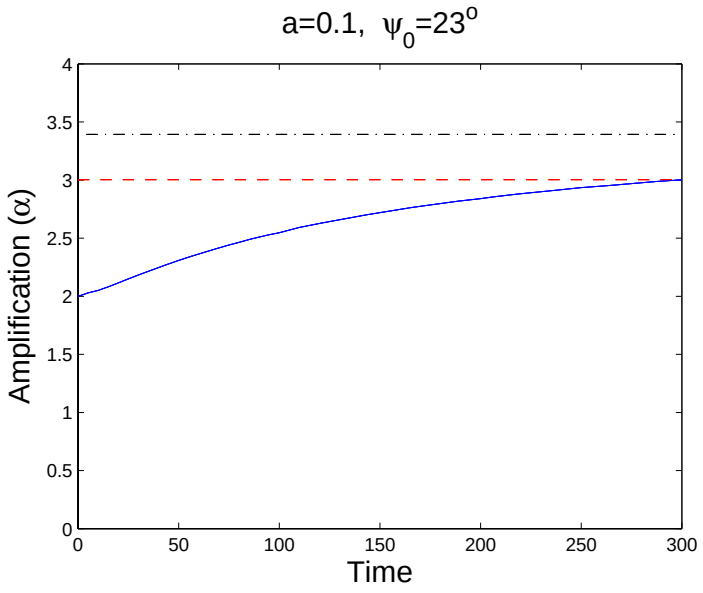

Figure 5.25 The evolution of amplification factor α as a function of time T with incident wave amplitude $a = 0.1$ and incident angle $\psi_0 = 23^o$. The solid line is the numerical result. The dash line is the predicted value given by Miles' model and the dash dot line is the value predicted by the KP equation.

estimated to be $k = \frac{\psi_0}{\sqrt{3a}} = 0.736 < 1$ by Miles' model and, therefore, the Mach reflection should happen. On the other hand, from the analysis of the KP equation, the critical number is found $k = \frac{\tan\psi}{\sqrt{3a}\cos\psi} = 1.15 > 1$; so it should be the regular reflection. After comparing the wave amplitude of the reflected wave with the incident wave, Tanaka believed that the observed reflection is a regular reflection rather than a Mach reflection, which is consistent with the KP theory.

Since Tanaka solved the Euler equations to study the oblique interaction of two solitary waves, it should be more accurate than the simplified weakly nonlinear long wave models. After comparing the amplification factor α obtained from our numerical solutions of the strongly nonlinear long wave model with that of Tanaka, it can be concluded that our model is an efficient model to study the oblique interaction between two solitary wave solutions.

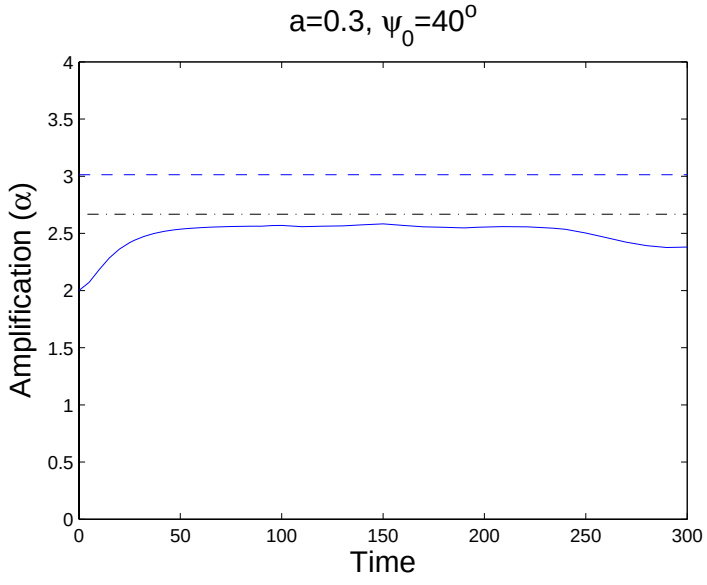

Figure 5.26 The evolution of amplification factor α as a function of time T with incident wave amplitude $a = 0.3$ and incident angle $\psi_0 = 40^o$. The solid line is the numerical result. The dash line is the predicted value given by Miles' model and the dash dot line is the value predicted by the KP equation.

5.4.4 Comparison with Experiment Data and the KP Solution

A laboratory experiment of the Mach reflection was recently carried out and detailed measurements using the laser induced fluorescent (LIF) technique were reported in Yeh, Li and Kodama [39]. They focus on the interaction of two identical solitary waves propagating with a small oblique angle $2\psi_0$ to produce the Mach reflection with the incident wave angle ψ_0 to a perfectly reflective vertical wall. Later they analyze their observation in a systematic fashion and compared with the KP theory.

Since it is not trivial to match initial conditions for our numerical simulations with experimental observations, we compare the asymptotic states approximated by the numerical solutions of the strongly nonlinear weakly 2D long wave model at $T = 300$ with the asymptotic states described by the KP equation and obtained from the laboratory data using a curve fit to obtain the behavior as $T \to \infty$.

The stem amplification factor $\alpha = \frac{A_M}{A_0}$ (A_M is the amplitude of the Mach stem, A_0 is the incident wave amplitude) induced by a variety of incident waves with amplitudes $0.086 < A_0 < 0.413$ and incident angle $\psi_0 = 30^0$ are presented in Table 5.3. It is evident that the limited physical dimension of the laboratory apparatus prevents the Mach stem from reaching its fully developed state. In Table 5.3, the experimental results of the amplification factor α are compared with the exact solutions of the KP equation at $X = 71.1$, the farthest measuring location in their experiment. Later Yeh, Li and Kodama [39] estimated the asymptotic amplification factors by using the exponential curve fitting to the data: $\alpha = ae^{-bx} + c$, where a, b and c are positive constants to be determined.

Table 5.3 Amplification factor α of the stem waves for different wave amplitude A_0 $\left(k = \frac{\tan\psi_0}{\sqrt{2A_0}}\right)$ with $\psi_0 = 30^0$: $\alpha_{X=71.1}$(Exp) are the laboratory data at location $X = 71.1$ and $\alpha_{X=71.1}$(KP) are calculated from the correspond-ing KP exact solutions at the given location. $\alpha_{T=300}$(Num) are numerical results obtained by using strongly nonlinear weakly 2D long wave model at $T = 300$. When $A_0 = 0.086$ and $A_0 = 0.108$, the amplification factor α is calculated at $T = 400$. $\alpha_{T=\infty}$(Exp) are estimated from the exponential curve fitting to the laboratory data, and $\alpha_{T=\infty}$(KP) are values predicted by the solution of the KP equation as $T \to \infty$. In the last row of $A_0 = 0.413$, the values of α in the brackets are obtained at $X = 50.8$, because of the wave breaking immediately after this point; hence, the greater amplification cannot be realized in experiment. The large deviations in the estimation $\alpha_{T=\infty}$(Exp) in the boxes from the theoretical predictions for the cases near $k = 1$

A_0	k	$\alpha_{X=71.1}$ (Exp)	$\alpha_{X=71.1}$ (KP)	$\alpha_{T=\infty}$ (Exp)	$\alpha_{T=\infty}$ (KP)	$\alpha_{T=300}$ (Num)
0.086	1.392	2.10	2.36	2.13	2.36	(2.34)
0.108	1.242	2.13	2.51	2.19	2.51	(2.41)
0.161	1.017	2.24	3.38	2.33	3.38	2.99
0.212	0.887	2.33	2.43	2.46	3.56	3.16
0.312	0.731	2.52	2.61	2.92	2.99	2.81
0.413	0.635	(2.48)	(2.61)	3.94	2.67	2.50

From Table 5.3, we can see that, for wave amplitudes $A_0 = 0.086$ and $A_0 = 0.108$, the asymptotic states obtained by our numerical simulations and the values predicted by the KP equation are very close; both of them agree well with the estimation from the experimental data. It is not surprising since the wave amplitudes are small and, therefore, our model should be consistent with the weakly nonlinear model.

For $A_0 = 0.161$ and $A_0 = 0.212$, the amplification factors α obtained numerically are smaller than those predicted by the KP equation, but closer to those estimated from experimental data. This implies that, when the wave amplitude is not so small, the strongly nonlinear long wave model approximate the experiment better than the weakly nonlinear KP equation.

For these four cases, we can see that the amplification factors α obtained by estimating experimental data are smaller than the theoretical predicted values. This is because the wave reflection in the laboratory is still in the process of being established and it is reasonable that the measured stem-wave amplitude is slightly lower.

When $A_0 = 0.312$ and $A_0 = 0.413$, we found that the amplification factors α obtained numerically are smaller than those obtained from the estimation of the experimental data. This discrepancy has not been fully understood yet, but it could be explained as follows. When the ratio of the incident angle and wave amplitude is small, it may take a long time to reach asymptotic state, but the length of wave tank might be too short to observe it. In addition, wave breaking was observed experimentally.

CHAPTER 6

CONCLUSION

The evolution of large amplitude long surface waves was investigated numerically using the strongly nonlinear asymptotic model.

For one-dimensional waves, the strongly nonlinear long wave model was generalized to include the effect of background shear and was solved numerically using a 4th-order finite difference method in §3 to study the interaction between two large amplitude solitary waves. Our numerical solutions shown a few higher-order nonlinear effects when compared with weakly nonlinear asymptotic results based on the weakly nonlinear bidirectional long wave model. In uniform flow ($F = 0$), the maximum wave amplitude during a head-on collision and the absolute value of the symmetric phase shift after the collision are larger than those predicted by the weakly nonlinear theory. However, in the presence of background shear ($F \neq 0$), it was found that the phase shift is asymmetric and the maximum wave amplitude is smaller than the value predicted by the weakly nonlinear theory. For an overtaking collision, based on the weakly nonlinear analysis, it has been known that the critical wave amplitude ratio is equal to 3. If the ratio is greater than the critical ratio, the two solitary waves merge into a single peak wave during the overtaking collision. For strongly nonlinear solitary waves in uniform shear, it was shown that the critical ratio depends on the wave amplitude, the Froude number F, and the propagation direction as well.

The generation of solitary waves due to the interaction of a background uniform shear flow with bottom topography is also considered. When compared with the uniform flow case, it is found that the amplitudes of the generated solitary waves propagating upstream are much larger and the period of the generation is much longer

in uniform shear flow. It is also noted that the depth of depressed water behind the topography is no longer uniform.

In §4, we adopted an asymptotic approach to study transverse instability of large amplitude solitary waves with introducing a small amplitude perturbation in the y-direction. A sufficient condition for instability ($a > 3.41$) was obtained and it is found that our numerical solutions for unstable solitary waves are consistent with our stability analysis.

We derived the weakly 2D strongly nonlinear long wave model to study the generation of a Mach stem due to the nonlinear interaction between two obliquely propagating solitary waves with a small angle. After validating the numerical solutions of the strongly nonlinear model with those of the Euler equations obtained by Tanaka [30], we compared our numerical solutions for the amplitude of the Mach stem with the weakly nonlinear KP solutions and available experimental data. When the wave amplitude is not so small, our numerical solutions are found to agree better with the experiment than the prediction by the KP equation.

APPENDIX A

TRANSVERSE INSTABILITY BY WEAKLY 2D MODEL

In chapter 4, we investigated transverse instability of large amplitude solitary waves using the strongly nonlinear fully 2D long wave model under the assumption that the perturbation in the y-direction is very small, which is consistent with the weakly 2D long wave model. Therefore, we expect the same sufficient condition of transverse instability when we use weakly 2D model, as shown below.

The strongly nonlinear weakly 2D long wave model is given by

$$\frac{\partial \eta}{\partial t} + \frac{\partial \eta u}{\partial x} + \frac{\partial \eta v}{\partial y} = 0 \ , \tag{A.1}$$

$$\frac{\partial u}{\partial t} + u\frac{\partial u}{\partial x} + v\frac{\partial u}{\partial y} + \frac{\partial \eta}{\partial x} = \frac{1}{\eta}\frac{\partial}{\partial x}\left(\frac{\eta^3}{3}G\right) \ , \tag{A.2}$$

$$\frac{\partial v}{\partial t} + u\frac{\partial v}{\partial x} + v\frac{\partial v}{\partial y} + \frac{\partial \eta}{\partial y} = \frac{1}{\eta}\frac{\partial}{\partial y}\left(\frac{\eta^3}{3}G\right) \ , \tag{A.3}$$

where u and v are the horizontal velocities in the x and y directions, η is the wave elevation, and G is defined as

$$G\left(x, y, t\right) = u_{xt} + uu_{xx} - u_x^2.$$

We seek a solitary wave solution of equations (A.1)–(A.3) in the following form

$$u = -c + u_s(x), \quad \eta = \eta_s(x), \quad v = 0, \tag{A.4}$$

where u_s and η_s tend to zero as $x \to \pm\infty$ and c is a positive wave speed. Then, $\eta_s(x)$ and $u_s(x)$ satisfy the following equations:

$$\frac{\partial}{\partial x}\left[\left(-c + u_s\right)\eta_s\right] = 0 \ , \tag{A.5}$$

$$\left(-c + u_s\right)\frac{\partial u_s}{\partial x} + \frac{\partial \eta_s}{\partial x} = \frac{1}{\eta_s}\frac{\partial}{\partial x}\left[\frac{\eta_s^3}{3}\left(\left(-c + u_s\right)\frac{\partial^2 u_s}{\partial x^2} - \left(\frac{\partial u_s}{\partial x}\right)^2\right)\right]. \tag{A.6}$$

Now we carry out linear stability analysis of the solitary wave solution given by equation (A.4). First we assume the solutions of equations (A.1)–(A.3) can be written as

$$\eta(x,y,t) = \eta_s(x) + \hat{\eta}(x)\exp^{\lambda t + i\epsilon y}\ , \tag{A.7}$$

$$u(x,y,t) = -c + u_s(x) + \hat{u}(x)\exp^{\lambda t + i\epsilon y}\ , \tag{A.8}$$

$$v(x,y,t) = \hat{v}(x)\exp^{\lambda t + i\epsilon y}\ , \tag{A.9}$$

where ϵ is the wave number in the y direction and λ is a complex constant which will be determined by solving a set of equations for $\hat{u},\ \hat{v}$, and $\hat{\eta}$ derived from equations (A.1)–(A.3). The steady solutions given by (A.4) are unstable if λ has a positive real part; otherwise they are stable. By substituting equations (A.7)–(A.9) into equations (A.1)–(A.3), linearizing with respect to $(\hat{u},\ \hat{v},\ \hat{\eta})$, and imposing the zero boundary conditions as $x \to \pm\infty$, we obtain the set of linear equations for $\hat{u},\ \hat{v}$, and $\hat{\eta}$:

$$L_1\left[\hat{u},\ \hat{\eta}\right] = -i\epsilon\eta_s\hat{v} - \lambda\hat{\eta}, \tag{A.10}$$

$$\begin{aligned} L_2\left[\hat{u},\ \hat{\eta}\right] = {} & \frac{i\epsilon}{3\eta_s}\frac{\partial}{\partial x}\left\{\eta_s^3\left[\left(-c+u_s\right)\frac{\partial\hat{v}}{\partial x} - 2\frac{\partial u_s}{\partial x}\hat{v}\right]\right\} \\ & -\lambda\left\{\hat{u} - \frac{1}{3\eta_s}\frac{\partial}{\partial x}\left[\eta_s^3\left(\frac{\partial\hat{u}}{\partial x} + i\epsilon\hat{v}\right)\right]\right\}, \end{aligned} \tag{A.11}$$

$$\begin{aligned} \left(-c+u_s\right)\frac{\partial\hat{v}}{\partial x} = {} & \epsilon L_3[\hat{u},\ \hat{\eta}] - \epsilon^2\frac{\eta_s^2}{3}\left[\left(-c+u_s\right)\frac{\partial\hat{v}}{\partial x} - 2\frac{\partial u_s}{\partial x}\hat{v}\right] \\ & +\lambda\left[i\epsilon\frac{\eta_s^2}{3}\frac{\partial\hat{u}}{\partial x} - \left(1+\epsilon^2\right)\hat{v}\right], \end{aligned} \tag{A.12}$$

where the linear operators L_1, L_2, and L_3 are defined as

$$L_1[\hat{u},\hat{\eta}] = \frac{\partial}{\partial x}\left(\eta_s\hat{u}\right) + \frac{\partial}{\partial x}\left[\left(-c+u_s\right)\hat{\eta}\right], \tag{A.13}$$

$$\begin{aligned} L_2[\hat{u},\hat{\eta}] = {} & -\frac{1}{3\eta_s}\frac{\partial}{\partial x}\left\{\eta_s^3\left[\left(-c+u_s\right)\frac{\partial^2\hat{u}}{\partial x^2} + \hat{u}\frac{\partial^2 u_s}{\partial x^2} - 2\frac{\partial u_s}{\partial x}\frac{\partial\hat{u}}{\partial x}\right]\right\} \\ & +\frac{\partial}{\partial x}\left[\left(-c+u_s\right)\hat{u}\right] + \frac{1}{3}\eta_s\hat{\eta}\left[\left(-c+u_s\right)\frac{\partial^3 u_s}{\partial x^3} - \frac{\partial u_s}{\partial x}\frac{\partial^2 u_s}{\partial x^2}\right] \\ & +\frac{\partial\hat{\eta}}{\partial x} - \frac{\partial}{\partial x}\left\{\left(\eta_s\hat{\eta}\right)\left[\left(-c+u_s\right)\frac{\partial^2 u_s}{\partial x^2} - \left(\frac{\partial u_s}{\partial x}\right)^2\right]\right\}, \end{aligned} \tag{A.14}$$

$$L_3[\hat{u},\ \hat{\eta}] = i\frac{\eta_s^2}{3}\left[(-c+u_s)\frac{\partial^2\hat{u}}{\partial x^2} + \frac{\partial^2 u_s}{\partial x^2}\hat{u} - 2\frac{\partial u_s}{\partial x}\frac{\partial\hat{u}}{\partial x}\right] + i\left\{\eta_s\left[(-c+u_s)\frac{\partial^2 u_s}{\partial x^2} - \left(\frac{\partial u_s}{\partial x}\right)^2\right] - 1\right\}\hat{\eta}. \tag{A.15}$$

The boundary conditions to be imposed are given by

$$\hat{u}\,(x) \to 0,\ \hat{v}\,(x) \to 0,\ \hat{\eta}\,(x) \to 0 \ \text{ as } \ x \to \pm\infty. \tag{A.16}$$

When there are no perturbations in the y direction (i.e., $\epsilon = 0$ and $\hat{v} = 0$), equations (A.10)–(A.12) can be reduced to

$$L_1[\hat{u},\hat{\eta}] = -\lambda\hat{\eta}, \tag{A.17}$$

$$L_2[\hat{u},\hat{\eta}] = -\lambda\left(\hat{u} - \eta_s\frac{\partial\eta_s}{\partial x}\frac{\partial\hat{u}}{\partial x} - \frac{\eta_s^2}{3}\frac{\partial^2\hat{u}}{\partial x^2}\right). \tag{A.18}$$

This is an eigenvalue problem for $\hat{u}$ and $\hat{\eta}$. Notice that $\lambda = 0$ is always an eigenvalue of equations (A.17)–(A.18) and is in fact the only eigenvalue of equations (A.17)–(A.18) when the speed of a solitary wave is close to the linear wave speed [23].

In order to study stability of the solitary wave solution given by (A.4) subject to long wavelength transverse perturbations, we assume that ϵ is small and expand λ, $\hat{\eta}$, $\hat{u}$, and $\hat{v}$ as

$$\hat{u}(x) = \hat{u}_0(x) + \epsilon\hat{u}_1(x) + \epsilon^2\hat{u}_2(x) + \epsilon^3\hat{u}_3(x) + \cdots\cdots\ , \tag{A.19}$$

$$\hat{\eta}(x) = \hat{\eta}_0(x) + \epsilon\hat{\eta}_1(x) + \epsilon^2\hat{\eta}_2(x) + \epsilon^3\hat{\eta}_3(x) + \cdots\cdots\ , \tag{A.20}$$

$$\hat{v}(x) = \hat{v}_0(x) + \epsilon\hat{v}_1(x) + \epsilon^2\hat{v}_2(x) + \epsilon^3\hat{v}_3(x) + \cdots\cdots\ , \tag{A.21}$$

$$\lambda = \epsilon\lambda_1 + \epsilon^2\lambda_2 + \epsilon^3\lambda_3 + \cdots\cdots\ . \tag{A.22}$$

Substituting the expansions of λ, $\hat{\eta}$, $\hat{u}$, and $\hat{v}$ into equations (A.10)–(A.12) and collecting the same order terms in ϵ, we have

$$L_1[\hat{u}_n, \hat{\eta}_n] = F_n, \tag{A.23}$$

$$L_2[\hat{u}_n, \hat{\eta}_n] = G_n, \tag{A.24}$$

$$(-c + u_s)\frac{\partial \hat{v}_n}{\partial x} = L_3[\hat{u}_{n-1}, \hat{\eta}_{n-1}] + H_n, \tag{A.25}$$

where $L_1,\ L_2$, and L_3 are defined in equations (A.13)–(A.15) and

$$F_n = -\lambda_j \hat{\eta}_{n-j} - i\eta_s \hat{v}_{n-1}, \tag{A.26}$$

$$G_n = -\lambda_j \left[\hat{u}_{n-j} - \frac{1}{3\eta_s}\frac{\partial}{\partial x}\left(\eta_s^3 \frac{\partial \hat{u}_{n-j}}{\partial x}\right)\right], \tag{A.27}$$

$$H_n = \lambda_j \left(\frac{i\eta_s^2}{3}\frac{\partial \hat{u}_{n-1-j}}{\partial x} - \hat{v}_{n-j}\right). \tag{A.28}$$

We remark that $\hat{u}_{-j} = 0$, $\hat{v}_{-j} = 0$, and $\hat{\eta}_{-j} = 0$, $j = 1,\ 2,\ \cdots$, $n = 0,\ 1,\ 2,\ \cdots$.

After solving following equation

$$\int_{-\infty}^{\infty} \left(\eta^* L_1[\eta, u] + u^* L_2[\eta, u]\right)\ dx = \int_{-\infty}^{\infty} \left(\eta L_1^*[\eta^*, u^*] + u^* L_2^*[\eta^*, u^*]\right)\ dx,$$

we obtain the adjoint equations of the homogeneous parts of equations (A.23)–(A.24), given by

$$L_1^*[u^*,\ \eta^*] = 0, \qquad L_2^*[u^*,\ \eta^*] = 0, \tag{A.29}$$

where L_1^* and L_2^* are the adjoint operators of L_1 and L_2 and are defined by

$$\begin{aligned} L_1^*[u^*,\ \eta^*] = &-\frac{\partial u^*}{\partial x} + \eta_s \frac{\partial}{\partial x}\left\{\left[(-c + u_s)\frac{\partial^2 u_s}{\partial x^2} - \left(\frac{\partial u_s}{\partial x}\right)^2\right] u^*\right\} \\ &- (-c + u_s)\frac{\partial \eta^*}{\partial x} - \frac{2\eta_s}{3}\left[(-c + u_s)\frac{\partial^3 u_s}{\partial x^3} - \frac{\partial u_s}{\partial x}\frac{\partial^2 u_s}{\partial x^2}\right] u^*, \end{aligned} \tag{A.30}$$

$$\begin{aligned} L_2^*[u^*,\ \eta^*] = &-\eta_s \frac{\partial \eta^*}{\partial x} - (-c + u_s)\frac{\partial u^*}{\partial x} \\ &-\frac{u^*}{3\eta_s}\frac{\partial}{\partial x}\left(\eta_s^3 \frac{\partial^2 u_s}{\partial x^2}\right) - \frac{\partial}{\partial x}\left[2\eta_s \frac{\partial \eta_s}{\partial x}\frac{\partial u_s}{\partial x}u^* + \frac{\eta_s^2}{3}\frac{\partial^2 u_s}{\partial x^2}u^*\right] \\ &+\frac{\partial^3}{\partial x^3}\left[\frac{\eta_s^2}{3}(-c + u_s)u^*\right] - \frac{\partial^2}{\partial x^2}\left[\eta_s \frac{\partial \eta_s}{\partial x}(-c + u_s)u^* - \frac{\eta_s^2}{3}\frac{\partial u_s}{\partial x}u^*\right]. \end{aligned} \tag{A.31}$$

From equations (A.5)–(A.6), we know $u^* = \eta_s$ and $\eta^* = u_s$ are the solutions of the adjoint equations. Therefore, for the inhomogeneous equations given by (A.23)–(A.24) to have solutions, their inhomogeneous terms on the right-hand sides should satisfy the following solvability conditions:

$$\int_{-\infty}^{\infty} (u_s F_n + \eta_s G_n) dx = 0. \tag{A.32}$$

For $n = 0$, we have

$$L_1[\hat{u}_0, \hat{\eta}_0] = 0, \tag{A.33}$$

$$L_2[\hat{u}_0, \hat{\eta}_0] = 0, \tag{A.34}$$

$$(-c + u_s)\frac{\partial \hat{v}_0}{\partial x} = 0. \tag{A.35}$$

The nontrivial solutions of the homogeneous equations (A.33)–(A.35) satisfying the boundary conditions given by equation (A.16) as $x \to \pm\infty$ can be found as

$$\hat{u}_0 = \frac{\partial u_s}{\partial x},\ \hat{\eta}_0 = \frac{\partial \eta_s}{\partial x},\ \text{and}\ \hat{v}_0 = 0.$$

For $n = 1$, we have

$$L_1[\hat{u}_1, \hat{\eta}_1] = -\lambda_1 \hat{\eta}_0, \tag{A.36}$$

$$L_2[\hat{u}_1, \hat{\eta}_1] = -\lambda_1 (\hat{u}_0 - \eta_s \frac{\partial \eta_s}{\partial x}\frac{\partial \hat{u}_0}{\partial x} - \frac{\eta_s^2}{3}\frac{\partial^2 \hat{u}_0}{\partial x^2}), \tag{A.37}$$

$$(-c + u_s)\frac{\partial \hat{v}_1}{\partial x} = i(-c + u_s)\frac{\partial u_s}{\partial x}. \tag{A.38}$$

The solvability condition given by equation (A.32) is satisfied automatically, i.e.,

$$-\lambda_1 \int_{-\infty}^{\infty} \left[\frac{\partial}{\partial x}(\eta_s u_s) - \frac{1}{3}\frac{\partial}{\partial x}\left(\eta_s^3 \frac{\partial^2 u_s}{\partial x^2} \right) \right] dx = 0, \tag{A.39}$$

and, therefore, λ_1 cannot be determined at this order. Then, the general solutions of equations (A.36)–(A.38) satisfying the boundary conditions given by equation (A.16)

as $x \to \pm\infty$ are

$$\hat{u}_1 = r_1 \frac{\partial u_s}{\partial x} - \lambda_1 \frac{\partial u_s}{\partial c},\ \hat{\eta}_1 = r_1 \frac{\partial \eta_s}{\partial x} - \lambda_1 \frac{\partial \eta_s}{\partial c},\ \text{and}\ \hat{v}_1 = i u_s,$$

where r_1 is an arbitrary constant, $\frac{\partial u_s}{\partial c}$ and $\frac{\partial \eta_s}{\partial c}$ represent the derivatives of u_s and η_s with respect to c for fixed x.

For $n = 2$, we have

$$L_1[\hat{u}_2, \hat{\eta}_2] = -\lambda_2 \hat{\eta}_0 - \lambda_1 \hat{\eta}_1 + \eta_s u_s, \tag{A.40}$$

$$L_2[\hat{u}_2, \hat{\eta}_2] = -\lambda_2 \left[\hat{u}_0 - \frac{1}{3\eta_s} \frac{\partial}{\partial x} \left(\eta_s^3 \frac{\partial \hat{u}_0}{\partial x} \right) \right] - \lambda_1 \left[\hat{u}_1 - \frac{1}{3\eta_s} \frac{\partial}{\partial x} \left(\eta_s^3 \frac{\partial \hat{u}_1}{\partial x} \right) \right], \tag{A.41}$$

$$\begin{aligned} (-c + u_s) \frac{\partial \hat{v}_2}{\partial x} &= i \frac{\eta_s^2}{3} \left[(-c + u_s) \frac{\partial^2 \hat{u}_1}{\partial x^2} + \frac{\partial^2 u_s}{\partial x^2} \hat{u}_1 - 2 \frac{\partial u_s}{\partial x} \frac{\partial \hat{u}_1}{\partial x} \right] - \lambda_1 \left(\hat{v}_1 - i \frac{\eta_s^2}{3} \frac{\partial \hat{u}_0}{\partial x} \right) \\ &\quad + i \left\{ \eta_s \left[(-c + u_s) \frac{\partial^2 u_s}{\partial x^2} - \left(\frac{\partial u_s}{\partial x} \right)^2 \right] - 1 \right\} \hat{\eta}_1. \end{aligned} \tag{A.42}$$

The solvability condition given by equation (A.32) is

$$-\lambda_1^2 \int_{-\infty}^{\infty} \frac{\partial}{\partial c} (\eta_s u_s) dx = \int_{-\infty}^{\infty} \eta_s u_s^2 dx, \tag{A.43}$$

which determines λ_1. From the fact that the steady solution u_s and η_s satisfy equations (A.5)–(A.6), we can see that $\eta_s u_s^2 > 0$, $\frac{\partial}{\partial c} (\eta_s u_s) > 0$, and

$$\lambda_1 = \pm i \sqrt{\frac{\int_{-\infty}^{\infty} \eta_s u_s^2 dx}{\int_{-\infty}^{\infty} \frac{\partial}{\partial c} (\eta_s u_s)\, dx}}. \tag{A.44}$$

The real part of λ_1 is zero so that the stability of the solitary wave solutions is not determined at this order; therefore, we have to proceed our analysis to the next order.

For $n = 3$, the solvability condition given by equation (A.32) is

$$\lambda_1 \lambda_2 \int_{-\infty}^{\infty} \frac{\partial}{\partial c} (\eta_s u_s) dx - \lambda_1 \int_{-\infty}^{\infty} (u_s \hat{\eta}_2 + \eta_s \hat{u}_2) dx = \int_{-\infty}^{\infty} i \eta_s u_s \hat{v}_2 dx. \tag{A.45}$$

To evaluate λ_2, notice that we have to find solutions of equations (A.40)–(A.42) for $\hat{u}_2,\ \hat{\eta}_2$, and $\hat{v}_2$. Since $L_1,\ L_2$ are linear operators, we can decompose $\hat{u}_2$ and $\hat{\eta}_2$ into

three parts

$$\hat{u}_2 = (-\lambda_2 - \lambda_1 r_1)\hat{u}_{20} + \lambda_1^2 \hat{u}_{21} + \hat{u}_{22}, \quad \hat{\eta}_2 = (-\lambda_2 - \lambda_1 r_1)\hat{\eta}_{20} + \lambda_1^2 \hat{\eta}_{21} + \hat{\eta}_{22}, \tag{A.46}$$

where $\hat{u}_{20},\ \hat{\eta}_{20},\ \hat{u}_{21}, \hat{\eta}_{21},\ \hat{u}_{22}$, and $\hat{\eta}_{22}$ satisfy the following equations

$$L_1[\hat{u}_{20}, \hat{\eta}_{20}] = \hat{\eta}_0, \tag{A.47}$$

$$L_2[\hat{u}_{20}, \hat{\eta}_{20}] = \hat{u}_0 - \frac{1}{3\eta_s}\frac{\partial}{\partial x}\left(\eta_s^3 \frac{\partial \hat{u}_0}{\partial x}\right), \tag{A.48}$$

$$L_1[\hat{u}_{21}, \hat{\eta}_{21}] = \frac{\partial u_s}{\partial c}, \tag{A.49}$$

$$L_2[\hat{u}_{21}, \hat{\eta}_{21}] = \frac{\partial u_s}{\partial c} - \frac{1}{3\eta_s}\frac{\partial}{\partial x}\left[\eta_s^3 \frac{\partial}{\partial x}\left(\frac{\partial u_s}{\partial c}\right)\right], \tag{A.50}$$

$$L_1[\hat{u}_{22}, \hat{\eta}_{22}] = \eta_s u_s, \tag{A.51}$$

$$L_2[\hat{u}_{22}, \hat{\eta}_{22}] = 0. \tag{A.52}$$

From equations (A.47)–(A.48), we can find $\hat{u}_{20}$ and $\hat{\eta}_{20}$ as

$$\hat{u}_{20} = \frac{\partial u_s}{\partial c} + r_2 \frac{\partial u_s}{\partial x},\ \hat{\eta}_{20} = \frac{\partial \eta_s}{\partial c} + r_2 \frac{\partial \eta_s}{\partial x},$$

where r_2 is an arbitrary constant.

Substituting equation (A.46) into equation (A.45) and using the fact $\int_{-\infty}^{\infty} \frac{\partial}{\partial x}(u_s \eta_s) = 0$, the solvability condition can be rewritten as

$$\begin{aligned} i\int_{-\infty}^{\infty} (\eta_s u_s \hat{v}_2) dx = \left(2\lambda_1\lambda_2 + r_1\lambda_1^2\right)\frac{\partial}{\partial c}\int_{-\infty}^{\infty}(\eta_s u_s)dx \\ -\lambda_1^3 \int_{-\infty}^{\infty}(\hat{\eta}_{21}u_s + \hat{u}_{21}\eta_s)dx - \lambda_1 \int_{-\infty}^{\infty}(\hat{\eta}_{22}u_s + \hat{u}_{22}\eta_s)dx. \end{aligned} \tag{A.53}$$

Since u_s, η_s, $\frac{\partial u_s}{\partial c}$, and $\frac{\partial \eta_s}{\partial c}$ are even functions with respect to x, the right-hand sides of equations (A.49)–(A.50) are even functions. Then, by replacing x by $-x$ in equations (A.49)–(A.50), it can be noticed that

$$L_1[\hat{u}_{21}(x), \hat{\eta}_{21}(x)] = -L_1[\hat{u}_{21}(-x), \hat{\eta}_{21}(-x)], \tag{A.54}$$

$$L_2[\hat{u}_{21}(x), \hat{\eta}_{21}(x)] = -L_2[\hat{u}_{21}(-x), \hat{\eta}_{21}(-x)]. \tag{A.55}$$

which imply that $\hat{u}_{21}(x)$ and $\hat{\eta}_{21}(x)$ are odd functions. Therefore, we have

$$\int_{-\infty}^{\infty}(\hat{\eta}_{21}u_s + \hat{u}_{21}\eta_s)dx = 0. \tag{A.56}$$

Likewise, from

$$L_1[\hat{u}_{22}(x), \hat{\eta}_{22}(x)] = -L_1[\hat{u}_{22}(-x), \hat{\eta}_{22}(-x)], \tag{A.57}$$

$$L_2[\hat{u}_{22}(x), \hat{\eta}_{22}(x)] = -L_2[\hat{u}_{22}(-x), \hat{\eta}_{22}(-x)]. \tag{A.58}$$

we can see that $\hat{u}_{22}(x)$ and $\hat{\eta}_{22}(x)$ are odd functions, which gives

$$\int_{-\infty}^{\infty}(\hat{\eta}_{22}u_s + \hat{u}_{22}\eta_s)dx = 0. \tag{A.59}$$

Substituting equations (A.56) and (A.59) into equation (A.53), the solvability condition can be further reduced to

$$(2\lambda_1\lambda_2 + r_1\lambda_1^2)\frac{\partial}{\partial c}\int_{-\infty}^{\infty}(\eta_s u_s)dx = i\int_{-\infty}^{\infty}(\eta_s u_s \hat{v}_2)dx. \tag{A.60}$$

To evaluate λ_2, we have to find $\hat{v}_2$ by solving equation (A.42). By substituting the solutions of $\hat{\eta}_1$, $\hat{u}_1$, and $\hat{v}_1$ into equation (A.42), and combining with equation (A.6), we can obtain

$$-c\frac{\partial \hat{v}_2}{\partial x} = -i\lambda_1\left(\eta_s u_s - \eta_s\frac{\partial \eta_s}{\partial c} + \frac{1}{3}\frac{\partial D}{\partial c}\right) - icr_1\frac{\partial u_s}{\partial x}, \tag{A.61}$$

where

$$D = \eta_s^3\left[(-c + u_s)\frac{\partial^2 u_s}{\partial x^2} - (\frac{\partial u_s}{\partial x})^2\right].$$

After substituting into equation (A.60) the solitary wave solutions u_s and η_s given, from equations (A.5)–(A.6), by

$$\eta_s(x) = 1 + a\ \mathrm{sech}^2(kx),\ u_s(x) = \frac{ac\ \mathrm{sech}^2(kx)}{1 + a\ \mathrm{sech}^2(kx)},\ \text{and}\ \eta_s(-c + u_s) = -c,$$

with $k^2 = \frac{3a}{4(1+a)}$ and integrating the left-hand side of equation (A.60) by parts, we obtain

$$\int_{-\infty}^{\infty} (\eta_s u_s \hat{v}_2)\, dx = \frac{ac}{k}\left[\hat{v}_2(+\infty) + \hat{v}_2(-\infty)\right] + ir_1 \int_{-\infty}^{\infty} \left(\eta_s u_s^2\right) dx, \tag{A.62}$$

where we have used

$$\int_{-\infty}^{\infty} \tanh(kx) \left(\eta_s u_s - \eta_s \frac{\partial \eta_s}{\partial c} + \frac{1}{3}\frac{\partial D}{\partial c}\right) dx = 0. \tag{A.63}$$

By using equations (A.43) and (A.62), we can simplify equation (A.60) to obtain

$$2\lambda_1\lambda_2 \frac{\partial}{\partial c} \int_{-\infty}^{\infty} (\eta_s u_s)\, dx = i\frac{ac}{k}\left[\hat{v}_2(+\infty) + \hat{v}_2(-\infty)\right]. \tag{A.64}$$

Therefore, in order to find λ_2, we only need to find the value of $\hat{v}_2$ at $x = \pm\infty$. Integrating equation (A.61) with respect to x once yields

$$\begin{aligned}\frac{c}{i\lambda_1}\hat{v}_2(x) = &\left[\frac{ac}{k} - \frac{\partial}{\partial c}\left(\frac{3a+a^2}{3k}\right) + \frac{1}{6}\frac{\partial}{\partial c}\left(\frac{8}{3}kac^2 + 8kc^2\right)\right]\tanh(kx) \\ &-\frac{1}{6}\frac{\partial}{\partial c}\left[\left(8k^2ac^2 + 8k^2c^2\right)\int_{-\infty}^{x} \frac{dt}{a + \cosh^2(kt)}\right] + \mathrm{Term}(x) + E,\end{aligned} \tag{A.65}$$

where E is an integration constant and

$$\begin{aligned}\mathrm{Term}(x) = &-icr_1 u_s(x) - \frac{(3a+a^2)\frac{\partial k}{\partial c}x}{3k\cosh^2(kx)} - \frac{\frac{\partial}{\partial c}\left(\frac{a^2}{6k}\right)\sinh(kx)}{\cosh^3(kx)} \\ &+\frac{\partial}{\partial c}\left(\frac{2kac^2\sinh(kx)}{9\cosh^3(kx)}\right) - \frac{a^2\left(\cosh^2(kx) - 3\sinh^2(kx)\right)\frac{\partial k}{\partial c}x}{3k\cosh^4(kx)},\end{aligned}$$

which vanishes as $x \to \pm\infty$.

From equation (A.65), we can see that as $x \to \pm\infty$, $\hat{v}_2(x)$ does not tend to zero no matter what the integration constant E is, i.e., this solution $\hat{v}_2(x)$ does not satisfy the boundary conditions shown in equation (A.16). We should call that $\hat{u}_2$, $\hat{v}_2$, and $\hat{\eta}_2$ near-field solutions. In order to satisfy the boundary conditions as $x \to \pm\infty$, we need to find far-field solutions whose varies much more slowly in x. By matching

the near-field and far-field solutions, we can find the values of $\hat{v}_2(\infty)$ and $\hat{v}_2(-\infty)$ to determine the value of λ_2.

In order to find far-field solutions, we introduce two slow scales x_1 and x_2 defined by

$$x_1 = \epsilon x, \quad x_2 = \epsilon^2 x, \tag{A.66}$$

where ϵ is the small parameter measuring the small wave number in the transverse direction. Then we look for solutions of equations (A.10)–(A.12) in the following power series in ϵ which depend on x_1 and x_2 as

$$\hat{u}(x_1, x_2) = \epsilon^2 \hat{u}_{F2} + \epsilon^3 \hat{u}_{F3} + \cdots, \tag{A.67}$$

$$\hat{\eta}(x_1, x_2) = \epsilon^4 \hat{\eta}_{F4} + \epsilon^5 \hat{\eta}_{F5} + \cdots, \tag{A.68}$$

$$\hat{v}(x_1, x_2) = \epsilon^2 \hat{v}_{F2} + \epsilon^3 \hat{v}_{F3} + \cdots, \tag{A.69}$$

where subscript F represents far-field solutions.

Substituting equations (A.67)–(A.69) into equations (A.10)–(A.12), collecting the same order terms in ϵ, and using the fact that

$$u_s(x) = 0, \ \eta_s(x) = 1 \text{ as } x \to \pm\infty,$$

we have, for order $O(\epsilon^3)$,

$$\frac{\partial \hat{u}_{F2}}{\partial x_1} + i\hat{v}_{F2} = 0, \tag{A.70}$$

$$\lambda_1 \hat{u}_{F2} - c\frac{\partial \hat{u}_{F2}}{\partial x_1} = 0, \tag{A.71}$$

$$\lambda_1 \hat{v}_{F2} - c\frac{\partial \hat{v}_{F2}}{\partial x_1} = 0. \tag{A.72}$$

whose solutions can be found as

$$\hat{u}_{F2}(x_1, x_2) = A(x_2)e^{(\frac{\lambda_1}{c}x_1)}, \quad \hat{v}_{F2}(x_1, x_2) = i\frac{\lambda_1}{c}A(x_2)e^{(\frac{\lambda_1}{c}x_1)}, \tag{A.73}$$

where $A(x_2)$ is an arbitrary function of x_2.

For order $O(\epsilon^4)$, we have

$$\frac{\partial \hat{u}_{F3}}{\partial x_1} + \frac{\partial \hat{u}_{F2}}{\partial x_2} + i\hat{v}_{F3} = 0, \tag{A.74}$$

$$\lambda_1 \hat{u}_{F3} - c\frac{\partial \hat{u}_{F3}}{\partial x_1} = c\frac{\partial \hat{u}_{F2}}{\partial x_2} - \lambda_2 \hat{u}_{F2}, \tag{A.75}$$

$$\lambda_1 \hat{v}_{F3} - c\frac{\partial \hat{v}_{F3}}{\partial x_1} = c\frac{\partial \hat{v}_{F2}}{\partial x_2} - \lambda_2 \hat{v}_{F2}. \tag{A.76}$$

In order to remove the secular terms, the inhomogeneous terms in equations (A.75)–(A.76) should vanish, which gives

$$c\frac{\partial \hat{u}_{F2}}{\partial x_2} - \lambda_2 \hat{u}_{F2} = 0, \tag{A.77}$$

$$c\frac{\partial \hat{v}_{F2}}{\partial x_2} - \lambda_2 \hat{v}_{F2} = 0. \tag{A.78}$$

After solving equations (A.77)–(A.78), we have, from equation (A.73),

$$A(x_2) = D_{\pm} e^{\frac{\lambda_2}{c} x_2}, \quad \hat{v}_{F2}(x_1, x_2) = iD_{\pm}\frac{\lambda_1}{c} e^{\frac{\lambda_2}{c} x_2} e^{\frac{\lambda_1}{c} x_1}, \tag{A.79}$$

where $D_{\pm}$ are constants for $x_2 > 0$ and $x_2 < 0$, respectively.

Next we have to match the near-field solution $\hat{v}_2$ in equation (A.65) with the-far field solution $\hat{v}_{F2}$ in equation (A.79).

Without loss of generality, we assume $c > 0$. If $\mathrm{Re}(\lambda_2) < 0$, we have, after imposing the boundary condition on the far-field solution and matching $\hat{v}_2$ with $\hat{v}_{F2}$ at $x = -\infty$,

$$D_- = 0,\ \hat{v}_2(-\infty) = 0,\ E = A,\ \hat{v}_2(+\infty) = \frac{i\lambda_1}{c}(2A - B),\ D_+ = 2A - B.$$

where A and B are defined by

$$A = \frac{ac}{k} - \frac{\partial}{\partial c}\left(\frac{3a+a^2}{3k}\right) + \frac{1}{6}\frac{\partial}{\partial c}\left(\frac{8}{3}kac^2 + 8kc^2\right),$$
$$B = \frac{1}{6}\frac{\partial}{\partial c}\left[(8k^2ac^2 + 8k^2c^2)\int_{-\infty}^{\infty}\frac{dx}{a+\cosh^2(kx)}\right].$$

From equation

$$2\lambda_1\lambda_2\frac{\partial}{\partial c}\int_{-\infty}^{\infty}(\eta_s u_s)dx = i\frac{ac}{k}[\hat{v}_2(+\infty) + \hat{v}_2(-\infty)],$$

and using the fact that $\frac{\partial}{\partial c}\int_{-\infty}^{\infty}(\eta_s u_s)dx > 0$, we find that

$$2\lambda_2\frac{\partial}{\partial c}\int_{-\infty}^{\infty}(\eta_s u_s)dx = -\frac{a}{k}(2A - B), \quad \text{when} \;\; (2\mathrm{A} - \mathrm{B}) > 0. \tag{A.80}$$

If $\mathrm{Re}(\lambda_2) > 0$, we obtain, after imposing the boundary condition on the far-field solution and matching $\hat{v}_2$ with $\hat{v}_{F2}$ at $x = +\infty$,

$$D_+ = 0,\ \hat{v}_2(+\infty) = 0,\ E = B - A,\ \hat{v}_2(-\infty) = \frac{i\lambda_1}{c}(B - 2A),\ D_- = B - 2A,$$

and

$$2\lambda_2\frac{\partial}{\partial c}\int_{-\infty}^{\infty}(\eta_s u_s)dx = \frac{a}{k}(2A - B), \quad \text{when} \;\; (2\mathrm{A} - \mathrm{B}) > 0. \tag{A.81}$$

Finally we can find an expression of λ_2 as:

$$\lambda_2 = \begin{cases} \pm\frac{a(2A-B)}{2k\frac{\partial}{\partial c}\int_{-\infty}^{\infty}(\eta_s u_s)dx} & : \text{ if } (2\mathrm{A} - \mathrm{B}) > 0, \\ \text{no solution} & : \text{ if } (2\mathrm{A} - \mathrm{B}) < 0. \end{cases}$$

which gives us a sufficient condition for transverse instability as $a > 3.41$.

APPENDIX B

RESCALING $F = 1$ FOR ONE-DIMENSIONAL STRONGLY NONLINEAR LONG WAVE MODEL

As pointed out by Li, the Froude number F can be scaled out from equations (3.1)–(3.2). In order to do this, we first rescale the parameters η, u, x, and t as

$$\eta = \frac{1}{F^2}\eta^*,\ u = \frac{1}{F}u^*,\ x = \frac{1}{F^2}x^*,\ t = \frac{1}{F}u^*.$$

Substituting the expansions of η, u, x, and t into equations (3.1)–(3.2), after dropping the asterisk *, we obtain the rescaled equations:

$$\eta_t + \eta\eta_x + (\eta u)_x = 0, \tag{B.1}$$

$$u_t + uu_x + \zeta_x = \frac{1}{\eta}\left[\frac{\eta^3}{3}\left(u_{xt} + uu_{xx} - u_x^2 + \eta u_{xx}\right)\right]_x. \tag{B.2}$$

Notice that this rescaling is only valid for $F \neq 0$. In this study, we leave F in the system so that we can study the system for both $F = 0$ and $F \neq 0$.

REFERENCES

[1] T. B. Benjamin. The solitary wave on a stream with an arbitrary distribution of vorticity. *J. Fluid Mech*, 12:97-116, 1962.

[2] T. B. Benjamin. The stability of solitary waves. *Proc. R. Soc. Lond. A*, 328:153-183, 1972.

[3] J. Boussinesq. Theories des ondes et des remous qui se propagent le long d'un canal rectangulaire horizontal, en communiquant an liquuide contenu dans ce canal des vitesses sensiblement pareilles de la surface au fond. *J. Math pures, Appl. ser. 2*, 17:55-108, 1872.

[4] J. Boussinesq. Essai sur la theorie des eaux courants, mem. *Pres. Div. Sav. Acad. Sci. Inst. Fr*, 23:1-680, 1877.

[5] S. Chakravarty and Y Kodama. Soliton solutions of the KP equation and application to shallow water waves. *Stud. Appl. Math*, 123:83-151, 2009.

[6] W. Choi. Nonlinear evolution equations for two-dimensional surface waves in a fluid of finite depth. *J. Fluid Mech*, 295:381-394, 1995.

[7] W. Choi. Strongly nonlinear long gravity waves in uniform shear flows. *Physical Review*, E68:026305, 2003.

[8] W. Choi and R. Camassa. Fully nonlinear internal waves in a two-fluid system. *J. Fluid Mech*, 396:1-36, 1999.

[9] D. G. Dommermuth and D. K. P. Yue. A high-order spectral method for the study of nonlinear gravity waves. *J. Fluid Mech*, 184:267-288, 1987.

[10] G. A. El, R. H. J. Grimshaw, and N. F. Symth. Transcritical shallow water flow past topography: finite amplitude theory. *J. Fluid Mech*, 640:187-214, 2009.

[11] J. D. Fenton and M. M. Rienecker. A Fourier method for solving nonlinear water wave problems: Application to solitary wave interactions. *J. Fluid Mech*, 118:411-443, 1982.

[12] N. C. Freeman and R. S. Johnson. Shallow water waves on shear flows. *J. Fluid Mech*, 43:101-409, 1970.

[13] M. Funakoshi. Reflection of obliquely incident solitary waves. *J. Phys. Soc. Japan*, 49:2371-2379, 1980.

[14] M. Funakoshi. On the time evolution of a solitary wave reflected by an oblique wall. *Rep. Res. Inst. Appl. Mech. Kyushu University*, 24:79-93, 1981.

[15] A. E. Green and P. M. Naghdi. A derivation of equations for wave propagation in water of variable depth. *Journal of Fluid Mechanics*, 78(2):237-246, 1976.

[16] J. L. Hammack and H. Segur. The Korteweg de Vries equation and water waves. part 2. comparison with experiments. *J. Fluid Mech*, 65:289-314, 1974.

[17] R. Hirota. Exact solution of the korteweg-de vries equation for multiple collisions of solitons. *Physical Review Lett*, 27:1192-1194, 1971.

[18] A. Jeffrey and T. Kakutani. Stability of the Burgers shock wave and the Korteweg-de Vries soliton. *Indiana Univ. Maths. J*, 20:463-468, 1970.

[19] B. B. Kadomtsev and V. I. Petviashvili. On the stability of solitary waves in a weakly dispersing medium. *Sov. Phys. Dokl*, 15:539-541, 1970.

[20] D. J. Korteweg and G. de. Vries. On the change of form of long waves advancing in a rectanglar canal, and on a new type of long stationary waves. *Philos.Mag*, 39:422-443, 1895.

[21] M. D. Kruskal. The Korteweg-de Vries equation and related evolution equations. *In Newell*, 1974.

[22] P. D. Lax. Integrals of nonlinear equations of evolution and solitary waves. *Comm. Pure Appl. Math*, 21:467-90, 1968.

[23] Yi. A. Li. The eigenvalue problem for solitary waves of the Green-Naghdi equations. *CNLS*, 1999.

[24] Yi. A. Li, J. M. Hyman, and W. Choi. A numerical study of the exact evolution equations for surface waves in water of finite depth. *Studies in applied mathematics*, 113:303-324, 2004.

[25] T. Maxworthy. Experiments on collisions between solitary waves. *J. Fluid Mech*, 76:177-185, 1976.

[26] C. C. Mei. *The applied Dynamics of Ocean surface waves*. 1989.

[27] J. W. Miles. Obliquely interacting solitary waves. *J. Fluid Mech*, 79:157-169, 1977.

[28] C. H. Su and C. S. Gardner. Korteweg-de Vries equation and generalizations. iii: Derivation of the Korteweg-de Vries equation and Burgers equation. *J. Math. Phys*, 10:536-539, 1969.

[29] C. H. Su and R. M. Mirie. On head on collisions between two solitary waves. *J. Fluid Mech*, 98:509-525, 1980.

[30] M. Tanaka. Mach reflection of a large-amplitude solitary wave. *J. Fluid Mech*, 248:637-661, 1993.

[31] W. Tsai and D. K. P. Yue. Computation of nonlinear free-surface flows. *Ann. Rev. Fluid Mech*, 28:249-278, 1996.

[32] M. Wadati and M. Toda. The exact n-soliton solution of the Korteweg de Vries equation. *J. Phys. Soc. Jpn*, 32:1403-11, 1972.

[33] G. Wei and T. J. James. Time-dependent numerical code for extended Boussinesq equations. *J. waterway, port, and ocean engineering*, 1995.

[34] P. D. Weidman and T. Maxworthy. Experiments on strong interactions between solitary waves. *J. Fluid Mech*, 85:417-31, 1978.

[35] G. B. Whitham. *Linear and nonlinear waves*. 1974.

[36] T. Y. Wu. Generation of upstream advancing solitons by moving disturbances. *J. Fluid Mech*, 184:75-99, 1987.

[37] T. Y. Wu. A bidirectional long-wave model. *Methods and Applications of Analysis*, 1994.

[38] T. Y. Wu. Bidirectional soliton street. *Acta Mechanica Sinica*, 11:No. 4., 1995.

[39] H. Yeh, W. Li, and Y. Kodama. Mach reflection and KP solitons in shallow water. *J. Fluid Mech*, 79:157-169, 2010.

[40] N. J. Zabusky. A synergetic approach to problems of nonlinear dispersive wave propagation and interaction. *In: Ames Wed. Nonlinear partial differential equations. Academic press.*, 1967.

[41] N. J. Zabusky and C. J. Galvin. Shallow water waves, the Korteweg de Vries equation and solitons. *J. Fluid Mech*, 47:811-24, 1971.

[42] N. J. Zabusky and M. D. Kruskal. Interaction of solitons in a collisionless plasma and the recurrence of initial states. *phys Rew Lett*, 15:240-243, 1965.

[43] Q. S. Zou and C. H. Su. Overtaking collision between two solitary waves. 2. A numerical study. *J. Fluid Mech*, 29:2113-2123, 1986.